POLITECNICO
MILANO 1863

SCUOLA DI INGEGNERIA INDUSTRIALE
E DELL'INFORMAZIONE

High-speed ultrabroadband CARS microscopy based on supercontinuum generation in bulk media

Tesi di Laurea Magistrale in
Engineering Physics - Ingegneria Fisica

Author: **Francesco Gucci**

Student ID: 964359
Advisor: Prof. Dario Polli
Co-advisors: Federico Vernuccio
Academic Year: 2021-22

Abstract

Spontaneous Raman (SR) spectroscopy is a powerful label-free optical spectroscopy tool to measure vibrational spectra of molecules, providing a unique signature exploitable for the identification of the different chemical species in heterogeneous samples. SR allows one to acquire the full spectrum covering the whole Raman active region, shining the sample with a quasi-monochromatic laser beam. However, SR suffers from low scattering cross-sections, preventing high acquisition speeds. Coherent anti-Stokes Raman scattering (CARS) overcomes this limitation, as it exploits third-order non-linear optical processes that coherently excite the vibrational modes of the investigated sample. The narrowband CARS signal derives from the interaction of the sample with two spatially and temporally synchronized picosecond pulses, namely pump and Stokes, and detects a specific vibrational mode blue-shifted with respect to the generating beams. Broadband CARS (B-CARS) combines a narrowband pump beam with a broadband Stokes beam, probing multiple vibrational transitions at the same time, detected with a spectrometer.
This thesis presents an innovative B-CARS set-up, based on a fiber laser system that we use to generate a narrowband pump beam and a broadband Stokes beam via supercontinuum (SC) generation in bulk media. The work is organized as follows: Chapter 1 introduces CARS processes; Chapter 2 gives a theoretical derivation of the equations involved in CARS processes and SC generation. Chapter 3 describes the B-CARS set-up and the experimental results that I obtained during my thesis and the post-processing algorithms used to extrapolate relevant chemical information. We demonstrated that our set-up allows us to perform ultrabroadband CARS microscopy and spectroscopy, through two and three-color CARS, covering the whole Raman active region (500-3100 cm^{-1}). We performed high-speed spectroscopy ($<$1 ms/spectrum) on solvents, subcellular acids and solid-state crystals in excellent agreement with SR spectra. We then validated our system imaging plastic beads and biological samples collecting hyperspectral data at high acquisition speed in a raster-scanning fashion. Through data processing, we demonstrated that our system enables us to derive concentration maps highlighting the different chemical species in unlabeled samples.

Keywords: Broadband CARS microscopy, Two and three-color CARS, Supercontinuum generation, High-speed imaging, Post-processing algorithms.

Abstract in lingua italiana

L'effetto Raman spontaneo (SR) è un potente strumento di spettroscopia ottica label-free che permette di misurare gli interi spettri vibrazionali delle molecole illuminando il campione con un fascio laser quasi-monocromatico. Questi spettri possono essere associati in modo univoco alle specie chimiche in campioni eterogenei, permettendone l'identificazione. Tuttavia, SR soffre di basse sezioni d'urto di scattering, che impediscono il raggiungimento di velocità di acquisizione elevate. Il Coherent anti-Stokes Raman scattering (CARS) supera questo limite, poiché sfrutta processi ottici non lineari del terzo ordine che eccitano coerentemente i modi vibrazionali del campione studiato. Il segnale CARS a banda stretta deriva dall'interazione del campione con due impulsi, detti pompa e Stokes, con durata nell'ordine dei picosecondi, sincronizzati spazialmente e temporalmente, e rileva uno specifico modo vibrazionale. Il segnale risultante ha una lunghezza d'onda minore dei fasci incidenti. Il CARS a banda larga (B-CARS) combina un fascio di pompa a banda stretta con un fascio di Stokes a banda larga, sondando più transizioni vibrazionali contemporaneamente, e viene rilevato con uno spettrometro.

Questa tesi presenta un set-up B-CARS innovativo, basato su un sistema laser in fibra, utilizzato per generare un fascio di pompa a banda stretta e un fascio di Stokes a banda larga attraverso la generazione di luce supercontinua (SC) in un cristallo. Il lavoro è organizzato come segue: il Capitolo 1 introduce i processi CARS; il Capitolo 2 fornisce una derivazione teorica delle equazioni coinvolte nei processi CARS e nella generazione di SC. Il Capitolo 3 descrive il set-up B-CARS e i risultati sperimentali ottenuti durante la tesi, nonché gli algoritmi di post-processing utilizzati per estrapolare le informazioni chimiche. Abbiamo dimostrato che il nostro set-up permette di eseguire microscopia e spettroscopia CARS a banda ultra larga, attraverso two e three-color CARS, coprendo l'intera regione Raman (500-3100 cm^{-1}). Abbiamo effettuato misure di spettroscopia ad alta velocità ($<$1 ms/spettro) su solventi, acidi subcellulari e cristalli, in ottimo accordo con gli spettri ottenuti tramite SR. Abbiamo poi eseguito l'imaging di sfere di plastica e campioni biologici, acquisendo dati iperspettrali ad alta velocità. A seguito dell'elaborazione dei dati, abbiamo dimostrato che il nostro set-up consente di ricavare mappe di concentrazione che evidenziano le diverse specie chimiche in campioni privi di labelling.

Parole chiave: Microscopia Broadband CARS, Two e three-color CARS, Generazione di supercontinuo, Imaging ad alta velocità, Algoritmi di post-processing.

Contents

1 | Introduction

1.1. Historical introduction

In 1928, C.V. Raman, together with K.S. Krishnan, observed for the first time the inelastic scattering of an electromagnetic field from vibrating molecules in liquids. This process was named Raman effect by one of its discoverers [1]. Even though the potential application for molecular spectroscopy was clear from the beginning, it was not until the invention of laser in 1960s that its technical implementation became possible. After that, the Raman effect became one of the most popular ways to perform molecular analysis. However, the main drawback of this technique is the slowness of data acquisition, due to its incoherent nature, which prevents fast imaging. A solution to this problem arose in 1962, when the first Coherent Raman effect, namely Stimulated Raman Scattering (SRS), was serendipitously discovered by Eckhardt [2]. This breakthrough was made possible once again by the invention of the ruby-laser [3], since high flux density, of the order of 10^8 W/cm^2, which can be achieved only through stimulated emission of radiation, are needed to induce Coherent Raman effects. Shortly afterwards, thanks to the study of nonlinear wave mixing performed by Yajima and Takatsuji in 1964 [4] and by Maker and Terhune in 1965 [5], a new four-wave mixing process that could be made resonant with a molecular vibration was discovered. This process took the name of Coherent anti-Stokes Raman scattering (CARS). Both stimulated Raman scattering (SRS) and CARS light-matter interaction processes have been extensively discussed and exploited in the context of nonlinear optical spectroscopy since this early period and up to the early 1980s [6–11]. In 1982, the first implementation of CARS in the context of imaging was reported by Duncan, who developed the first CARS microscope using a non-collinear geometry [12]. The first biological applications of CARS imaging arose in 1999, when Xie's group developed a novel CARS microscope characterised by a collinear geometry of two laser beams and raster scanning at near-infrared wavelengths [13]. The use of collinear geometry and near infrared wavelengths greatly simplified the instrumentation and the biocompatibility, triggering many applications and innovations. While CARS microscopes were invented in the early 1980s, it was only in 2007 that the first SRS microscope was developed [14], since

only after the invention of sophisticated detection instruments, such as lock-in amplifier, it was possible to measure SRS signals at reasonable pixel dwell times. In 2008, Xie's group reported a high-speed SRS microscope for biological imaging [15]. Nowadays, Coherent Raman scattering microscopy is a potent method for revealing the chemical mechanisms within living cells and functional materials.

1.2. Introduction

Nowadays, optical microscopy is one of the most exploited methods to perform imaging of biological samples. This powerful technique allows one to visualize morphological details in cells and tissues up to the micrometer scale [16]. Optical microscopy offers high resolution and it does not need sample fixation, allowing one to work on unprocessed specimens or *in vivo*. However, in biological samples, it is often necessary to introduce probes to distinguish what is interesting (signal) from what is not (background). Fluorescence microscopy is the quintessential example, as it aims to reveal only the objects of interest in an otherwise black background. Fluorescence imaging has taken the lead in microscopy used for biology because of its inherent selectivity. Organic chemists have developed countless fluorescent probes during the past few decades, enabling the labeling of almost any component of biological systems that can be imaged [17].

Fluorescence microscopy features a superb sensitivity up to the single-molecule limit thanks to the use of exogenous (such as dyes or semiconductor quantum dots [18]) or endogenous (such as fluorescent proteins [19]) markers. However, the addition of fluorescent markers inevitably perturbes the sample, especially when small molecules are analyzed, since in this case the size of the probes is often bigger than the investigated system and interferes with its biological functions [20]. Furthermore, fluorescent microscopy suffers from two intrinsic limitations [21]: photobleaching and phototoxicity [22]. Cells are particularly vulnerable to phototoxicity [23], especially with short-wavelength light stimulation, which is further worsened by reactive chemical species produced by the fluorescent probes under illumination.

These factors make intrinsic, label-free imaging approaches necessary for a wide range of issues in the biological sciences and biomedicine. These methods don't require the inclusion of any fluorescent molecules. Every element of a biological sample, such as a cell or tissue, has a vibrational spectrum that represents its molecular structure and offers an endogenous unique signature that can be used for identification of its chemical constituents. The vibrational transitions are directly resonant with mid-infrared (MIR) wavelengths (λ = 3-20 μm). Vibrational absorption microscopy [24] exploits this kind

of light to retrieve the vibrational information. However, the required long wavelengths have a limited penetration depth due to water absorption, and low spatial resolution [20]. Spontaneous Raman (SR) microscopy overcomes these restrictions, since it uses visible or near-infrared (NIR) light, which offers far higher penetration depth and spatial resolution than its MIR equivalent [25]. SR exploits quasi-monochromatic laser light at frequency ω_P (pump frequency) in the visible or near-infrared (NIR) to excite a molecule to a virtual state, from which it relaxes to the ground state emitting a photon with lower energy at frequency ω_S (Stokes frequency) [1]. As depicted in fig. 1.1a, the Stokes frequency, $\omega_S = \omega_p - \Omega$, is red shifted in frequency and carries the vibrational information at frequency Ω. The resulting vibrational spectrum (fig. 1.1b) consists in a superposition of peaks, each representing a specific chemical bond. Each vibrational spectrum could be divided into three main regions: the fingerprint region (500-1800 cm^{-1}), that has a higher number of peaks and is considered to be the most informative one since many contributions from proteins and nucleic acids can be observed in this interval, the silent region (1800-2800 cm^{-1}), that has no peaks, and the carbon-hydrogen (C-H) stretching region (2800-3100 cm^{-1}).

[1] If the molecule is already in a vibrational state, after a further excitation due to the pump beam, it relaxes to the ground state emitting an anti-Stokes photon at frequency $\omega_{AS} = \omega_p + \Omega$. However, performing imaging of biological samples at room temperature (considering a Boltzmann distribution of the population among the vibrational levels), the anti-Stokes signal is much weaker than its Stokes counterpart, since the ground level is much more populated than the other vibrational states. The Stokes signal is thus preferred.

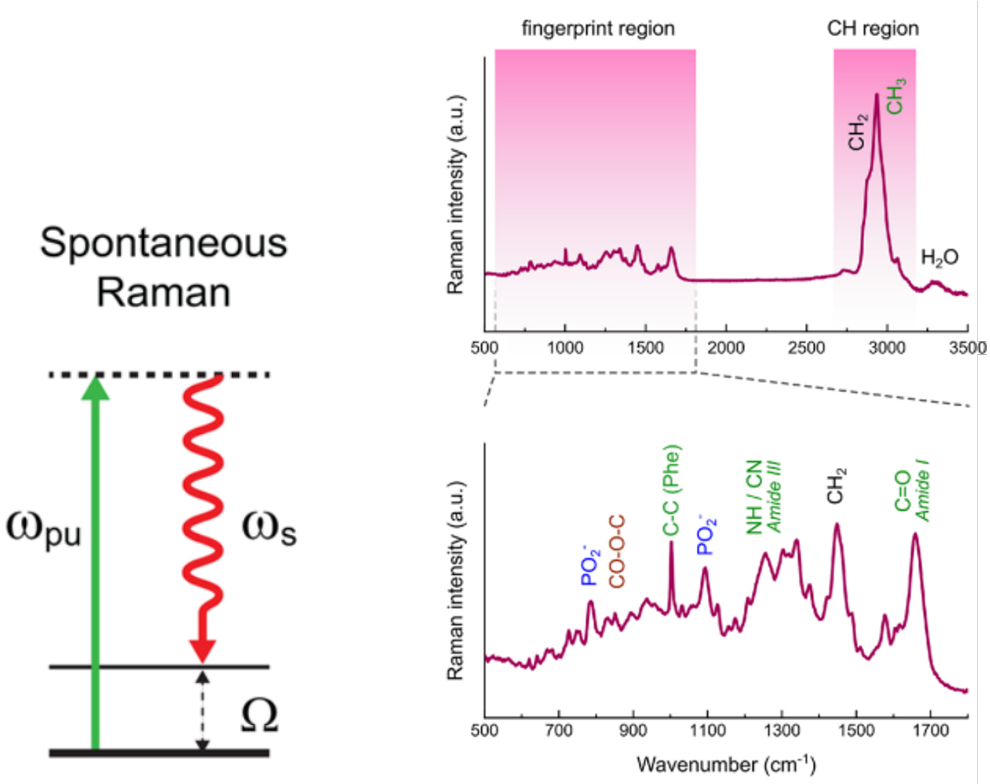

(a) Jablonsky diagram of Spontaneous Raman.

(b) Raman vibrational spectrum.

Figure 1.1: (a) Schematic of energy levels involved in Spontaneous Raman. Graph taken from: [20]. (b) Example of Raman vibrational spectra, highlighting the fingerprint region and the relevant biological peaks. Graph taken from: [26]

Analyzing a Raman spectrum it is possible to chemically identify many biomolecules contained in cells and tissues [27, 28]. SR can distinguish between normal and malignant states in skin, bladder, and gastric tissues, rat fibroblast cells, human bone, and human epithelial cells from a number of organs. It can also detect biochemical abnormalities in radioirradiated cells [20]. Furthermore, there are numerous encouraging reports of the diagnostic efficacy of this technique in cancer research [26, 29–34].

However, as a result of the very low scattering cross section of SR microscopy, which is around 10-12 orders of magnitude lower than the absorption cross section of molecules, a weak, incoherent signal is released isotropically from the irradiated material. This involves several consequences:

- It is challenging to distinguish the weak inelastically scattered SR light from the sample fluorescence, which creates a broad baseline to be removed using post-processing

techniques;

- It is difficult to use SR to investigate diluted species, due to the low signal-to-noise ratio (SNR);
- Image acquisition periods are too long due to the lengthy integration times needed (seconds or even minutes to generate Raman spectra with a satisfactory SNR) and thus prevents real-time imaging of dynamical processes in living cells or tissues.

Coherent Raman Scattering (CRS) [35, 36] overcomes these limitations exploiting third-order nonlinear optical processes which allow generating a signal higher than the SR one up to a factor of 10^7. These processes rise when two ultrashort light pulses, pump (at ω_P) and a red-shifted Stokes (at ω_S), interact with a medium simultaneously. When the difference between the two frequencies, $\Omega = \omega_P - \omega_S$ matches a vibrational frequency of the sample, a collective molecular oscillation is induced in the focal volume. Unlike in the SR process, the molecules in this case vibrate coherently, emitting a coherent and stronger signal, which propagates along a phase-matched direction, making it also easier to detect. Many advantages come from CRS with respect to SR or fluorescence microscopy:

- CRS produces a significantly stronger signal than SR microscopy due to a coherent superposition of the vibrational responses from the excited oscillators, which enables substantially faster imaging speeds;
- Unlike fluorescence microscopy, which uses fluorophores and stainings, CRS is a label-free microscopy which allow for the study of unperturbed cells and tissues;
- It normally operates without population transfer into the molecule's electronic excited states, limiting the photobleaching of biological substances;
- Similar to multi-photon fluorescence microscopy [37], CRS is a nonlinear microscopy technique and the signal is only created in the focal volume, demonstrating 3D sectioning capacity without the requirement for any physical confocal apertures [38];
- In comparison to the visible range, excitation in the NIR (700-1200 nm) has the benefit of having relatively low light absorption by tissues *in vivo* and reduced light scattering by turbid media, making it possible to investigate thick tissues at higher penetration depths (typically in the 0.1-1 mm range) [20]. Reduced phototoxicity and tissue damage are also other advantages of shifting the wavelength of the beams toward infrared.

The most relevant CRS implementations are Coherent anti-Stokes Raman scattering

(CARS)[12, 13, 39] and Stimulated Raman Scattering (SRS)[14, 15, 40].

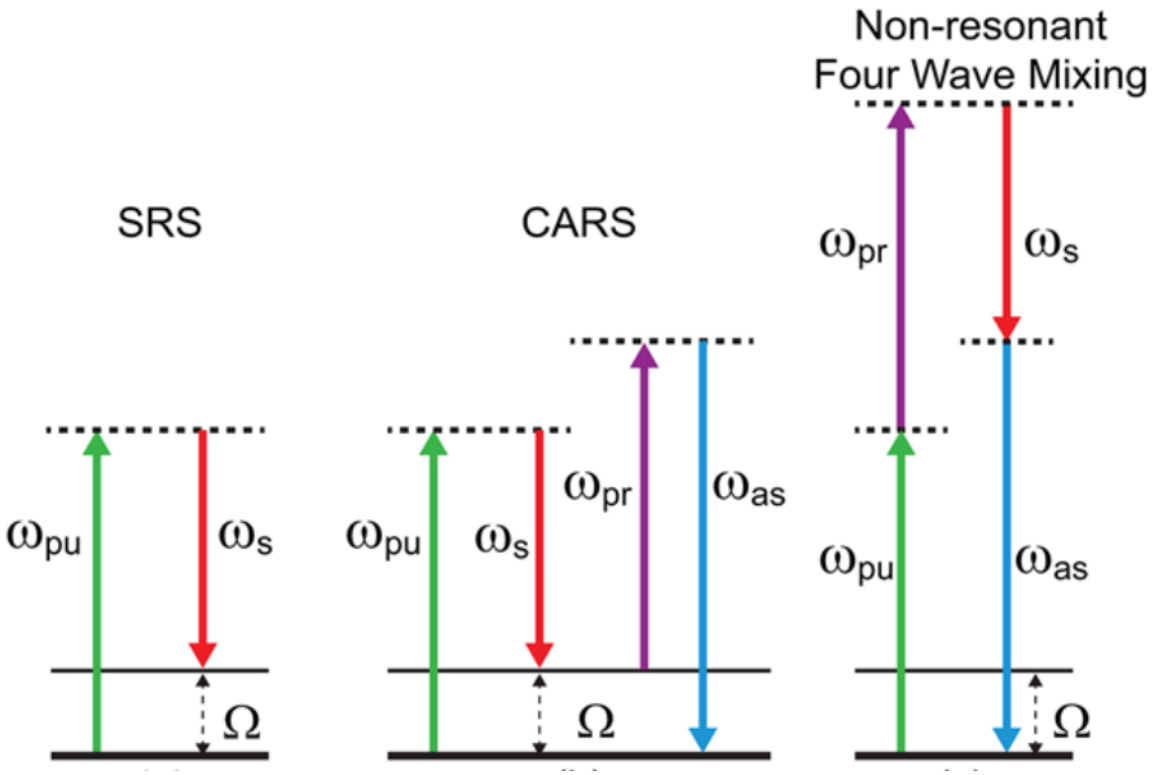

Figure 1.2: Schematic of energy levels involved in SRS, CARS and non-resonant background (NRB). Graphs taken from: [20].

In fig. 1.2 the Jablonski diagrams of SRS, CARS and non-resonant background (NRB) are reported. In the SRS process, coherent interaction with the sample drives stimulated emission from a virtual state to the probed vibrational state, which causes a Stokes-field amplification (stimulated Raman gain, SRG) and a concurrent pump-field attenuation (stimulated Raman loss, SRL). In the CARS process, the vibrational coherence is read by an encounter with a probe beam at frequency ω_{PR}, producing coherent radiation at the anti-Stokes frequency $\omega_{AS} = \omega_{PR} + \Omega$ (usually, $\omega_{PR} = \omega_{PU}$ is used so that $\omega_{AS} = \omega_{PU} + \Omega$).

Both CARS and SRS have benefits and downsides. SRS is superior to CARS in terms of molecular contrast and quantification. Particularly, since the SRS intensity is directly proportional to the imaginary part of the resonant third order susceptibility, it exhibits linear dependance to the analyte concentration and a spectral lineshape directly comparable to the SR signal allowing for the simple application of spectral data bases created for spontaneous Raman data to SRS [41]. However, SRS signal is read on top of the original pump or Stokes beams, calling for modulation transfer techniques, which are quite complicated in their implementation.

By contrast, due to the presence of a non-resonant background (NRB) deriving from a four wave mixing process, which interferes with the resonant signal, CARS spectral line shape results distorted and the peaks are shifted in position. Sophisticated algorithms like Kramers-Kronig or Maximum-Entropy method and expensive calculations are required to extract the pure vibrational information that can be compared to the SR spectrum [42]. On the other hand, implementing CARS into standard laser scanning microscopes is more feasible since neither laser modulation of one of the lasers nor special detectors and sophisticated frequency-selective amplifiers like lock-in amplifiers (LIA) or tuned amplifiers (TAMP) are needed [41]. Moreover, a higher-order nonlinear dependence on the excitation laser intensity makes the spatial resolution of CARS microscopy possibly higher, and high resolution imaging systems appear feasible [43]. Since CARS and SRS present advantages and disadvantages, both are actively being researched in light of potential uses.

Extremely high acquisition speeds have already been demonstrated for both CARS and SRS, reaching the video-rate [44, 45], in the single-frequency regime. In this regime, pump and Stokes pulses are characterized by a narrow bandwidth, covering few wavenumbers (which is the typical width of Raman peaks), and a picosecond duration. The difference in frequency $\Omega = \omega_P - \omega_S$ matches a specific vibrational transition, allowing to track the presence of specific molecules, with rather isolated Raman peaks. However, the single-frequency technique does not allow to identify or distinguish different species in complex systems such as biological samples, since the spectral information is incomplete and several biological peaks are overlapped. The best way to overcome these limits is broadband CRS microscopy. The main goal of broadband CRS microscopy is to retain the same amount of information given by SR, but at higher acquisition speed, comparable to its single-frequency counterpart. Two possible modalities to implement this technique are available:

- Hyperspectral CRS: in this case narrowband pulses are exploited and the frequency detuning is rapidly scanned to build a complete SRS/CARS spectrum;
- Multiplex CRS: in this case one of the pulses presents a broad bandwidth, allowing to stimulate several vibrational modes at the same time.

The last configuration will be analyzed and experimentally exploited in the following. In multiplex broadband CARS, a broadband Stokes pulse and a narrowband pump pulse are used to shine the sample. Their interaction populates several vibrational levels, as can be seen in fig. 1.3 (a). Afterwards, another interaction with the pump beam, which is characterized by a longer temporal duration (in the picosecond regime), excites the

system to a multitude of virtual levels. Finally, the system goes back to the ground state, emitting the CARS signal. It is remarkable that the bandwidth of the pump beam determines the spectral resolution, therefore, it is desirable to keep it in the order of few wavenumbers. On the contrary, in SRS, the vibrational signature can either be detected as a frequency-dependent Stokes amplification (SRG) or as a frequency-dependent pump attenuation (SRL). One can then choose to either resort to a narrowband pump and a broadband Stokes signal (SRG detection, fig. 1.3 (b),(d)), or a narrowband pump and a broadband Stokes signal (SRL detection, fig. 1.3 (c),(e)).

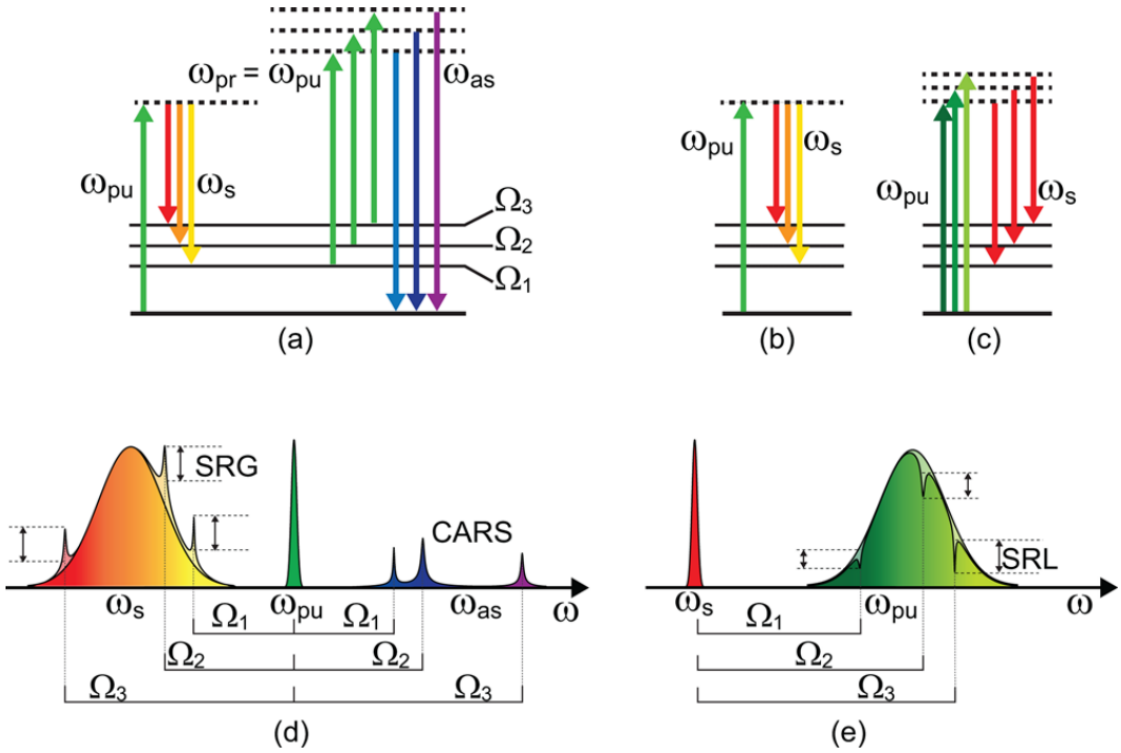

Figure 1.3: Schematic of energy levels and fields involved in: (a) broadband CARS; (b) SRS with broadband Stokes; (c) SRS with broadband pump. Pump/Stokes spectra and nonlinear signals for the cases of (d) broadband Stokes and (e) broadband pump. [20].

In the literature, several multiplex B-CARS microscopy setups have been realized. The majority work in the C-H region [46], due to the higher concentration of oscillators. Despite improvements in the detection systems, there are still problems in the acquisition of Raman spectra in the fingerprint region, since the signal in this area is much weaker. Some application of multiplex B-CARS setups covering the fingerprint region have been realized[47–51]. In order to successfully probe the most informative spectral area, supercontinuum light must be generated and exploited as a broadband Stokes pulse.

Supercontinuum generation is usually achieved in a tapered fiber [52] or a photonic crystal fiber (PCF) [53, 54].

The detection of the signal can be performed in various ways:

- Exploiting a time-domain Fourier transform approach [55–57]. Hashimoto *et al.* achieved the record speed of 24000 spectra/s [56];
- Using frequency combs [58]. Ideguchi *et al.* managed to perform high-speed measurement (3400 spectra/s);
- Detecting the signal in the frequency domain [47], simply using a spectrometer dispersing the anti-Stokes components and a CCD. This approach is limited by the CCD readout time, which is around 1 ms.

In this thesis, an innovative experimental configuration for multiplex ultra-broadband CARS with supercontinuum (SC) generation in bulk media is described and the experimental results are shown.

SC in bulk media represents a more compact, reliable, easy-to-use, and alignment-insensitive approach. It exhibits exceptional long-term stability that approaches that of the pump laser source itself, strong mutual correlations between the intensities of its spectrum components, and low pulse-to-pulse fluctuations, as demonstrated by Dubietis *et al.*[59]. With this innovative approach, we managed to cover the entire Raman-active region, from 500 to 3100 cm^{-1}. We reached high-speed detection, being able to acquire more than 1000 spectra/s, when performing spectroscopy on solvents, subcellular acids and solid state materials, such as Lithium Niobate. We then performed imaging of plastic beads, testing imaging capability of the setup, and biological samples.

The work is organized as follows:

- In chapter 2 we will start from the theoretical derivation of the propagation equation of light in media. We will proceed analyzing the non linear processes up to the third order. Afterwards, we will describe the coherent Raman scattering phenomena, dwelling on CARS, analyzing in particular B-CARS, Two and three colors CARS, time-delayed CARS and Epi-CARS. Finally, we will describe supercontinuum generation techniques, especially in bulk media.
- In chapter 3 we will introduce the experimental set-up. Then, we will characterize the sources exploiting frequency resolved optical gating (FROG). We will describe the data processing, analyzing in particular the noise reduction, the NRB removal techniques and the Multivariate curve resolution (MCR) algorithm. Finally, we

will show the experimental results obtained applying our setup on several samples. In particular, spectroscopy on solvents, subcellular acids and Lithium Niobate and imaging of plastic beads and biological samples will be shown. Both Two and three-color CARS spectra will be analyzed and a time-delayed CARS measurement will be shown as a proof of concept.

2 | Theory

In this chapter the basic theory regarding the studied processes is presented. We will start from the Maxwell equations, describing the propagation of pulses in linear media. Afterwards, we will analyze the non-linear optical processes up to the third order, describing the coherent Raman scattering phenomena in details, dwelling on CARS. Finally, supercontinuum (SC) light generation will be described, pointing out the advantages of SC generation in bulk media.

2.1. Linear optics

2.1.1. Propagation equation

In order to study the optical processes described in the next sections, it is necessary to start from Maxwell's wave equations, aiming to derive the propagation equation of light in vacuum or in dielectric media. Maxwell's equations read:

$$\begin{cases} \nabla \cdot \boldsymbol{D} = \rho, & \text{(2.1a)} \\ \nabla \times \boldsymbol{E} = -\dfrac{\partial \boldsymbol{B}}{\partial t}, & \text{(2.1b)} \\ \nabla \cdot \boldsymbol{B} = 0, & \text{(2.1c)} \\ \nabla \times \boldsymbol{H} = \dfrac{\partial \boldsymbol{D}}{\partial t} + \boldsymbol{J}. & \text{(2.1d)} \end{cases}$$

Where $\mathbf{D}$ is the electric displacement field, ρ is the net free charge density, $\mathbf{B}$ is the magnetic induction field, $\mathbf{E}$ is the electric field, $\mathbf{H}$ is the magnetic field and $\mathbf{J}$ is the conduction current density.

In addition to the Maxwell equations, we shall consider the constitutive equations as well:

$$\begin{cases} \boldsymbol{D} = \epsilon_0 \boldsymbol{E} + \boldsymbol{P}, & \text{(2.2a)} \\ \boldsymbol{B} = \mu_0 (\boldsymbol{H} + \boldsymbol{M}), & \text{(2.2b)} \end{cases}$$

Where **P** is the polarization field, namely the volumetric density of electric dipole moments, while **M** is the magnetization field, that is the volumetric density of magnetic dipole moments [60].

Exploiting the Maxwell equations, it is possible to derive the magnetic field from the electric one and viceversa. Hence, it is enough to focus on just one of the two. In particular, the electric field propagation equation will be derived.

Starting from (2.1b), we vectorially multiply both sides by the nabla operator ∇, obtaining:

$$\nabla \times (\nabla \times \boldsymbol{E}) = -\nabla \times (\frac{\partial \boldsymbol{B}}{\partial t}), \tag{2.3}$$

Hence, considering that the ∇ operator and $\frac{\partial}{\partial t}$ commute, since there is no relationship among space and time derivatives, we can write (2.3) as:

$$\nabla \times (\nabla \times \boldsymbol{E}) = -\frac{\partial}{\partial t}(\nabla \times \boldsymbol{B}), \tag{2.4}$$

Whence, substituting (2.2b), (2.4) becomes:

$$\nabla \times (\nabla \times \boldsymbol{E}) = -\frac{\partial}{\partial t}\left[\nabla \times (\mu_0 \boldsymbol{H} + \mu_0 \boldsymbol{M})\right] = -\mu_0 \frac{\partial}{\partial t}(\nabla \times \boldsymbol{M}) - \mu_0 \frac{\partial}{\partial t}(\nabla \times \boldsymbol{H}), \tag{2.5}$$

Now, exploiting (2.1d), and substituting it in (2.5), we obtain:

$$\nabla \times (\nabla \times \boldsymbol{E}) = -\mu_0 \frac{\partial}{\partial t}(\nabla \times \boldsymbol{M}) - \mu_0 \frac{\partial}{\partial t}\left[\boldsymbol{J} + \frac{\partial \boldsymbol{D}}{\partial t}\right], \tag{2.6}$$

We can now proceed substituting (2.2a) in (2.6) finding:

$$\nabla \times (\nabla \times \boldsymbol{E}) = -\mu_0 \frac{\partial}{\partial t}(\nabla \times \boldsymbol{M}) - \mu_0 \frac{\partial \boldsymbol{J}}{\partial t} - \mu_0 \frac{\partial^2}{\partial t^2}[\epsilon_0 \boldsymbol{E} + \boldsymbol{P}], \tag{2.7}$$

Knowing that $\epsilon_0 \mu_0 = \frac{1}{c^2}$, where c is the speed of light, and reorganizing the terms in (2.7), we find:

$$\nabla \times (\nabla \times \boldsymbol{E}) + \frac{1}{c^2}\frac{\partial^2 \boldsymbol{E}}{\partial t^2} = -\mu_0 \frac{\partial}{\partial t}(\nabla \times \boldsymbol{M}) - \mu_0 \frac{\partial \boldsymbol{J}}{\partial t} - \mu_0 \frac{\partial^2 \boldsymbol{P}}{\partial t^2}, \tag{2.8}$$

Equation (2.8) represents the exact propagation equation in a medium, where three different source terms can be identified. It is now possible to introduce some approximations, in order to solve the propagation equation[60].

We can safely consider $\frac{\partial}{\partial t}(\nabla \times \boldsymbol{M}) \approx 0$, which is a valid approximation for the non-magnetic materials, or when the magnetization does not change abruptly in space and time.

Furthermore, we shall assume $\rho \approx 0$ (no net free charges approximation). This approximation is valid until the electrons are not separated from the corresponding atoms. In order to introduce this approximation in the propagation equation we shall further develop the left-hand side of (2.8) with the well known relation:

$$\nabla \times (\nabla \times \boldsymbol{E}) = \nabla(\nabla \cdot \boldsymbol{E}) - \nabla^2 \boldsymbol{E} \tag{2.9}$$

Where, substituting (2.2a) in (2.1a), reorganizing the terms and considering the no net free charges approximation we find:

$$\nabla \cdot \boldsymbol{E} = \frac{\rho - \nabla \cdot \boldsymbol{P}}{\epsilon_0} \approx -\frac{\nabla \cdot \boldsymbol{P}}{\epsilon_0} \tag{2.10}$$

Introducing (2.9) and (2.10) in the propagation equation for non magnetic media we obtain:

$$-\nabla^2 \boldsymbol{E} + \frac{1}{c^2}\frac{\partial^2 \boldsymbol{E}}{\partial t^2} = -\mu_0 \frac{\partial \boldsymbol{J}}{\partial t} - \mu_0 \frac{\partial^2 \boldsymbol{P}}{\partial t^2} + \nabla\left[\frac{\nabla \cdot \boldsymbol{P}}{\epsilon_0}\right], \tag{2.11}$$

We can proceed further considering homogeneous media, where refractive index does not show significant discontinuities. Through this approximation we can consider the polarization almost constant in space for the spatial scale considered, then: $\nabla \cdot \boldsymbol{P} \approx 0$

We can now introduce this approximation in (2.11) obtaining the propagation equation for homogeneous, non-magnetic media, with no free charges:

$$-\nabla^2 \boldsymbol{E} + \frac{1}{c^2}\frac{\partial^2 \boldsymbol{E}}{\partial t^2} = -\mu_0 \frac{\partial \boldsymbol{J}}{\partial t} - \mu_0 \frac{\partial^2 \boldsymbol{P}}{\partial t^2}, \tag{2.12}$$

Now, since we will consider mainly dielectric media at moderate powers (not enough to ionize the electrons), the conduction current density is almost equal to zero: $\boldsymbol{J} \approx 0$.

Therefore, applying this last approximation and changing the signs in (2.12), we obtain

the approximated propagation equation for homogeneous non-magnetic media at low-moderate powers:

$$\nabla^2 \boldsymbol{E} - \frac{1}{c^2}\frac{\partial^2 \boldsymbol{E}}{\partial t^2} = \mu_0 \frac{\partial^2 \boldsymbol{P}}{\partial t^2}, \tag{2.13}$$

In many cases other approximations could be introduced, such as non-birefringent media. In this kind of media the linear polarization of the electric field is preserved throughout the entire propagation, allowing to discard the vectorial nature of the fields:

$$\begin{cases} \boldsymbol{E} = E(\boldsymbol{r}, t), & \text{(2.14a)} \\ \boldsymbol{P} = P(\boldsymbol{r}, t) & \text{(2.14b)} \end{cases}$$

Then, introducing (2.14) in (2.13) we find the scalar propagation equation, namely:

$$\nabla^2 E - \frac{1}{c^2}\frac{\partial^2 E}{\partial t^2} = \mu_0 \frac{\partial^2 P}{\partial t^2}, \tag{2.15}$$

The last approximation which can be introduced is the Plane Wave Approximation (PWA). This approximation is particularly useful to understand the behaviour of light in matter, however, it is not applicable to the vast majority of real-life cases. Due to the Plane Wave Approximation, the electric field can be considered constant all over a plane perpendicular to the propagation direction, which can be considered along the z-axis without loss of generality, in this way the Laplacian operator can be significantly simplified as follows:

$$\nabla^2 E = \frac{\partial^2 E}{\partial x^2} + \frac{\partial^2 E}{\partial y^2} + \frac{\partial^2 E}{\partial z^2} = \frac{\partial^2 E}{\partial z^2}, \tag{2.16}$$

Within this approximation, we can apply (2.16) to (2.15) and the propagation equation can be written as:

$$\frac{\partial^2 E}{\partial z^2} - \frac{1}{c^2}\frac{\partial^2 E}{\partial t^2} = \mu_0 \frac{\partial^2 P}{\partial t^2}, \tag{2.17}$$

2.1.2. Linear Polarization

The polarization $\boldsymbol{P}$ appears in the propagation equation as a source term. It is linked to the the medium in which the light propagates and affects the incoming electric field. It can be divided in a linear, $\boldsymbol{P}^{(L)}$, and a non-linear, $\boldsymbol{P}^{(NL)}$, terms as:

$$\boldsymbol{P} = \boldsymbol{P}^{(L)} + \boldsymbol{P}^{(NL)}, \tag{2.18}$$

The polarization is defined as the volumetric density of dipole moments, however, in a macroscopic picture, it can be described by means of the electric susceptibility χ. We can now focus on the linear polarization, which is a valid approach for moderate intensities, where only $\boldsymbol{P}^{(L)}$ plays a role. The components of the linear polarization can be written as:

$$P_i^L(\boldsymbol{r}, t) = \epsilon_0 \int dx'\, dy'\, dz' \int_{-\infty}^{+\infty} dt' \chi_{ij}(\boldsymbol{r}, \boldsymbol{r'}, t, t') E_j(\boldsymbol{r'}, t'), \tag{2.19}$$

With $i = \{x, y, z\}$ and $j = \{x, y, z\}$ and where the integral in space is performed over the whole space. Note that the Einstein notation has been used in (2.19).[1] It is possible to observe that the polarization depends linearly on the electric field, but it is weighted by the susceptibility χ, which generally has a tensorial nature. Indeed, every component of the electric field contributes to every component of the polarization. Before plugging (2.19) in the propagation equation, some approximations are needed. In the next sections, we will consider media with the following characteristics:

1. Isotropic;
2. Time-invariant;
3. Homogeneous.

Considering only isotropic (and so non birefringent) media allows us to discard the tensorial nature of the susceptiblity. Moreover, for time-invariant and homogeneous media, the susceptibility can be further simplified as: $\chi(\boldsymbol{r}, \boldsymbol{r'}, t, t') = \chi(\boldsymbol{r} - \boldsymbol{r'}, t - t')$. The linear polarization can be written as:

$$\boldsymbol{P}^L(\boldsymbol{r}, t) = \epsilon_0 \int dx'\, dy'\, dz' \int_{-\infty}^{+\infty} dt' \chi(\boldsymbol{r} - \boldsymbol{r'}, t - t') \boldsymbol{E}(\boldsymbol{r'}, t'), \tag{2.20}$$

The polarization is the convolution in space and time of the electric field component of the light pulse with the susceptibility function. If we neglect the spatial dependence (which is valid in the plane wave approximation) of χ and the vectorial nature (as we did before) (2.20) is further simplified:

[1] Whenever an index is repeated in an expression, such as j in (2.19), a sum over that index is performed.

$$P^L(t) = \epsilon_0 \int_{-\infty}^{+\infty} dt' \chi(t'-t) E(t'), \tag{2.21}$$

We can now plug (2.21) in the propagation equation (for simplicity the last form of the propagation equation, that is (2.17), is considered):

$$\frac{\partial^2 E}{\partial z^2} - \frac{1}{c^2}\frac{\partial^2 E}{\partial t^2} = \mu_0 \epsilon_0 \frac{\partial^2}{\partial t^2} \int_{-\infty}^{+\infty} \chi(t-t') E(t')\, dt'. \tag{2.22}$$

The source term can be rewritten as a convolution in time, defined as:

$$\int_{-\infty}^{+\infty} f(t'-t) g(t')\, dt' = f(t) * g(t), \tag{2.23}$$

Therefore, taking into account (2.23) in (2.22), we find:

$$\frac{\partial^2 E}{\partial z^2} - \frac{1}{c^2}\frac{\partial^2 E}{\partial t^2} = \mu_0 \epsilon_0 \frac{\partial^2}{\partial t^2} \left[\chi(t) * E(t)\right]. \tag{2.24}$$

2.1.3. Helmoltz equation

In order to further proceed in the analysis, it is necessary to introduce the Fourier transform and some of its properties. Given a function in time $f(t)$, the Fourier transform of $f(t)$ is defined as:

$$F(\omega) = \mathcal{F}\left\{f(t)\right\} = \int_{-\infty}^{+\infty} f(t) e^{-i\omega t}\, dt, \tag{2.25}$$

While the anti-transform reads as follows:

$$f(t) = \mathcal{F}^{-1}\left\{F(\omega)\right\} = \int_{-\infty}^{+\infty} F(\omega) e^{+i\omega t} \frac{d\omega}{2\pi}, \tag{2.26}$$

The following properties hold [60]:

$$\mathcal{F}\left\{\frac{d^n f}{dt^n}\right\} = (i\omega)^n F(\omega), \tag{2.27}$$

$$\mathcal{F}\left\{\int_{-\infty}^{+\infty} f(t-t')g(t')\,dt'\right\} = \mathcal{F}\left\{f * g\right\} = \mathcal{F}\{f\}\mathcal{F}\{g\} = F(\omega)G(\omega), \tag{2.28}$$

$$\mathcal{F}(f(t)g(t)) = \mathcal{F}(f) * \mathcal{F}(g) = F(\omega) * G(\omega), \tag{2.29}$$

We can apply the Fourier transform (2.25) to both sides of (2.24) obtaining:

$$\mathcal{F}\left\{\frac{\partial^2 E}{\partial z^2} - \frac{1}{c^2}\frac{\partial^2 E}{\partial t^2}\right\} = \mu_0\epsilon_0\mathcal{F}\left\{\frac{\partial^2}{\partial t^2}\left[\chi(t) * E(t)\right]\right\}. \tag{2.30}$$

Applying (2.27) and (2.28), to (2.30) we find:

$$\frac{\partial^2\mathcal{F}\{E\}}{\partial z^2} - \frac{1}{c^2}(i\omega)^2\mathcal{F}\{E\} = \frac{1}{c^2}[(i\omega)^2\mathcal{F}\{\chi\}\mathcal{F}\{E\}]. \tag{2.31}$$

Where we also considered the well known relation: $\epsilon_0\mu_0 = \frac{1}{c^2}$. Introducing: $\tilde{E}(z,\omega) = \mathcal{F}\{E(z,t)\}$ and $\tilde{\chi}(\omega) = \mathcal{F}(\chi(t))$, it is possible to rewrite (2.31) as:

$$\frac{\partial^2\tilde{E}}{\partial z^2} + \frac{\omega^2}{c^2}\tilde{E} = -\frac{\omega^2}{c^2}\tilde{E}\tilde{\chi}. \tag{2.32}$$

Finally, reorganizing the terms in (2.32), retrieving the Helmoltz equation:

$$\frac{\partial^2\tilde{E}}{\partial z^2} + \frac{(1+\tilde{\chi})\omega^2}{c^2}\tilde{E} = 0. \tag{2.33}$$

In order to solve the Helmoltz equation (2.33), it is useful to introduce the dielectric function $\epsilon_r(\omega)$:

$$\epsilon_r(\omega) = 1 + \tilde{\chi}. \tag{2.34}$$

Where $\epsilon_r(\omega)$ is linked to the wavenumber $k(\omega)$ by means of the relation:

$$k^2(\omega) = \frac{\omega^2}{c^2}\epsilon_r(\omega). \tag{2.35}$$

Furthermore, since the dielectric function is linked to the refractive index $n(\omega)$ by the relation $\epsilon_r(\omega) = n^2(\omega)$, the wavenumber can also be written as:

$$k(\omega) = \frac{\omega}{c} n(\omega). \tag{2.36}$$

Introducing (2.34) and (2.35) in (2.33) we obtain:

$$\frac{\partial^2 \tilde{E}}{\partial z^2} + k^2(\omega)\tilde{E} = 0. \tag{2.37}$$

We found a harmonic oscillator equation (eq. (2.37)), which has two different solutions in the exponential form:

$$\tilde{E}_1(z,\omega) = \tilde{E}_1(0,\omega)e^{-ik(\omega)z}, \tag{2.38}$$

$$\tilde{E}_2(z,\omega) = \tilde{E}_2(0,\omega)e^{+ik(\omega)z}. \tag{2.39}$$

Equations (2.38) and (2.39) represent the forward and backward propagation respectively. Let us consider only the forward propagation. Starting from (2.38), we can find the solution of the propagation equation in linear, isotropic, homogeneous, time-invariant media applying the Fourier anti-transform (2.26) as follows:

$$E(z,t) = \mathcal{F}^{-1}\left\{\tilde{E}_1(z,\omega)\right\} = \int_{-\infty}^{+\infty} \tilde{E}_1(0,\omega)e^{i[\omega t - k(\omega)z]}\frac{d\omega}{2\pi}. \tag{2.40}$$

2.1.4. Propagation of pulses

In the previous calculations, we applied the Plane Wave Approximation. However, in the following, the propagation of pulses in media will be considered. A pulse can be represented as follows:

$$E(z,t) = A(z,t)\cos[\omega_0 t - k_0 z + \phi(z,t)], \tag{2.41}$$

This is called envelope representation of a pulse, where $A(z,t)$ is the envelope, $\cos[\omega_0 t - k_0 z + \phi(z,t)]$ is the carrier, ω_0 is the central frequency, k_0 is the central wavenumber, defined as $k_0 = \frac{\omega_0}{c} n(\omega_0)$, and $\phi(z,t)$ is the phase. The resulting shape is depicted in fig. 2.1.

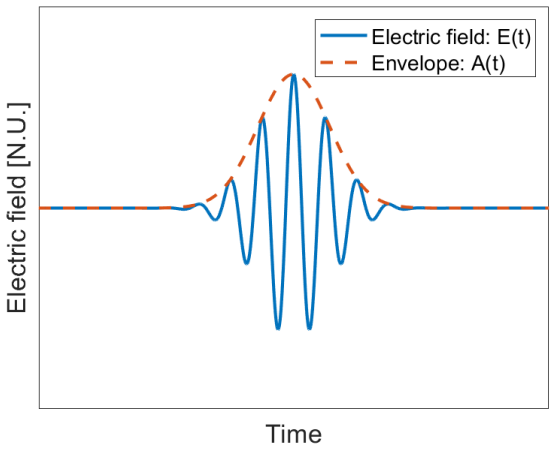

Figure 2.1: Envelope representation of a gaussian pulse.

Assuming $\phi(z=0,t)=0$, (2.41) at $z=0$ can be written as:

$$E(z=0,t)=A(z=0,t)\cos[\omega_0 t], \tag{2.42}$$

Since $E(z=0,t)$ is a real function, the following property of the Fourier transform holds:

$$\tilde{E}(0,-\omega)=\tilde{E}^*(0,\omega), \tag{2.43}$$

We can now proceed performing the Fourier transform of (2.42):

$$\tilde{E}(0,\omega)=\mathcal{F}\left\{A(0,t)\cos(\omega_0 t)\right\}=\mathcal{F}\left\{A(0,t)\right\}*\mathcal{F}\left\{\cos(\omega_0 t)\right\}, \tag{2.44}$$

Where we used the property (2.29). Let us consider the Fourier transform of $\cos(\omega_0 t)$:

$$\mathcal{F}\left\{\cos(\omega_0 t)\right\}=\frac{\delta(\omega-\omega_0)+\delta(\omega+\omega_0)}{2}, \tag{2.45}$$

Where δ is the Dirac delta. The following property of the Dirac delta holds:

$$f(x)*\delta(x-x_0)=f(x-x_0), \tag{2.46}$$

Exploiting (2.46) and knowing (2.45), we can rewrite (2.44) as:

$$\tilde{E}(0,\omega)=\frac{\tilde{A}(0,\omega-\omega_0)+\tilde{A}(0,\omega+\omega_0)}{2}, \tag{2.47}$$

Where $\tilde{A}(0,\omega) = \mathcal{F}\{A(z=0,t)\}$. Taking into account (2.43), we can write:

$$\tilde{A}(0,\omega-\omega_0) = \tilde{A}^*(0,\omega+\omega_0), \tag{2.48}$$

Therefore, due to (2.48):

$$\tilde{A}(0,\omega-\omega_0) + \tilde{A}(0,\omega+\omega_0) = 2Re\{\tilde{A}(0,\omega-\omega_0)\}, \tag{2.49}$$

Assuming that the bandwidth in frequency of $\tilde{A}(0,\omega)$ is much smaller compared to ω_0 and considering (2.49) we can rewrite (2.40) as:

$$E(z,t) = Re\left\{\int_0^{+\infty} \tilde{A}(\omega-\omega_0)\exp[i(\omega t - k(\omega)z)]\frac{d\omega}{2\pi}\right\}. \tag{2.50}$$

Let us consider the wavenumber $k(\omega)$. Since $\tilde{A}(0,\omega)$ is different from zero only close to ω_0, we can expand $k(\omega)$ in ω_0 as follows:

$$k(\omega) = k(\omega_0) + \left(\frac{dk}{d\omega}\right)_{\omega_0}(\omega-\omega_0) + \sum_{n=1}^{\infty}\frac{\beta_n}{n!}(\omega-\omega_0)^n, \tag{2.51}$$

Where the following definitions hold:

1. Phase velocity v_{ph}, defined as: $\frac{1}{v_{ph}} = \frac{k(\omega_0)}{\omega_0}$,
2. Group velocity v_g, defined as: $\frac{1}{v_g} = \left(\frac{dk}{d\omega}\right)_{\omega_0}$,
3. Group velocity dispersion (GVD) β_2, defined as: $\beta_2 = \left(\frac{d^2k}{d\omega^2}\right)_{\omega_0}$,
4. Third order dispersion (TOD) β_3, defined as: $\beta_3 = \left(\frac{d^3k}{d\omega^3}\right)_{\omega_0}$.

Therefore, we can develop (2.51) as:

$$k(\omega) = \frac{\omega_0}{v_{ph}} + \frac{(\omega-\omega_0)}{v_g} + \frac{1}{2}\beta_2(\omega-\omega_0)^2 + \frac{1}{6}\beta_3(\omega-\omega_0)^3 + \ldots, \tag{2.52}$$

In order to understand the role of the phase and group velocity, we can stop at the first order (that is the group velocity term) in (2.52) and plug it in (2.50), obtaining:

$$E(z,t) = Re\left\{\int_0^{+\infty} \tilde{A}(\omega-\omega_0)\exp\left[i\left(\omega t - \frac{\omega_0 z}{v_{ph}} - \frac{(\omega-\omega_0)z}{v_g}\right)\right]\frac{d\omega}{2\pi}\right\}. \tag{2.53}$$

Then, we can sum and subtract $\omega_0 t$ in the exponential in (2.53), and subsequently take out of the integral the terms which do not depend on ω:

$$\begin{aligned} E(z,t) &= Re\left\{\int_0^{+\infty} \tilde{A}(\omega-\omega_0)\exp\left[i\left(\omega t-\omega_0 t+\omega_0 t-\frac{\omega_0 z}{v_{ph}}-\frac{(\omega-\omega_0)z}{v_g}\right)\right]\frac{d\omega}{2\pi}\right\} = \\ &= Re\left\{\int_0^{+\infty} \tilde{A}(\omega-\omega_0)\exp\left[i\left(\left(t-\frac{z}{v_g}\right)(\omega-\omega_0)+\omega_0\left(t-\frac{z}{v_{ph}}\right)\right)\right]\frac{d\omega}{2\pi}\right\} = \\ &= Re\left\{\exp\left[i\omega_0\left(t-\frac{z}{v_{ph}}\right)\right]\int_0^{+\infty} \tilde{A}(\omega-\omega_0)\exp\left[i\left(\left(t-\frac{z}{v_g}\right)(\omega-\omega_0)\right)\right]\frac{d\omega}{2\pi}\right\}, \end{aligned} \tag{2.54}$$

Let us define $\omega' = \omega - \omega_0$, so $d\omega' = d\omega$. We can rewrite (2.54) as:

$$E(z,t) = Re\left\{\exp\left[i\omega_0\left(t-\frac{z}{v_{ph}}\right)\right]\int_{-\omega_0}^{+\infty} \tilde{A}(\omega')\exp\left[i\left(\left(t-\frac{z}{v_g}\right)\omega'\right)\right]\frac{d\omega'}{2\pi}\right\}, \tag{2.55}$$

Since $\tilde{A}(\omega')$ is different from zero only close to $\omega' \approx 0$, we can extend the lower limit of the integral from $-\omega_0$ to $-\infty$ without changing the result. In this way (2.55) becomes:

$$\begin{aligned} E(z,t) &= Re\left\{\exp\left[i\omega_0\left(t-\frac{z}{v_{ph}}\right)\right]\int_{-\infty}^{+\infty} \tilde{A}(\omega')\exp\left[i\left(\left(t-\frac{z}{v_g}\right)\omega'\right)\right]\frac{d\omega'}{2\pi}\right\} = \\ &= Re\left\{\exp\left[i\omega_0\left(t-\frac{z}{v_{ph}}\right)\right]\mathcal{F}^{-1}\left\{\tilde{A}(\omega')\right\}_{t'=t-z/v_g}\right\}, \end{aligned} \tag{2.56}$$

Where $\mathcal{F}^{-1}\left\{\tilde{A}(\omega')\right\}_{t'=t-z/v_g}$ is the Fourier anti-transform in $t - z/v_g$. Finally, defining the group delay τ_g as $\tau_g = \frac{z}{v_g}$ and the phase delay τ_{ph} as $\tau_{ph} = \frac{z}{v_{ph}}$we can write (2.56) as:

$$E(z,t) = A(t-\tau_g)\cos[\omega_0(t-\tau_{ph})] \tag{2.57}$$

In general $\tau_g \neq \tau_{ph}$, and this results in a slippage of the optical carrier with respect to

the envelope. Let us define the Carrier-Envelope Phase Offset (CEP) in order to quantify this mismatch:

$$CEP : \Delta\Psi = \omega_0(\tau_g - \tau_{ph}) \tag{2.58}$$

2.1.5. Group velocity dispersion

The goal of this section is to understand the role of the Group velocity dispersion and its effects on the propagation of a pulse trough a medium. Hence, we will start from (2.50), developing $k(\omega)$ to the second order (namely, the GVD term):

$$E(z,t) = Re\left\{\int_0^{+\infty} \tilde{A}(\omega-\omega_0)\exp\left[i\left(\omega t - \frac{\omega_0 z}{v_{ph}} - \frac{(\omega-\omega_0)z}{v_g} - \frac{1}{2}\beta_2 z(\omega-\omega_0)^2\right)\right]\frac{d\omega}{2\pi}\right\}. \tag{2.59}$$

Let us consider a Gaussian pulse as the simplest case of pulse:

$$E(z,t) = E_0 \exp\left[-\frac{t^2}{2\tau_p^2}\right]\cos(\omega_0 t), \tag{2.60}$$

The intensity of the Gaussian pulse can be calculated from (2.60) obtaining:

$$I(z,t) = I_0 \exp\left[-\frac{t^2}{\tau_p^2}\right], \tag{2.61}$$

Where τ_p is a constant related to the temporal duration Δt_{FWHM} (where FWHM stands for Full Width at Half Maximum, as it can be seen in fig. 2.2) by means of the relation:

$$\Delta t_{FWHM} = \tau_p\sqrt{2\ln(2)}, \tag{2.62}$$

Which could be easily derived putting the right-hand side of (2.61) equal to $I_0/2$.

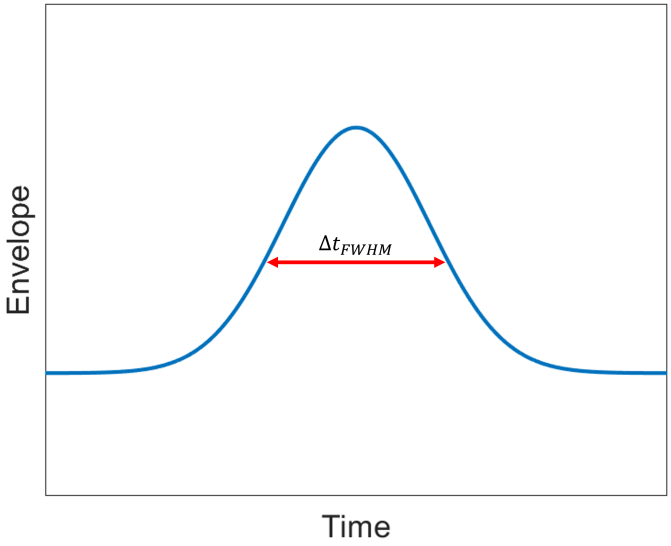

Figure 2.2: Gaussian pulse and its full width at half maximum in time.

An example of gaussian pulse is reported in fig. 2.2, where the FWHM in time has been highlighted. In order to plug the Gaussian pulse in (2.50), it is necessary to calculate the Fourier transform of its envelope:

$$\mathcal{F}\left\{E_0 \exp\left[-\frac{t^2}{2\tau_p^2}\right]\right\} = \tau_p\sqrt{2\pi}\exp\left(-\frac{\omega^2\tau_p^2}{2}\right) = \tilde{A}(\omega), \tag{2.63}$$

Therefore, substituting ω with $\omega - \omega_0$ in (2.63), we find:

$$\tilde{A}(\omega-\omega_0) = \tau_p\sqrt{2\pi}\exp\left(-\frac{(\omega-\omega_0)^2\tau_p^2}{2}\right), \tag{2.64}$$

We can now plug (2.64) in (2.59), obtaining:

$$E(z,t) = Re\left\{\int_0^{+\infty} E_0\tau_p\sqrt{2\pi}\exp\left(-\frac{(\omega-\omega_0)^2\tau_p^2}{2}\right)\right.$$
$$\left.\exp\left[i\left(\omega t - \frac{\omega_0 z}{v_{ph}} - \frac{(\omega-\omega_0)z}{v_g} - \frac{1}{2}\beta_2 z(\omega-\omega_0)^2\right)\right]\frac{d\omega}{2\pi}\right\}. \tag{2.65}$$

We can now define a new quantity: $\tilde{\tau}_p^2 \equiv \tau_p^2 + i\beta_2 z$. Therefore (2.65) becomes:

$$E(z,t) = Re\left\{\int_0^{+\infty} E_0\tau_p\sqrt{2\pi}\exp\left(-\frac{(\omega-\omega_0)^2\tilde{\tau}_p^2}{2}\right)\exp\left[i\left(\omega t - \frac{\omega_0 z}{v_{ph}} - \frac{(\omega-\omega_0)z}{v_g}\right)\right]\frac{d\omega}{2\pi}\right\}. \tag{2.66}$$

We can now sum and subtract $\omega_0 t$ in the exponential in (2.66) and define $\omega' = \omega - \omega_0$, as we did in (2.54), finding:

$$E(z,t) = Re\left\{\exp\left[i\omega_0\left(t - \frac{z}{v_{ph}}\right)\right]\int_{-\omega_0}^{+\infty}\tilde{A}(\omega')\exp\left[i\left(\omega'\left(t-\frac{z}{v_g}\right)\right)\right]\frac{d\omega}{2\pi}\right\}. \tag{2.67}$$

It is possible to observe that the integral in (2.67) represents the Fourier anti-transform of $\tilde{A}(\omega')$ (where τ_p was substituted by $\tilde{\tau}_p$), centered in $t' = t - \frac{z}{v_g}$. Therefore, we can proceed as follows:

$$\mathcal{F}^{-1}\left\{\tilde{A}(\omega')\right\} \propto \mathcal{F}^{-1}\left\{\exp\left[-\frac{\omega'\tilde{\tau}_p^2}{2}\right]\right\} \propto \exp\left[-\frac{t'}{2\tilde{\tau_p}^2}\right] \tag{2.68}$$

After some calculations, (2.68) becomes:

$$\mathcal{F}^{-1}\left\{\tilde{A}(\omega')\right\} \propto \exp\left[-\frac{t'^2\tau_p^2}{2[\tau_p^4+\beta_2^2 z^2]}\right]\exp\left[-\frac{i\beta_2 z t'^2}{2[\tau_p^4+\beta_2^2 z^2]}\right] \tag{2.69}$$

Plugging (2.69) in (2.67) and taking only the real part, we obtain a Gaussian pulse described by:

$$E(z,t) \propto \exp\left[-\frac{(t-\frac{z}{v_g})^2}{2\tau_p^2(z)}\right]\cos\left[\omega_0\left(t-\frac{z}{v_{ph}}\right) + \frac{z(t-\tau_g)^2}{2L_D\tau_p^2(z)}\right]. \tag{2.70}$$

Where, in eq. (2.70), $L_D \equiv \frac{\tau_P^2}{\beta_2}$ is the dispersion length and $\tau_p^2(z) \equiv \tau_p^2\left[1+\left(\frac{z}{L_D}\right)^2\right]$ is related to the pulse duration depending on the position z. In conclusion, we found out that a Gaussian pulse maintains the Gaussian shape during the propagation in a medium with second order dispersion β_2. However, the pulse duration Δt_{FWHM}, calculated using (2.62), changes during the propagation as:

$$\Delta t_{FWHM} = \tau_p(z)\sqrt{2\ln(2)} = \tau_p \left| \sqrt{1 + \left(\frac{z}{L_D}\right)^2} \sqrt{2ln(2)} \right| \tag{2.71}$$

We can distinguish two extreme cases in (2.71):

1. $z \ll L_D \Rightarrow \tau_p(z) \approx \tau_p$
2. $z \gg L_D \Rightarrow \tau_p(z) \approx \frac{\tau_p z}{L_D} = \frac{|\beta_2|z}{\tau_p}$

Therefore, for distances much smaller than the dispersion length, the pulse duration is almost constant. However, for greater distances, the pulse duration increases with z. A representation of a gaussian pulse before and after propagation is depicted in figure 2.3.

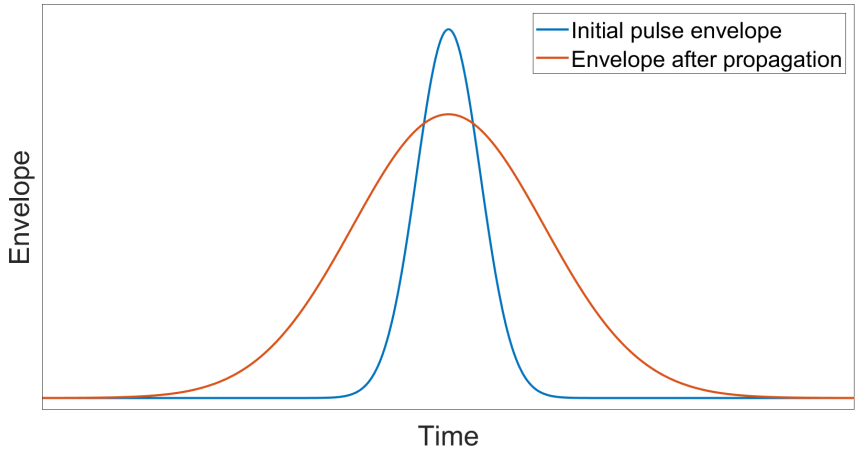

Figure 2.3: Envelope of a gaussian pulse before and after propagation.

Furthermore, in the latter case, the smaller is the initial duration, the faster it will increase: shorter pulses are more "fragile", that is, they tend to broaden in time in a faster way.

Another consequence of the presence of the second order dispersion is the frequency chirp. In order to visualize this phenomenon we can calculate the instantaneous frequency, defined as: $\omega_i(t) \equiv \frac{d\phi}{dt}$, where ϕ is the phase of the pulse, which is the argument of the cosine in (2.70). Proceeding with the calculation we find:

$$\omega_i(t) = \frac{d}{dt}\left[\omega_0\left(t - \frac{z}{v_{ph}}\right) + \frac{z(t-\tau_g)^2}{2L_D\tau_p^2(z)}\right] = \omega_0 + \frac{z(t-\tau_g)}{L_D\tau_p^2(z)} \tag{2.72}$$

Depending on the sign of β_2, two types of dispersion are defined:

1. $\beta_2 > 0$: ordinary or normal dispersion,

2. $\beta_2 < 0$: anomalous dispersion.

We can assume for instance $\beta_2 > 0$ (hence $L_D > 0$) distinguishing two cases in (2.72):

1. $t < \tau_g \Rightarrow \omega_i(t) < \omega_0$
2. $t > \tau_g \Rightarrow \omega_i(t) > \omega_0$

Thus, as reported in figure 2.4, the red components of the pulse (that is, the part with the lower instantaneous frequency) arrive before the blue ones (the opposite outcome is expected in case of anomalous dispersion), this effect is called positive chirp (or negative chirp for anomalous dispersion).

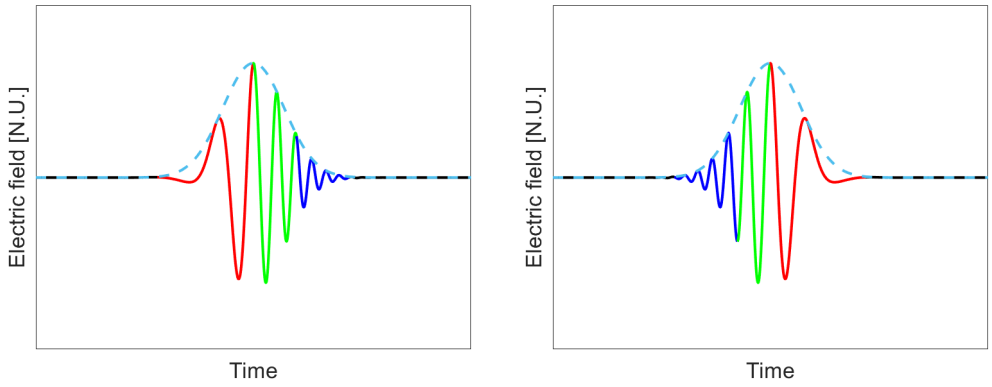

(a) Pulse with positive chirp. (b) Pulse with negative chirp

Figure 2.4: Representation of Gaussian pulses in time with positive (a) and negative (b) chirp respectively. It can be seen that different colours arrive at different times.

We can reach the same conclusion from another point of view: analyzing $\tau_g(\omega)$, that is the group delay depending on the frequency:

$$\tau_g(\omega) = z\frac{dk}{d\omega} = z\left[\frac{1}{v_g(\omega_0)} + \beta_2(\omega - \omega_0)\right] = \tau_g(\omega_0) + z\beta_2(\omega - \omega_0) \tag{2.73}$$

Also analyzing (2.73), we can observe that, for ordinary dispersion, $\tau_g(\omega) < \tau_g(\omega_0)$, if $\omega < \omega_0$, hence, the red components arrive before the blue ones (for the blue components $\tau_g(\omega) > \tau_g(\omega_0)$, since $\omega > \omega_0$).

2.1.6. Dispersion compensation

As we have seen in the previous sections, a pulse is modified while propagating in a medium. It is possible to describe the pulse before and after propagation in a medium in

the spectral domain with the following expression:

$$\tilde{E}_{OUT}(\omega, z) = \tilde{E}_{IN}(\omega, z = 0)e^{-ik(\omega)z}, \tag{2.74}$$

Where we can expand $k(\omega)$ in (2.74) as we did in (2.52), finding:

$$k(\omega)z = \omega_0\tau_{ph} + (\omega - \omega_0)\tau_g(\omega_0) + \frac{1}{2}D_2(\omega - \omega_0)^2 + \frac{1}{6}D_3(\omega - \omega_0)^2 + \dots, \tag{2.75}$$

Where in (2.75) we defined the Group Delay Dispersion (GDD) D_2 as: $D_2 \equiv z\beta_2$, while $D_3 \equiv z\beta_3$. During the propagation in a medium, the GDD increases leading to a growth in pulse duration. Since for many applications it is crucial to have short pulses, several techniques based on optical compressors have been developed to counteract dispersion. In particular, in order to compensate for the GDD introduced by a medium, an optical compressor should introduce an additional phase term ϕ_{comp} compensating for $\phi(\omega, z) = k(\omega)z$ such that $D_2^{comp} = -D_2$, and, to compensate for the third order dispersion, $D_3^{comp} = -D_3$. In figure 2.5 the conceptual scheme of an optical compressor is reported.

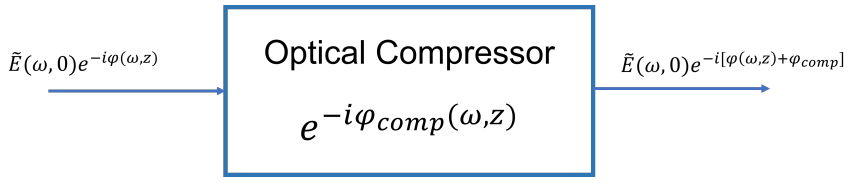

Figure 2.5: Conceptual scheme of an optical compressor.

There are several ways to build an optical compressor, such as diffraction gratings, spatial light modulators, chirped mirrors and prisms. The last method will be described in detail, since it will be exploited experimentally in section 3.1.

The most common configuration is depicted in figure 2.6, where two prisms are placed in anti-parallel configuration and are followed by a mirror.

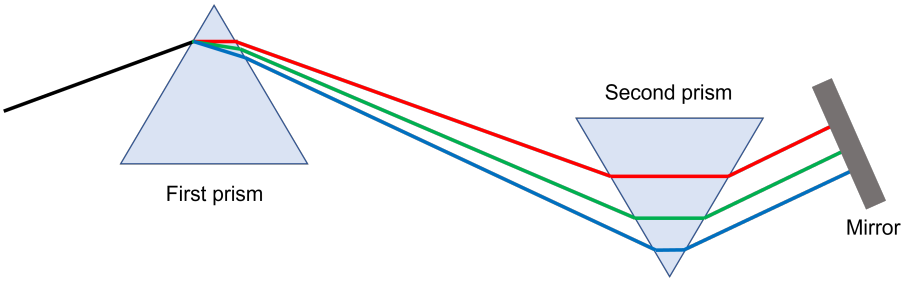

Figure 2.6: Scheme of a prism compressor.

The incoming beam impinges on the first prism at the Brewster angle, in order to minimize the reflection. Then, the different wavelengths are separated due to the dependence of the prism refractive index on the wavelength: $n_{prism}(\lambda)$. Different colours exit the first prism at different angles and then exit the second prism traveling again in parallel paths. During the propagation through the prism material the beam experiences normal dispersion. On the other hand, the angular dispersion between the prisms introduces anomalous dispersion. Increasing the distance between the two prisms, the anomalous dispersion can be greater than the positive dispersion introduced by the material, allowing to introduce a negative GDD [61]. It is also possible to tune the D_2^{prisms} introduced changing the insertion of one of the two prism without modifying the colours propagation.

Once the various colours are separated by the be prisms, they need to be recollimated in a single spot. This can be done placing a mirror after the second prism. The GDD is also doubled in this way.

The GDD introduced by the prism compressor at Brewster angle is [62]:

$$D_2^{prisms} = -\frac{\lambda_0^3}{\pi c^2}\left\{4L\cos\theta\left(\frac{dn}{d\lambda}\right)_{\lambda_0}^2 - 2L'\sin\theta\left[\left(\frac{d^2n}{d\lambda^2}\right)_{\lambda_0} + \left(2n_0 - \frac{1}{n_0^3}\right)\left(\frac{dn}{d\lambda}\right)_{\lambda_0}^2\right]\right\}, \tag{2.76}$$

Where L is the apex-to-apex distance between the prisms, while L' is the geometric path of the beam inside the prisms, $\theta(\lambda)$ is the angle between the various wavelength and the reference ray, which is the path followed by the central wavelength λ_0, n is the refractive index of the prism material.

Generally the angle θ is small, therefore the first term dominates, giving rise to $D_2^{prisms} < 0$. Also D_3^{comp} could be retrieved [62]:

$$D_3^{prisms} \simeq -\frac{2\lambda_0^4}{\pi^2 c^3}\left\{6L\cos\theta\left(\frac{dn}{d\lambda}\right)_{\lambda_0}^2 - \frac{1}{2}L'sin\theta\left[\left(\frac{d^2n}{d\lambda^2}\right)_{\lambda_0}\right]\right\}, \tag{2.77}$$

Also in this case the first term dominates giving a negative D_3^{prisms}.

2.2. Non-Linear optics

In the previous section we have considered linear optics. This picture is valid at low-moderate intensities. We could define an approximate threshold taking into account the peak intensity I_{peak} of the pulse, which is the intensity at the maximum of the envelope. Hence, for $I_{peak} \lesssim 10^{8\backsim 9}\frac{W}{cm^2}$, the matter responses in a linear way. However, if $10^{8\backsim 9}\frac{W}{cm^2} < I_{peak} < 10^{13}\frac{W}{cm^2}$, the matter response becomes non-linear and can be described through a perturbative approach [60]. In this case, the polarization has two main components (see eq. (2.18)): $\boldsymbol{P} = \boldsymbol{P}^{(L)} + \boldsymbol{P}^{(NL)}$, where $\boldsymbol{P}^{(L)}$ represents the linear polarization, described in the previous section, while $\boldsymbol{P}^{(NL)}$ is the non-linear one, and can be further developed as the sum of many components with different order of non-linearity:

$$\boldsymbol{P}^{(NL)} = \sum_{n=2}^{\infty} \boldsymbol{P}^{(n)} = \boldsymbol{P}^{(2)} + \boldsymbol{P}^{(3)} + \dots . \tag{2.78}$$

For higher intensities it is necessary to take into account the quantum nature of matter and solve the Shrödinger equation, finding the dipoles and calculating the polarization as the average of them, but this is out of the scope of this section.

2.2.1. Envelope propagation equation in Non-linear media

In section 2.1.1 we found, after some approximations, the propagation equation (2.17), which is valid for linear media. The goal of this section is to extend the propagation equation to non-linear media, and to consider the pulsed regime. To do this, the envelope only will be taken into account.

Starting from eq. (2.17), it is possible to take into account the non-linearity of media, simply writing the polarization as the sum of a linear and a non-linear part, obtaining:

$$\frac{\partial^2 E}{\partial z^2} - \frac{1}{c^2}\frac{\partial^2 E}{\partial t^2} = \mu_0 \frac{\partial^2 P^{(L)}}{\partial t^2} + \mu_0 \frac{\partial^2 P^{(NL)}}{\partial t^2}, \tag{2.79}$$

In order to proceed with the calculation, it is necessary to introduce the two-dimensional Fourier transform and its properties. It is defined as:

$$\hat{F}(k,\omega) = \mathcal{F}_2\left\{f(z,t)\right\} = \int_{-\infty}^{\infty}\int_{-\infty}^{\infty} f(z,t)e^{-i(\omega t - kz)}dtdz, \tag{2.80}$$

While the two-dimensional Fourier anti-transform is defined as:

$$f(z,t) = \mathcal{F}_2^{-1}\left\{\hat{F}(k,\omega)\right\} = \int_{-\infty}^{\infty}\int_{-\infty}^{\infty}\hat{F}(k,\omega)e^{i(\omega t-kz)}\frac{d\omega dk}{(2\pi)^2}, \tag{2.81}$$

The properties (2.27), (2.28) still hold. Furthermore, it can be demonstrated that:

$$\mathcal{F}_2\left\{\frac{d^n f(z,t)}{dz^n}\right\} = (-ik)^n\mathcal{F}_2\left\{f(z,t)\right\}, \tag{2.82}$$

We can now apply (2.80) to (2.79), exploiting properties (2.27), (2.28) and (2.82), obtaining:

$$-k^2\hat{E}(k,\omega) + \frac{\omega^2}{c^2}\hat{E}(k,\omega) = -\mu_0\omega^2\hat{P}^{(L)}(k,\omega) - \mu_0\omega^2\hat{P}^{(NL)}(k,\omega), \tag{2.83}$$

Where $\hat{E}(k,\omega) = \mathcal{F}_2\left\{E(z,t)\right\}$ and $\hat{P}^{(L),(NL)}(k,\omega) = \mathcal{F}_2\left\{P^{(L),(NL)}(z,t)\right\}$. Let us consider equations (2.32) and (2.34), where we implicitly wrote the Fourier transform of the linear polarization as[2]:

$$\hat{P}^{(L)}(k,\omega) = \epsilon_0\left[\epsilon_r(\omega) - 1\right]\hat{E}(k,\omega), \tag{2.84}$$

Therefore, considering (2.84), we can simplify (2.83) finding the propagation equation with bidimensional Fourier approach in non-linear media, namely:

$$\left(\frac{\omega^2\epsilon_r(\omega)}{c^2} - k^2\right)\hat{E}(k,\omega) = -\mu_0\omega^2\hat{P}^{(NL)}(k,\omega), \tag{2.85}$$

It should be pointed out that k is not the wavenumber of the propagating wave, but the spatial frequency, which is independent from the temporal one for propagation in non-linear media. Let us now consider the pulsed nature of the propagating waves, writing both the electric field and the non-linear polarization as the product of an envelope and a carrier:

$$E(z,t) = Re\left\{A(z,t)e^{i(\omega_0 t-k_0 z)}\right\}, \tag{2.86}$$

$$P^{(NL)}(z,t) = Re\left\{B(z,t)e^{i(\omega_0 t-k_p z)}\right\}, \tag{2.87}$$

[2]In this case, even if the expression is formally equivalent to the one found in (2.32), the bidimensional Fourier transform is considered, therefore the symbol $.\hat{.}.$ instead of $.\tilde{.}.$ is used.

Where the central wavenumber of the non-linear polarization k_p is different from k_0 in general. Let us now apply the Fourier bidimensional transform to (2.86) and (2.87):

$$\mathcal{F}_2\left\{E(z,t)\right\} = \hat{A}(k-k_0, \omega-\omega_0), \tag{2.88}$$

$$\mathcal{F}_2\left\{P^{(NL)}(z,t)\right\} = \hat{B}(k-k_p, \omega-\omega_0), \tag{2.89}$$

We can now proceed from (2.85) with the following calculations:

$$\left(\frac{\omega n(\omega)}{c} - k\right)\left(\frac{\omega n(\omega)}{c} + k\right)\hat{E}(k,\omega) = -\mu_0\omega^2\hat{P}^{(NL)}(k,\omega), \tag{2.90}$$

In equation (2.90), we can distinguish forward and backward propagation. It is possible to introduce a further approximation to get rid of the backward propagation term, namely the Slowly Varying Envelope function Approximation (SVEA). Since the envelope does not vary significantly over the period of the carrier, we can safely say that the frequencies and the wavenumbers of the pulse are centered in (ω_0, k_0) and do not deviate too much:

$$\left(\frac{\omega n(\omega)}{c} + k\right) \approx \left(\frac{\omega_0 n(\omega_0)}{c} + k_0\right) = 2k_0, \tag{2.91}$$

Therefore, taking (2.91) into account and applying the same reasoning to the right-hand term of (2.90) we find:

$$\left(\frac{\omega n(\omega)}{c} - k\right)\hat{E}(k,\omega) = -\frac{\mu_0\omega_0^2}{2k_0}\hat{P}^{(NL)}(k,\omega), \tag{2.92}$$

Then, defining $\tilde{k}(\omega) = \frac{\omega n(\omega)}{c}$ in (2.92), and considering $k_0 = \frac{\omega_0 n(\omega_0)}{c}$, we get:

$$\left(\tilde{k}(\omega) - k\right)\hat{E}(k,\omega) = -\frac{\mu_0\omega_0 c}{2n(\omega_0)}\hat{P}^{(NL)}(k,\omega), \tag{2.93}$$

Since the pulse is centered in k_0, we can expand $\tilde{k}(\omega)$ in (2.93) as:

$$\tilde{k}(\omega) = k_0 + \frac{(\omega-\omega_0)}{v_g(\omega_0)} + \sum_{n=2}^{N}\frac{\beta_n(\omega-\omega_0)^n}{n!}, \tag{2.94}$$

We can now substitute (2.88), (2.89) and (2.94) in (2.93), obtaining:

$$\left[\frac{(\omega-\omega_0)}{v_g(\omega_0)}+\sum_{n=2}^{N}\frac{\beta_n(\omega-\omega_0)^n}{n!}-(k-k_0)\right]\hat{A}(k-k_0,\omega-\omega_0)=-\frac{\mu_0\omega_0 c}{2n(\omega_0)}\hat{B}(k-k_p,\omega-\omega_0), \tag{2.95}$$

We can now apply the two-dimensional Fourier anti-transform (2.81) to both sides of (2.95) finding:

$$\begin{aligned}\int_{-\infty}^{+\infty}\int_{-\infty}^{+\infty}\left[\frac{(\omega-\omega_0)}{v_g(\omega_0)}+\sum_{n=2}^{N}\frac{\beta_n(\omega-\omega_0)^n}{n!}-(k-k_0)\right]\hat{A}(k-k_0,\omega-\omega_0)e^{i(\omega t-kz)}\frac{dkd\omega}{(2\pi)^2}=\\ =\int_{-\infty}^{+\infty}\int_{-\infty}^{+\infty}-\frac{\mu_0\omega_0 c}{2n(\omega_0)}\hat{B}(k-k_p,\omega-\omega_0)e^{i(\omega t-kz)}\frac{dkd\omega}{(2\pi)^2},\end{aligned} \tag{2.96}$$

Let us change the variables as follows: $\omega' \equiv \omega-\omega_0$, $k' \equiv k-k_0$ and $k'' \equiv k-k_p$. Equation (2.96) becomes:

$$\begin{aligned}\int_{-\infty}^{+\infty}\int_{-\infty}^{+\infty}\left[\frac{\omega'}{v_g(\omega_0)}+\sum_{n=2}^{N}\frac{\beta_n\omega'^n}{n!}-k'\right]\hat{A}(k',\omega')e^{i[\omega' t-(k'+k_0)z]}\frac{dk'd\omega'}{(2\pi)^2}=\\ =\int_{-\infty}^{+\infty}\int_{-\infty}^{+\infty}-\frac{\mu_0\omega_0 c}{2n(\omega_0)}\hat{B}(k'',\omega')e^{i[\omega' t-(k''+k_p)z]}\frac{dk''d\omega'}{(2\pi)^2},\end{aligned} \tag{2.97}$$

Let us now define $\Delta k \equiv k_p-k_0$, and multiply both sides of (2.97) for the imaginary unit i and rearrange the terms as follows:

$$\begin{aligned}\int_{-\infty}^{+\infty}\int_{-\infty}^{+\infty}\left[\frac{i\omega'}{v_g(\omega_0)}+\sum_{n=2}^{N}\frac{i(i)^{-n}\beta_n(i\omega')^n}{n!}-ik'\right]\hat{A}(k',\omega')e^{i[\omega' t-k'z]}\frac{dk'd\omega'}{(2\pi)^2}=\\ =\int_{-\infty}^{+\infty}\int_{-\infty}^{+\infty}-\frac{\mu_0\omega_0 c}{2n(\omega_0)}e^{-i\Delta kz}\hat{B}(k'',\omega')e^{i[\omega' t-k''z]}\frac{dk''d\omega'}{(2\pi)^2},\end{aligned} \tag{2.98}$$

Let us now apply the Fourier two-dimensional transform to (2.98), considering the properties (2.27), (2.28) and (2.82), and rearrange the terms:

$$\frac{\partial A}{\partial z} + \frac{1}{v_g(\omega_0)}\frac{\partial A}{\partial t} + \sum_{n=2}^{n}\frac{1}{n!}\beta_n(-i)^{n-1}\frac{\partial^n A}{\partial t^n} = -\frac{i\mu_0\omega_0 c}{2n(\omega_0)}e^{-i\Delta kz}B \tag{2.99}$$

Equation (2.99) represents the Envelope propagation equation for short laser pulses propagating in non-linear media [63], where the non-linearity is included in the term B, representing the envelope of the non-linear polarization.

2.2.2. Third order non-linear processes

Let us now focus on the third order non-linear optical processes[3]. Among these, Coherent Raman Scattering are of particular interest for the following sections and will be analyzed in further detail.

In order to describe these phenomena, the third order polarization should be taken into account:

$$\begin{aligned} P_i^{(3)}(t) = \epsilon_o \int_{-\infty}^{+\infty} dt' \int_{-\infty}^{+\infty} dt'' \int_{-\infty}^{+\infty} dt''' \chi_{ijkl}^{(3)}(t', t'', t''') \\ E_j(t-t')E_k(t-t'-t'')E_l(t-t'-t''-t''') \end{aligned} \tag{2.100}$$

Applying some approximations discussed in appendix A.1, we can simplify (2.100) as:

$$P^{(3)} = \epsilon_0 \chi^{(3)} E^3(t), \tag{2.101}$$

Where $\chi^{(3)}$ is the third order susceptibility of the propagation medium. Let us now introduce an incoming electric field defined as:

$$E(t) = A_1\cos(\omega_1 t + \phi_1) + A_2\cos(\omega_2 t + \phi_2) + A_3\cos(\omega_3 t + \phi_3), \tag{2.102}$$

The third order non-linear polarization could be calculated substituting (2.102) in (2.101), finding:

$$P^{(3)} = \epsilon_0 \chi^{(3)} \left[A_1\cos(\omega_1 t + \phi_1) + A_2\cos(\omega_2 t + \phi_2) + A_3\cos(\omega_3 t + \phi_3)\right]^3, \tag{2.103}$$

Performing the calculations, 22 different terms can be found oscillating at different frequencies. Oscillating, the polarization acts as a source giving rise to radiation at the same

[3] An analysis of the second order non-linear processes can be found in appendix A.1

frequency. The 22 terms can be classified in the following way:

- 3 terms at the original frequencies ω_1, ω_2 and ω_3, which give rise to the Optical Kerr effect,
- 3 terms at the third harmonics $3\omega_1$, $3\omega_2$ and $3\omega_3$, which is called Third Harmonic Generation (THG),
- 6 terms at $2\omega_i + \omega_j$, with $i \neq j$,
- 6 terms at $2\omega_i - \omega_j$, with $i \neq j$,
- 1 term at $\omega_1 + \omega_2 + \omega_3$,
- 3 terms at $\omega_i + \omega_j - \omega_k$, with $i \neq j \neq k$,

Therefore, a wave at a different frequency is obtained as an output. The whole process could be seen as an interaction among four wave. For this reason, third order phenomena are also called Four Wave Mixing (FWM) processes [63].

2.2.3. Propagation equation for Four Wave Mixing

In section 2.2.1 we ended up with the expression (2.99), which represents the envelope propagation equation in non-linear media. We would like to apply this equation to the FWM phenomena. Let us define the incoming electric field in the exponential form as:

$$\begin{aligned} E(t,z) = \frac{1}{2}\{A_1(t,z)e^{i(\omega_1 t - k_1 z)} + A_2(t,z)e^{i(\omega_2 t - k_2 z)} + \\ + A_3(t,z)e^{i(\omega_3 t - k_3 z)} + A_4(t,z)e^{i(\omega_4 t - k_4 z)} + c.c.\} \end{aligned} \tag{2.104}$$

Where the expression *c.c.* stands for complex conjugate.

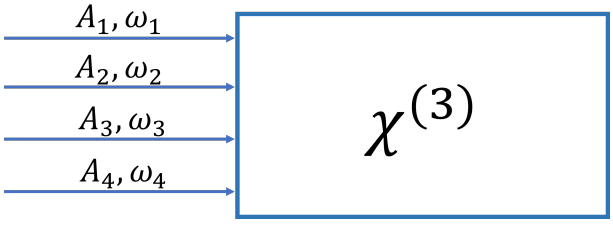

Figure 2.7: Conceptual scheme of the interaction between light and matter considering third order non-linear processes in the FWM frame.

Let us now assume $\omega_1 + \omega_3 = \omega_2 + \omega_4$, and let us focus on the terms oscillating at the same frequencies as the incoming waves. Substituting (2.104) in (2.99) we find, after some

calculations, that the third order polarization term oscillating at frequency ω_1, namely $P^{(3)}_{\omega_1}$ reads:

$$P^{(3)}_{\omega_1}(t,z) = \frac{\epsilon_0\chi^{(3)}}{4} 3A_2(t,z)A_4(t,z)A_3^*(t,z)e^{i[(\omega_2-\omega_3+\omega_4)t-(k_2+k_4-k_3)z} + c.c., \tag{2.105}$$

The same reasoning could be applied to all the other terms oscillating at the original frequencies, obtaining:

$$\begin{cases} P^{(3)}_{\omega_1}(t,z) = \dfrac{3\epsilon_0\chi^{(3)}}{4} A_2(t,z)A_4(t,z)A_3^*(t,z)e^{i[\omega_1 t-(k_2+k_4-k_3)z} + c.c. & \text{(2.106a)} \\ P^{(3)}_{\omega_2}(t,z) = \dfrac{3\epsilon_0\chi^{(3)}}{4} A_1(t,z)A_3(t,z)A_4^*(t,z)e^{i[\omega_2 t-(k_1+k_3-k_4)z} + c.c. & \text{(2.106b)} \\ P^{(3)}_{\omega_3}(t,z) = \dfrac{3\epsilon_0\chi^{(3)}}{4} A_2(t,z)A_4(t,z)A_1^*(t,z)e^{i[\omega_3 t-(k_2+k_4-k_1)z} + c.c. & \text{(2.106c)} \\ P^{(3)}_{\omega_4}(t,z) = \dfrac{3\epsilon_0\chi^{(3)}}{4} A_1(t,z)A_3(t,z)A_2^*(t,z)e^{i[\omega_4 t-(k_1+k_3-k_2)z} + c.c., & \text{(2.106d)} \end{cases}$$

From (2.105), we found that the envelope of $P^{(3)}_{\omega_1}$ can be written as:

$$B(t,z) = \frac{3\epsilon_0\chi^{(3)}}{4} A_2(t,z)A_4(t,z)A_3^*(t,z), \tag{2.107}$$

We can now plug (2.107) in (2.99) and develop the calculation for the wave at frequency ω_1. Therefore, the propagation equation becomes:

$$\frac{\partial A_1}{\partial z} + \frac{1}{v_g(\omega_1)}\frac{\partial A_1}{\partial t} + \sum_{n=2}^{n}\frac{1}{n!}\beta_n(-i)^{n-1}\frac{\partial^n A_1}{\partial t^n} = -\frac{i\mu_0\omega_1 c}{2n(\omega_1)}\frac{3\epsilon_0\chi^{(3)}}{4}A_2A_4A_3^*e^{-i(k_2+k_4-k_3-k_1)z}, \tag{2.108}$$

Let us define $k_p \equiv k_2 + k_4 - k_3$, and $\Delta k = k_1 - k_p$. We can proceed rewriting (2.108) as:

$$\frac{\partial A_1}{\partial z} + \frac{1}{v_g(\omega_1)}\frac{\partial A_1}{\partial t} + \sum_{n=2}^{n}\frac{1}{n!}\beta_n(-i)^{n-1}\frac{\partial^n A_1}{\partial t^n} = -\frac{i3\omega_1\chi^{(3)}}{8cn(\omega_1)}A_2A_4A_3^*e^{i\Delta kz}, \tag{2.109}$$

Where we exploited the relation $\epsilon_0\mu_0 = \frac{1}{c^2}$. Let us neglect the dispersion term for simplicity and extend the same reasoning to the other frequencies. Plugging the envelope of the polarization written in (2.106) and proceeding with analogous calculation we find:

$$\begin{cases} \dfrac{\partial A_1}{\partial z} + \dfrac{1}{v_g(\omega_1)}\dfrac{\partial A_1}{\partial t} = -if_1 A_2 A_4 A_3^* e^{i\Delta kz} & \text{(2.110a)} \\ \dfrac{\partial A_2}{\partial z} + \dfrac{1}{v_g(\omega_2)}\dfrac{\partial A_2}{\partial t} = -if_2 A_1 A_3 A_4^* e^{-i\Delta kz} & \text{(2.110b)} \\ \dfrac{\partial A_3}{\partial z} + \dfrac{1}{v_g(\omega_3)}\dfrac{\partial A_3}{\partial t} = -if_3 A_2 A_4 A_1^* e^{i\Delta kz} & \text{(2.110c)} \\ \dfrac{\partial A_4}{\partial z} + \dfrac{1}{v_g(\omega_4)}\dfrac{\partial A_4}{\partial t} = -if_4 A_1 A_3 A_2^* e^{-i\Delta kz}, & \text{(2.110d)} \end{cases}$$

Where we made use of f_i, defined as $f_i \equiv \frac{3\omega_i \chi^{(3)}}{8cn(\omega_i)}$. It is possible to observe that the set of equations (2.110) represents the propagation equation for four wave mixing phenomena (neglecting dispersion for simplicity), which are characterized by the direct dependence on the term $\chi^{(3)}$, which will be analyzed in detail in the following.

2.3. Coherent Raman Scattering Processes

In this section, coherent Raman scattering processes will be analyzed in detail, dwelling on CARS.

2.3.1. Molecular resonances

The simplest way to describe a molecule interacting with an electromagnetic field is to model the system as a mass attached to a spring characterized by stiffness k, as depicted in fig. 2.8. Through this picture it is possible to give an intuitive explanation of Raman scattering [64].

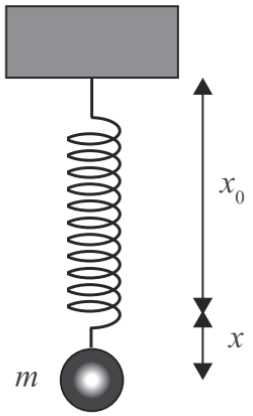

Figure 2.8: Mass-spring system. x_0 is the equilibrium position, while x is the relative displacement. Adapted from [64].

The system described above gives rise to a harmonic oscillator, which is an ideal object whose temporal oscillation is a sine wave with constant amplitude and with a frequency that is solely dependent on the system parameters. Let us consider a mass attached to a spring and set vertically, subjected to gravity and let us write the equation describing its center of mass:

$$mg - kx_0 = 0, \tag{2.111}$$

In which, x_0 represents the equilibrium position. It is possible to study the displacement x of the center of mass with respect to x_0. Exploiting the principle of energy conservation, the following expression is found:

$$\frac{d^2x}{dt^2} + \omega_0^2 x = 0, \tag{2.112}$$

In which $\omega_0 = \frac{k}{m}$ is the resonant frequency. Let us introduce a damping force experienced by the mass, directly proportional to its velocity and to a damping coefficient γ. We can modify equation (2.112) adding this term finding:

$$\frac{d^2x}{dt^2} + 2\gamma\frac{dx}{dt} + \omega_0^2 x = 0, \tag{2.113}$$

Since we would like to model the interaction with the electromagnetic field, we need to introduce a driving force oscillating periodically. Hence we define $F(t) = F_0 \cos(\omega t)$, where F_0 represents the amplitude, while ω is the angular frequency. Introducing the

driving force $F(t)$, equation (2.113) becomes:

$$\frac{d^2x}{dt^2} + 2\gamma\frac{dx}{dt} + \omega_0^2 x = \frac{F(t)}{m}, \tag{2.114}$$

Let us move to the complex exponential notation, where $F(t) = F_0 e^{-i\omega t}$ and $x(\omega, t) = x(\omega)e^{-i\omega t}$, which allows us to perform the temporal derivatives. Therefore, plugging these expressions in (2.114) we find:

$$(-\omega^2 - 2i\gamma\omega + \omega_0^2)x(\omega)e^{-i\omega t} = \frac{F_0 e^{-i\omega t}}{m}, \tag{2.115}$$

Analyzing (2.115), we can find the solution $x(\omega)$:

$$x(\omega) = \frac{F_0/m}{\omega_0^2 - \omega^2 - 2i\gamma\omega}, \tag{2.116}$$

Getting close to resonance ($\omega \approx \omega_0$) and for small damping coefficient ($\gamma \ll \omega_0$), (2.116) can be approximated as a complex Lorentzian function [64]:

$$x(\omega) = \frac{-F_0/(2m\omega_0)}{(\omega - \omega_0) + i\gamma}, \tag{2.117}$$

2.3.2. Vibrational modes

In the previous section we modeled a molecule as a single mass attached to a spring. This led to equation (2.116), which describes the movement of the mass varying the frequency of the driving force. Let us now generalize the model in order to describe the vibrational modes of a molecule. A vibrational mode is a periodic motion of the atoms of a molecule relative to each other, such that the center of mass remains still, an example is reported in fig. 2.9. Every mode is characterized by a certain resonance frequency Ω_R

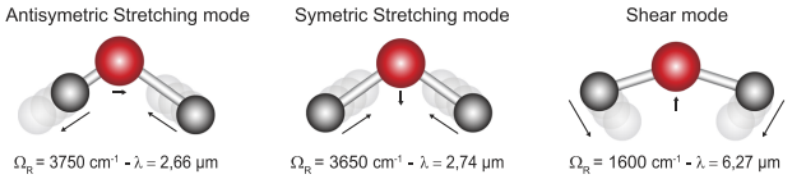

Figure 2.9: Water vibrational modes. Adapted from [64].

A molecule constituted of n atoms with a non-linear geometry presents $3n-6$ vibrational

modes. If the molecule is linear, then the number of vibrational modes is $3n-5$, therefore, a diatomic molecule has just one vibrational mode, the stretching one. Let us now model a diatomic molecule as a system constituted by two point masses, respectively m_1 and m_2, connected by a spring. We will assume that the equilibrium distance between the point masses is x_0 and the resonant frequency is Ω_R. We will also assume that the diatomic molecule taken into account is polar and presents an asymmetric distribution of charges, in particular the atom m_1 will have a charge $+q$, while the atom m_2 will have a charge $-q$. The model is shown in fig. 2.10.

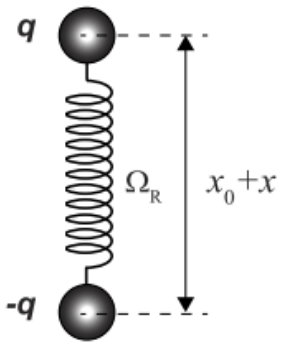

Figure 2.10: Model of a diatomic molecule: two charged masses attached to a spring. Adapted from [64].

Let us consider the interaction with an electric field $E(t)$, characterized by an angular frequency ω. The field will generate a Lorentz force $F_{Lorentz} = qE_0e^{-i\omega t}$ acting on the atoms of the molecule. We can write a formula analogous to (2.114):

$$\frac{d^2x}{dt^2} + 2\gamma\frac{dx}{dt} + \Omega_R^2 x = \frac{F_{Lorentz}(t)}{\mu}, \tag{2.118}$$

In which μ is the reduced mass: $\mu = m_1m_2/(m_1+m_2)$, and where the damping term γ represents the radiation loss of the oscillating dipole. Equation (2.118) can be solved (as we solved (2.114)), finding the approximated solution:

$$x(\omega) = \frac{-F_{Lorentz}/(2\mu\Omega_R)}{(\omega-\Omega_R)+i\gamma}, \tag{2.119}$$

The presence of an asymmetric distribution of charges in the molecule induces a dipole moment $\boldsymbol{p}$, which can be expressed as $\boldsymbol{p} = q\boldsymbol{d}$, where $\boldsymbol{d}$ is the vector displacement between the atoms, directed from the negative to the positive charge. If we consider a macroscopic medium, constituted by an ensemble of N diatomic molecules modelled as above, all

subjected to the same electric field $E(t)$, the charge displacement of every molecule will contribute to the total polarization of the medium, which can be calculated as the sum of all the single dipole moments:

$$P(\omega) = Nqx(\omega), \tag{2.120}$$

Let us now define the linear electronic susceptibility as:

$$P(\omega) = \epsilon_0 \chi^{(1)}(\omega) E(\omega), \tag{2.121}$$

Comparing formulas (2.120) and (2.121), and plugging in (2.119), we find the expression of the linear susceptibility $\chi^{(1)}(\omega)$:

$$\chi^{(1)}(\omega) = \frac{-\frac{Nq^2}{(2\epsilon_0 \mu \Omega_R)}}{(\omega - \Omega_R) + i\gamma}, \tag{2.122}$$

Expression (2.122) describes the vibrational contribution from the molecule to the susceptibility of the medium. The real part is related to the medium dispersion and it has an antisymmetric shape with respect to the resonance frequency, while the imaginary part is related to the medium absorption and it is characterized by a Lorentzian shape, centered in Ω_R. The width of the Lorentzian peak of $Im\left(\chi^{(1)}\right)$ is directly proportional to the damping constant γ. The real and imaginary parts are schematically depicted in fig. 2.11.

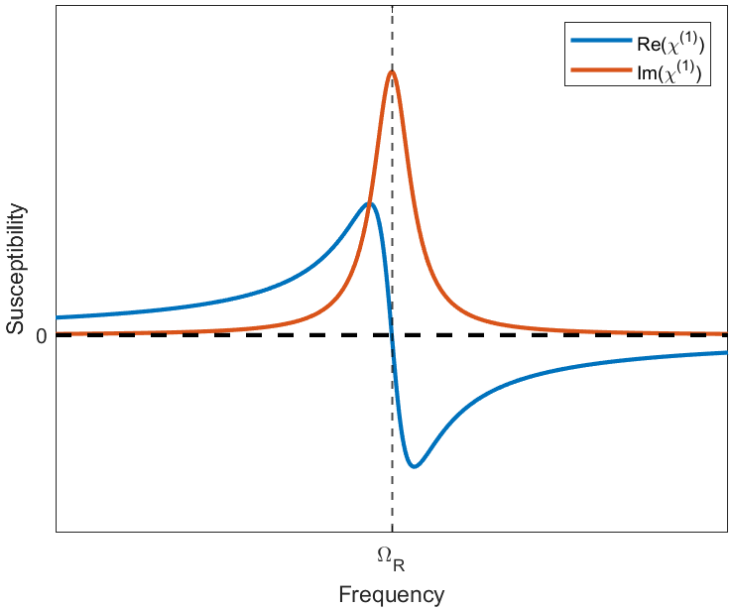

Figure 2.11: Graph of the the real and imaginary parts of the linear susceptibility.

For diluted media, the refractive index can be calculated from $Re\left(\chi^{(1)}\right)$ as:

$$n(\omega) = n_0 - \frac{Re\left[\chi^{(1)}(\omega)\right]}{2n_0}, \tag{2.123}$$

In which n_0 is the mean refractive index of the medium. On the other hand, the absorption coefficient $\alpha(\omega)$, can be calculated from $Im\left(\chi^{(1)}\right)$ as:

$$\alpha(\omega) = \frac{2\pi}{\lambda_0 n_0} Im\left[\chi^{(1)}(\omega)\right], \tag{2.124}$$

Where $\alpha(\omega)$ is expressed in cm^{-1} and can be found in the Lambert-Beer law, describing the reduction of light intensity in a medium due to absorption of light, as:

$$I(L) = I_0 \exp(-\alpha L), \tag{2.125}$$

It is possible to exploit this feature of media in order to measure the resonance frequencies of the vibrational modes, performing a spectroscopy of the analyzed medium. This technique is called IR absorption spectroscopy and allows one to identify and quantify absorption bands corresponding to different molecular species in a sample.

2.3.3. Spontaneous Raman Scattering

The main phenomena arising from light-matter interaction are absorption and scattering. In the first case, the light energy is retained by the molecule for a certain amount of time, while in the second case the light is instantaneously scattered in a different direction. The vast majority of the scattered photons preserve the original frequency, thus this process is called elastic (or Rayleigh) scattering, since the energy of the light photon is preserved. Nevertheless, a small portion of the photons is inelastically scattered, and change the energy, propagating at a difference frequency with respect to the original one. This phenomenon is called Raman scattering. In order to understand the Raman effect, let us consider again the diatomic molecule described in the previous section. Before we assumed that the molecule was polar, that is it presented an asymmetric charge distribution on the two atoms. In this part we will drop this assumption. However, even though a molecule is not polar, it will have a polarizability α depending on the intramolecular distance x. Let us assume the molecule is vibrating at the resonance frequency Ω_R. The fluctuations of the interatomic distance with respect to the equilibrium position can be described as: $x(t) = x_f \cos(\Omega_R t)$, where x_f is the amplitude fluctuations. Assuming the displacement

amplitude is small, we can perform a Taylor expansion of the polarizability with respect to the equilibrium position:

$$\alpha(t) = \alpha_0 + \left(\frac{\partial \alpha}{\partial x}\right)_0 x(t), \tag{2.126}$$

The dipole moment induced by an electric field oscillating at ω_p, $E(t) = E_0 cos(\omega_p t)$, can be calculated as:

$$p = \epsilon_0 \alpha(t) E(t), \tag{2.127}$$

Let us now plug the expression of the polarizability (2.126) in (2.127):

$$p = \epsilon_0 \left[\alpha_0 + \left(\frac{\partial \alpha}{\partial x}\right)_0 x_f \cos(\Omega_R t)\right] E_0 \cos(\omega_p t), \tag{2.128}$$

We can proceed with the calculations from (2.128) finding:

$$p = \epsilon_0 \alpha_0 E_0 cos(\omega_p t) + \frac{\epsilon_0 \left(\frac{\partial \alpha}{\partial x}\right)_0 E_0 x_f}{2} cos[(\omega_p - \Omega_R)t] + \frac{\epsilon_0 \left(\frac{\partial \alpha}{\partial x}\right)_0 E_0 x_f}{2} cos[(\omega_p + \Omega_R)t], \tag{2.129}$$

Let us analyze eq. (2.129). The first term, oscillating at the same frequency of the incoming field corresponds to the Rayleigh scattering. In this case the photons are simply scattered by the molecule without any exchange of energy. The second term is oscillating at angular frequency $\omega_S = \omega_p - \Omega_R$ and describes a red-shifted scattering known as Raman Stokes scattering. In this case the molecule absorbs part of the energy of the light and is promoted from ground state to a vibrationally excited state. Consequently, the outgoing photons present a lower energy with respect to the incoming one. The third term represents the Raman anti-Stokes scattering and oscillates at $\omega_{AS} = \omega_p + \Omega_R$. In this case the molecule goes from the excited state to the ground one, releasing energy. The outgoing photons have a higher energy with respect to the incoming ones, therefore they are blue-shifted in frequency. The different types of scattering are schematically depicted in fig. 2.12 making use of Jablonsky diagrams.

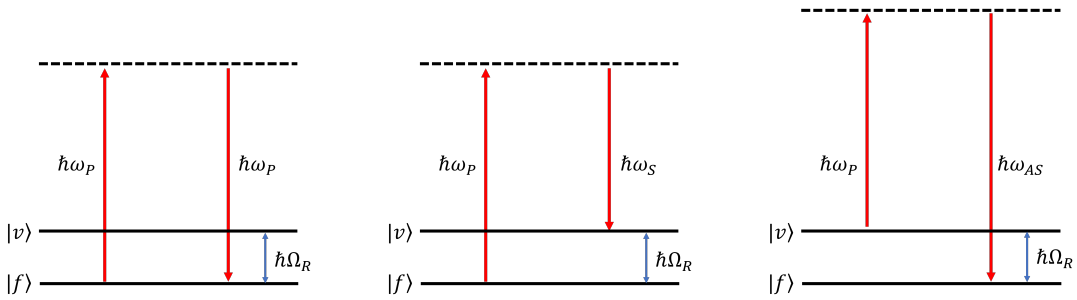

(a) Rayleigh scattering. (b) Stokes Raman scattering. (c) Anti-Stokes Raman scattering.

Figure 2.12: Jablonsky diagrams of (a) Rayleigh scattering, (b) Stokes Raman scattering, (c) anti-Stokes Raman scattering. The solid lines represent the fundamental state $|f\rangle$ and the vibrational state $|v\rangle$, while the dashed one is a virtual state. $|f\rangle$ and $|v\rangle$ are separated by the resonance frequency Ω_R.

At thermal equilibrium, atomic level populations are described by the Boltzmann distribution (2.130), which gives the probability that a system will be in the i-th state depending on the energy of the level ϵ_i and on the temperature:

$$p_i \propto e^{-\epsilon_i/kT}, \tag{2.130}$$

Therefore, the population of the excited level is lower than the one at ground state, and they become equal at infinite temperature. Thus, since to observe anti-Stokes scattering we need the molecule to be in the excited state, we expect a lower signal with respect to the Stokes scattering, unless the temperature is really high. This has been proved experimentally. In order to be Raman active, a vibrational mode has to affect the polarizability, therefore, the selection rule can be expressed as: $\left(\frac{\partial\alpha}{\partial x}\right)_0 \neq 0$. Similarly to IR absorption spectroscopy, Raman spectroscopy enables to identify the vibrational levels and measure their energy analyzing the spectral distance of the Raman peaks with respect to the Rayleigh scattering peak, as shown in fig. 2.13.

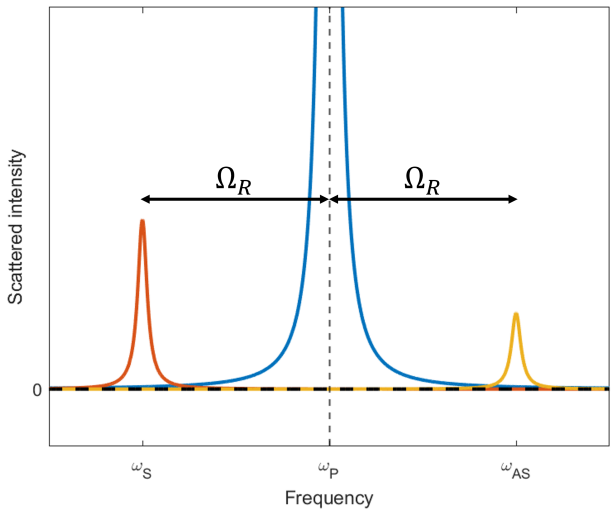

Figure 2.13: Scattered light from a molecule with a single vibrational mode at frequency Ω_R. From the left, the Stokes, Rayleigh and anti-Stokes scattering can be seen.

If a molecule presents inversion symmetry, its modes can be either Raman active and not IR active or vice-versa. In particular, symmetric modes with respect to the inversion symmetry are only Raman active, while anti-symmetric ones are only IR active. The main advantage of Raman spectroscopy with respect to IR absorption spectroscopy is that the former allows to reach sub-micron resolution, since shorter wavelengths can be used to excite Raman scattering. However, the cross section of Raman scattering is rather poor: the order of magnitude is around 10^{-30} cm^2 (while the cross section of single photon absorption fluorescence can reach 10^{-16} cm^2).

2.3.4. Vibrational spectrum

In the previous section we considered a simple diatomic molecule, characterized by a single vibrational mode. However, real molecules are often constituted of more than two atoms and present several modes of vibration. Therefore, the Raman scattering gives rise to a spectrum characterized by many peaks, which allows one to distinguish different molecules. The study of the Raman scattering spectrum is called Raman spectroscopy. In order to perform it, the sample is illuminated by a laser beam, also called 'pump' at a certain frequency ω_P. Then, the outcoming radiation is measured through a spectrometer, filtering the Rayleigh scattered light and taking into account only the inelastically scattered one. Since the Stokes and anti-Stokes spectra carry the same spectral information, the former is generally preferred due to the higher intensity. Raman spectroscopy is a powerful technique, which is becoming increasingly popular among biologists [26]. A Raman spectrum can be regarded as a phenotype of a biological system because it pro-

vides an overall molecular vibrational profile, containing Raman bands for major cellular building blocks, such as proteins, nucleic acids, lipids, and carbohydrates [65]. This allows to distinguish different parts of a biological sample without using any stain or marker. A biological Raman spectrum can be divided into three main regions: the 'fingerprint' region that contains essential bio-information and can be seen as a fingerprint of a cell (400 - 1800 cm^{-1}); the 'silent' region that usually does not involve vibrational modes contributed by biomolecules formed of naturally occurring isotopes and can involve bands contributed by stable isotopes or triple bonds (1800-2700 cm^{-1}); the high-wavenumber region that is specifically contributed by the stretching vibrations of CH groups, predominantly from lipids and proteins (2700-3200 cm^{-1}). The main benefits of employing Raman micro-spectroscopy in biological studies are high spatial resolution, the ability to identify aqueous materials, intrinsic and label-free characterisation, non-contacting and non-destructive analysis, quick preparation, and small sample volume.

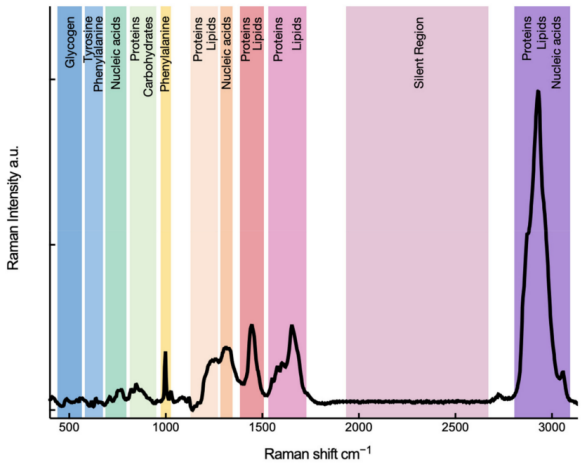

Figure 2.14: Raman spectrum of a human cell, demonstrating various bands representative of cellular constituents. Graph taken from [65].

As it can be seen in fig. 2.14, the Raman intensity depends on the Raman shift. It can be calculated as:

$$\text{Raman shift} = \frac{\Omega_R}{2\pi c} = \frac{(\omega_P - \omega_S)}{2\pi c} = \lambda_P^{-1} - \lambda_S^{-1}, \tag{2.131}$$

Where λ_P and λ_S are respectively the pump and Stokes wavelengths.

2.3.5. Coherent Raman Scattering

In the previous section we highlighted that the main limitation of Raman spectroscopy is the rather low cross-section. Therefore, in order to obtain a vibrational spectrum, a considerable amount of time is needed to reach an acceptable signal to noise ratio. Coherent Raman scattering (CRS) allows to solve this problem gaining a factor of 10^7 in efficiency as compared to spontaneous Raman scattering. Let us consider an incoming electric field, constituted by two waves, denominated pump and Stokes, respectively with frequency ω_P and ω_S:

$$E(z,t) = A_P e^{i(\omega_P t - k_p z)} + A_S e^{i(\omega_S t - k_s z)} + c.c., \tag{2.132}$$

The interference between the two fields generates a beating with frequency $\Omega = \omega_P - \omega_S$. If the beating frequency Ω matches the frequency of a vibrational mode, $\Omega_R = \Omega$, then the normal mode enters in resonance with the wave beating.

Let us consider again the diatomic molecule modelled as a harmonic oscillator, described by the expression (2.114). Let us find the expression of the force $F(t)$ evaluating the derivative of the energy W necessary to create a dipolar moment $\boldsymbol{p}(t) = \epsilon_0 \alpha(t) \boldsymbol{E}(t)$. The energy of a dipole in an electric field is:

$$W = \frac{1}{2} \langle \boldsymbol{p}(z,t) \cdot \boldsymbol{E}(t) \rangle = \frac{1}{2} \epsilon_0 \alpha(t) \left\langle E^2(z,t) \right\rangle, \tag{2.133}$$

Where the intensity term $\langle E^2(z,t) \rangle$ is calculated considering as:

$$\left\langle E^2(z,t) \right\rangle = A_P A_S^* e^{i(\Omega t - Kz)} + c.c., \tag{2.134}$$

Where we considered the electric field in (2.132). The brackets $\langle \dots \rangle$ represent the time average over one optical period. We can now plug (2.134) in (2.133) and perform the derivative with respect to the intermolecular distance obtaining:

$$F(t) = \frac{dW}{dx} = \epsilon_0 \left(\frac{\partial \alpha}{\partial x} \right)_0 \left[A_P A_S^* e^{i(\Omega t - Kz)} + c.c. \right], \tag{2.135}$$

Let us plug (2.135) in the expression of the driven harmonic oscillator (2.114), and look for a solution of the form:

$$x(z,t) = x(\Omega) e^{i(\Omega t - Kz)} + c.c., \tag{2.136}$$

Near the resonance, the molecular vibration amplitude is:

$$x(\Omega) = \frac{-\left(\frac{\epsilon_0}{2\mu\Omega_R}\right)\left(\frac{\partial\alpha}{\partial x}\right)_0 A_P A_S^*}{(\Omega - \Omega_R) + i\gamma}, \tag{2.137}$$

Therefore, if the beating frequency Ω gets close to the resonance frequency Ω_R, the vibration amplitude of the molecule $x(\Omega)$ grows inducing non-linear effects.

Let us now calculate the induced polarization as the sum of the induced dipole moments in the medium:

$$P(z,t) = Np(z,t) = N\epsilon_0 \left[\alpha_0 + \left(\frac{\partial\alpha}{\partial x}\right)_0 x(z,t)\right] E(z,t), \tag{2.138}$$

We can now distinguish two terms from (2.138):

1. the linear polarization $P^{(L)}$, directly proportional to the electric field and oscillating at the same frequency: $P^{(L)} = N\epsilon_0\alpha_0 E(z,t)$
2. The non-linear polarization $P^{(NL)}$:

$$P^{(NL)} = N\epsilon_0 \left(\frac{\partial\alpha}{\partial x}\right)_0 \left[x(\Omega)e^{i(\Omega t - Kz)} + c.c.\right]\left[A_P e^{i(\omega_P t - k_P z)} + A_S e^{i(\omega_S t - k_S z)} + c.c.\right], \tag{2.139}$$

We can now perform the calculations developing (2.139) finding four terms radiating at different frequencies. In particular we find:

1. A term oscillating at frequency $\omega_{AS} = 2\omega_P - \omega_S$:

$$P(\omega_{AS}) = N\epsilon_0 \left(\frac{\partial\alpha}{\partial x}\right)_0 x(\Omega) A_P e^{-i(2k_P - k_S)z}, \tag{2.140}$$

2. A term oscillating at frequency $\omega_{CS} = 2\omega_S - \omega_P$:

$$P(\omega_{CS}) = N\epsilon_0 \left(\frac{\partial\alpha}{\partial x}\right)_0 x^*(\Omega) A_S e^{-i(2k_S - k_P)z}, \tag{2.141}$$

3. A term oscillating at frequency ω_P:

$$P(\omega_P) = N\epsilon_0 \left(\frac{\partial\alpha}{\partial x}\right)_0 x(\Omega) A_S e^{-ik_P z}, \tag{2.142}$$

4. A term oscillating at frequency ω_S:

$$P(\omega_S) = N\epsilon_0 \left(\frac{\partial \alpha}{\partial x}\right)_0 x^*(\Omega) A_P e^{-ik_S z}, \tag{2.143}$$

The polarization oscillating at different frequencies act as the source of different processes. $P(\omega_{AS})$ gives rise to the Coherent anti-Stokes Raman scattering (CARS), $P(\omega_{CS})$ to the Coherent Stokes Raman scattering (CSRS), while $P(\omega_P)$ and $P(\omega_S)$ are the source of Stimulated Raman scattering.

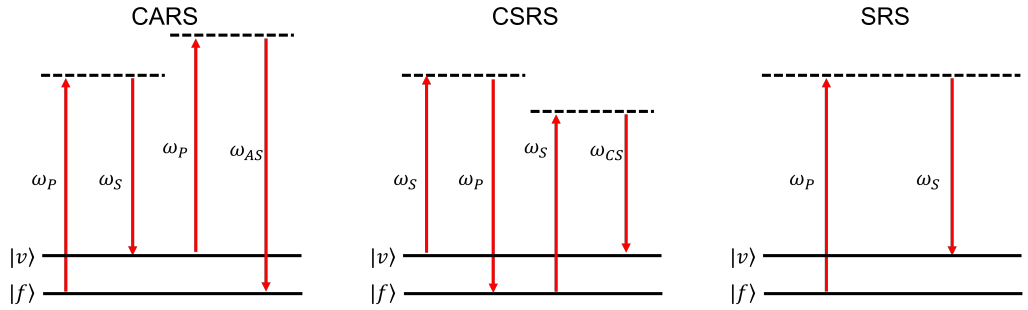

(a) Coherent anti-Stokes Raman scattering.

(b) Coherent Stokes Raman scattering.

(c) Stimulated Raman scattering.

Figure 2.15: Jablonsky diagrams of (a) Coherent anti-Stokes Raman scattering (CARS), (b) Coherent Stokes Raman scattering (CSRS), (c) Stimulated Raman scattering.

CRS processes arise from the third order non-linear polarization[4], and can be seen as four-wave mixing phenomena.

2.3.6. The CARS process

Among the coherent Raman scattering processes, the Coherent Anti-Stokes Raman scattering (CARS) will be described in detail. It can be generated exploiting two pulses centered at different frequencies, namely the pump pulse at frequency ω_P and the Stokes pulse at frequency ω_S. The intensity must be high enough to stimulate third order non-linear processes, as described in section 2.2.2. Therefore, the third order non-linear polarization oscillating at frequency ω_{AS} can be written as[5]:

[4] A second order dependence on the electric fields can be seen in the expression of $x(\Omega)$, reported in (2.137), while the third is explicitly expressed in (2.140), (2.141), (2.142), (2.143).

[5] Equation (2.144) is a generalized form of eq. (2.106), where the tensorial nature of the third order susceptibility is taken into account.

$$P_i(\boldsymbol{r}, \omega_{AS}) = \frac{3\epsilon_0}{4} \sum_{j,k,l} \chi^{(3)}_{ijkl} E_{P_j}(\boldsymbol{r}) E_{P_k}(\boldsymbol{r}) E^*_{S_l}(\boldsymbol{r}) \tag{2.144}$$

In which $i, j, k, l = \{x, y, z\}$. The Raman scattered light can be depolarized with respect to the incident one. To take into account this process, let us define the Raman depolarization ratio ρ_R as:

$$\rho_R = \frac{I_R(\perp)}{I_R(\parallel)}, \tag{2.145}$$

Where $I_R(\parallel)$ is the Raman intensity polarized as the pump, while $I_R(\perp)$ is perpendicular to it. The depolarization ratio is a number between 0 and $\frac{3}{4}$, depending on the vibrational mode stimulated. If we consider isotropic media, without any one-photon transition at ω_P or ω_S, it can be proved [64] that $\boldsymbol{P}(\boldsymbol{r})$ can be expressed in terms of the tensor element $\chi^{(3)}_{xxyy}$ and the Raman depolarization ratio as:

$$\begin{aligned} \boldsymbol{P}(\boldsymbol{r}, \rho_R; \omega_{AS}) = \frac{3\epsilon_0}{2} \chi^{(3)}_{xxyy} \Big\{ & \left[\boldsymbol{E_P}(\boldsymbol{r}) \cdot \boldsymbol{E^*_S}(\boldsymbol{r})\right] \boldsymbol{E_P}(\boldsymbol{r}) + \\ & \frac{\rho_R}{1-\rho_R} \left[E^2_{P_x}(\boldsymbol{r}) + E^2_{P_y}(\boldsymbol{r}) + E^2_{P_z}(\boldsymbol{r})\right] \boldsymbol{E^*_S}(\boldsymbol{r}) \Big\}, \end{aligned} \tag{2.146}$$

Several considerations could be pointed out:

- if the pump and Stokes beams are linearly polarized in the same direction, the non-linear polarization is collinear with them,
- on the other hand, if the pump and Stokes fields are linearly polarized in mutually perpendicular directions (thus, $\boldsymbol{E_P}(\boldsymbol{r}) \cdot \boldsymbol{E^*_S}(\boldsymbol{r}) = 0$), the induced polarization is aligned with the Stokes beam and the totally polarized Raman bands, characterized by $\rho_R = 0$, can not be stimulated,
- If $\rho_R = 0$, the polarization is collinear with the pump field, and maximized for $\boldsymbol{E_P}(\boldsymbol{r}) \parallel \boldsymbol{E^*_S}(\boldsymbol{r})$,

For simplicity, in the following we will assume that $\rho_R = 0$ and that the pump and Stokes fields are linearly polarized in the same direction.

Therefore, the polarization oscillating at the anti-stokes frequency is described by the expression (2.106d) assuming the following condition:

$$\omega_1 = \omega_3 = \omega_P, \quad \omega_2 = \omega_S, \quad \omega_4 = 2\omega_P - \omega_S = \omega_{AS}, \tag{2.147}$$

Thus, the induced non-linear polarization giving rise to the CARS signal reads as:

$$P_{\omega_{AS}} = \frac{3\epsilon_0 \chi^{(3)}(\omega_{AS})}{4} A_P^2 A_S^* e^{i[\omega_{AS}t-(2k_P-k_S)z]} + c.c., \tag{2.148}$$

Where we discarded the vectorial nature since we will consider collinear geometry in the following. We can now substitute the expression of the polarization (2.148) in the propagation equation (2.110) and move to the local time frame finding the following propagation equation:

$$\frac{dA_{AS}}{dz} = -\frac{3i\omega_{AS}}{4cn(\omega_{AS})}\chi^{(3)}(\omega_{AS})A_P^2 A_S^* e^{-i\Delta kz}, \tag{2.149}$$

Where $\Delta k = 2k_P - k_S - k_{AS}$. Let us now evaluate the CARS signal amplitude, after propagating over a distance L in a medium, integrating (2.149):

$$A_{AS}(L) = \int_0^L \frac{dA_{AS}}{dz} dz = -\frac{3i\omega_{AS}}{4cn(\omega_{AS})}\chi^{(3)}(\omega_{AS})A_P^2 A_S^* L \,\mathrm{sinc}\left(\frac{\Delta kL}{2}\right) e^{i\frac{\Delta kL}{2}}, \tag{2.150}$$

Where the function $\mathrm{sinc}(x) = \sin(x)/x$. We can now calculate from (2.150) the intensity of CARS I_{AS} knowing that $I \propto |A|^2$:

$$I_{AS}(L) \propto |\chi^{(3)}|^2 L^2 \,\mathrm{sinc}^2\left(\frac{\Delta kL}{2}\right) I_P^2 I_S, \tag{2.151}$$

Equation (2.151) represents the expression of the CARS signal coming out of a medium with length L. Several considerations can be made:

1. The signal depends quadratically on the pump intensity and linearly on the Stokes one. Therefore, increasing the pump intensity is more beneficial to enhance the signal.

2. The signal depends quadratically[6] on the width of the medium L. Thus, it is hard to get signal from thin samples. The same reasoning could be applied to the concentration of scatterers: if it is close to zero, small variations of concentration are hardly detected due to the square dependence on it.

3. In order to get high intensity, the phase matching condition should be respected,

[6]The quadratic dependence of the CARS signal is due to its quadratic dependence on $\chi^{(3)}$, which will be introduced in subsection section 2.3.7

namely:

$$\Delta k = 2k_P - k_S - k_{AS} \simeq 0, \tag{2.152}$$

Where the wave vectors can be written as:

$$k_P = \frac{n_P \omega_P}{c}, \quad k_S = \frac{n_S \omega_S}{c}, \quad k_{AS} = \frac{n_{AS} \omega_{AS}}{c}, \tag{2.153}$$

Where $n_i = n(\omega_i)$. Due to the material dispersion, in general $n_P \neq n_S \neq n_{AS}$, and the phase matching condition is not satisfied. However, in condition of tight focusing, which can be assumed in microscopy, ΔkL is approximately equal to zero. Therefore, since $\lim_{x\to 0} \mathrm{sinc}(x) = 1$, the CARS intensity can be written as:

$$I_{AS}(L) \propto |\chi^{(3)}|^2 L^2 I_P^2 I_S. \tag{2.154}$$

4. The CARS intensity depends on $|\chi^{(3)}|^2$. In the next section we will find the expression of the third order susceptibility and then we will describe the consequences of the dependence on its modulus square.

2.3.7. Resonant and non-resonant contribution to CARS

In the previous section the CARS process has been described analyzing the four-wave mixing propagation equation generating a signal oscillating at ω_{AS}. Let us now describe this phenomenon looking at the Jablonsky diagrams reported in fig. 2.16.

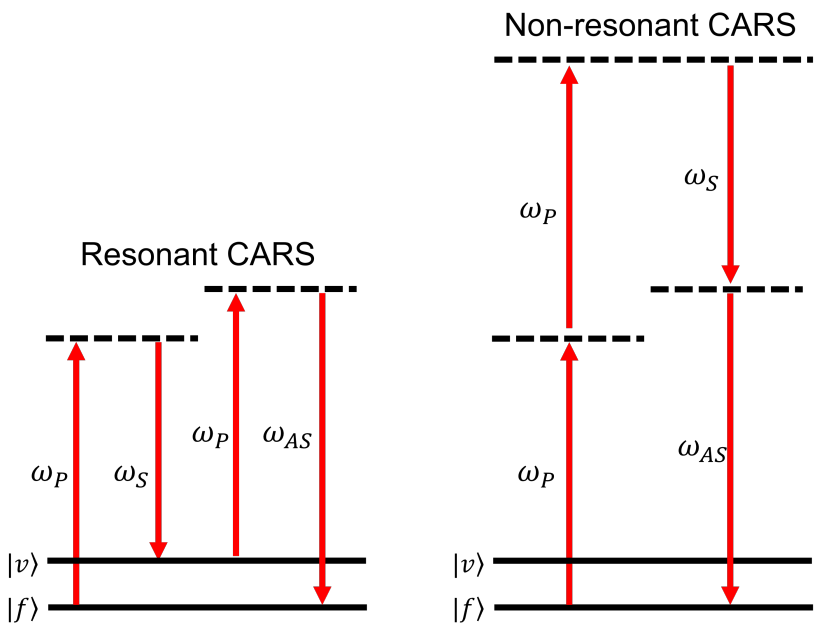

(a) Resonant Coherent anti-Stokes Raman scattering.

(b) Non-resonant Coherent anti-Stokes Raman scattering.

Figure 2.16: Jablonsky diagrams of (a) Resonant Coherent anti-Stokes Raman scattering (Resonant CARS), (b) Non-resonant Coherent anti-Stokes Raman scattering (Non-resonant CARS).

As we can see, there are two different processes giving rise to a signal at frequency ω_{AS}. In the first case, a molecule is excited to a virtual level by the pump electric field. Then, stimulated by the Stokes field, it relaxes to a vibrational level. Subsequently, it is excited again by the pump field, reaching a new virtual state. Finally, it relaxes to the ground state emitting an electromagnetic wave at frequency ω_{AS}. This contribution is called Resonant CARS, and it carries information about the energy of the vibrational state, which can be calculated as $E_{|v\rangle} = \hbar\Omega_R = \hbar\omega_{AS} - \hbar\omega_P$. The other contribution is called Non-Resonant CARS. In this case, after the molecule is excited by the pump field, reaching an intermediate virtual state, it interacts with the pump field again, reaching a new virtual state. Afterwards, stimulated by the Stokes field, it relaxes to the ground state emitting a Stokes and an anti-Stokes waves. In this last process there is no interaction with the molecule vibrational state, indeed, it originates from the instantaneous electronic response of the medium. Both the contributions appear in the expression of the third order susceptibility, which can be written as the sum:

$$\chi^{(3)} = \chi_R^{(3)} + \chi_{NR}^{(3)}, \tag{2.155}$$

Far from electronic resonances, the non-resonant susceptibility $\chi^{(3)}_{NR}$ is real and constant. On the other hand, the resonant part $\chi^{(3)}_{R}$ is characterized by a real and an imaginary part and is related to the vibrational modes. Comparing the expression (2.140) of the polarization we found in section section 2.3.5 and expression (2.148), found in section section 2.3.6, we obtain that:

$$\chi^{(3)}_{R} = \frac{4}{3A_P A^*_S} N \left(\frac{\partial \alpha}{\partial x}\right)_0 x(\Omega) \tag{2.156}$$

We can plug in (2.156) the expression of $x(\Omega)$ found in (2.137) obtaining:

$$\chi^{(3)}_{R} = \frac{a_{VIB}}{(\Omega - \Omega_R) + i\gamma}, \tag{2.157}$$

With $a_{VIB} = -\frac{2N\epsilon_0}{3\mu\Omega_R}\left(\frac{\partial \alpha}{\partial x}\right)^2_0$, a negative number which represents the oscillator strength of the molecular vibration. We implicitly assumed that there is only one vibrational mode, however, expression (2.157) can be easily extended to a complete vibrational spectrum with M different modes describing the third order susceptibility as:

$$\chi^{(3)}_{VIB} = \sum_{i=1}^{M} \frac{a_{VIB,i}}{(\Omega - \Omega_{R_i}) + i\gamma_i} + \chi^{(3)}_{NR} \tag{2.158}$$

Where $\chi^{(3)}_{R} = \sum_{i=1}^{M} \frac{a_{VIB,i}}{(\Omega - \Omega_{R_i}) + i\gamma_i}$ represents the resont part in (2.158). For simplicity, in the following it will be considered just one vibrational mode. Let us now consider the CARS signal intensity and its dependence on the square modulus of $\chi^{(3)}$:

$$I_{AS} \propto \left|\chi^{(3)}\right|^2 \propto \left|\chi^{(3)}_{R} + \chi^{(3)}_{NR}\right|^2 \tag{2.159a}$$

$$\propto \left|\chi^{(3)}_{R}\right|^2 + \left|\chi^{(3)}_{NR}\right|^2 + 2Re\left[\chi^{(3)}_{R} + \chi^{(3)*}_{NR}\right] \tag{2.159b}$$

$$\propto \left|\chi^{(3)}_{R}\right|^2 + \left|\chi^{(3)}_{NR}\right|^2 + 2\chi^{(3)}_{NR} Re\left[\chi^{(3)}_{R}\right], \tag{2.159c}$$

Where in the last passage we considered that $\chi^{(3)}_{NR}$ is real. Analyzing (2.159c), it is possible to observe that the CARS intensity is the sum of three different contributions:

1. A resonant contribution, given by the term $\left|\chi^{(3)}_{R}\right|^2$. This term contains the information regarding the vibrational modes and it is meaningful in spectroscopy applications.
2. A non-resonant contribution, given by the term $\left|\chi^{(3)}_{NR}\right|^2$. This term is almost constant

in the spectral domain if far from electronic resonances.

3. In the last term, $2\chi^{(3)}_{NR} Re\left[\chi^{(3)}_{R}\right]$, the resonant and non-resonant parts are mixed together giving rise to a heterodyne contribution.

The CARS signal can be seen as an interference between two waves, one generated by the resonant contribution, and the other by the non-resonant one. As a result of this interference, the last term appears. The CARS spectrum appears distorted with respect to the Spontaneous Raman spectrum due to the contributions of the second and third terms of the equation, which give rise to the so called Non-resonant Background (NRB). A representation of the different contributions to the CARS signal is reported in fig. 2.17.

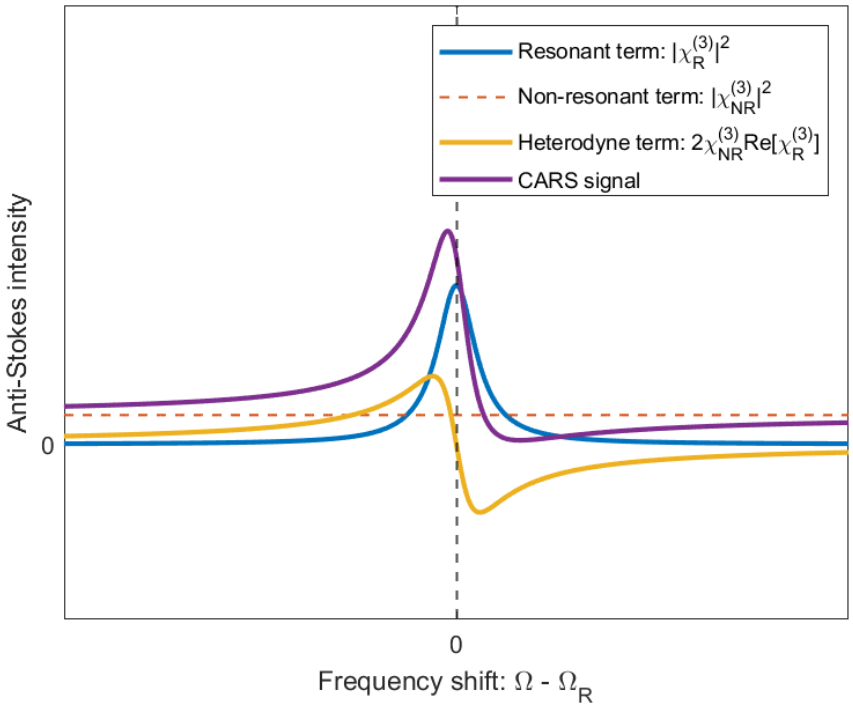

Figure 2.17: Anti-Stokes signal in the spectral domain: the contributions from the resonant, non-resonant and heterodyne terms are highlighted.

The NRB modifies the resonant signal red-shifting the maximum of the peaks, and makes it appear a minimum blue-shifted with respect to the Raman peak. Decreasing the ratio between the resonant and the non-resonant part of the third order susceptibility, the CARS signal is progressively more distorted, as it can be seen in fig. 2.18.

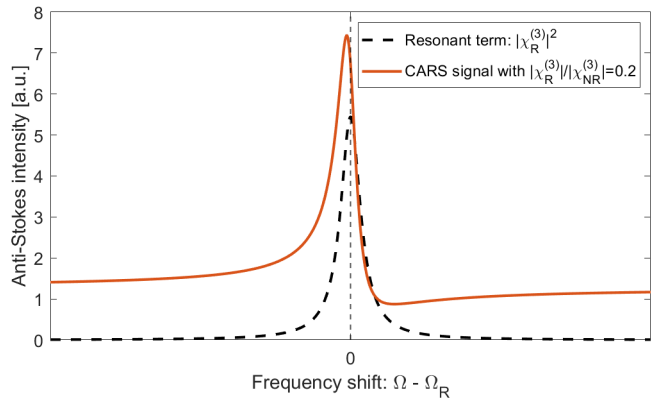

(a)

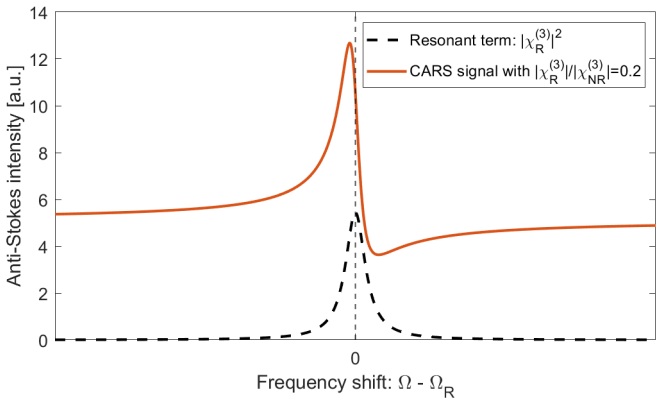

(b)

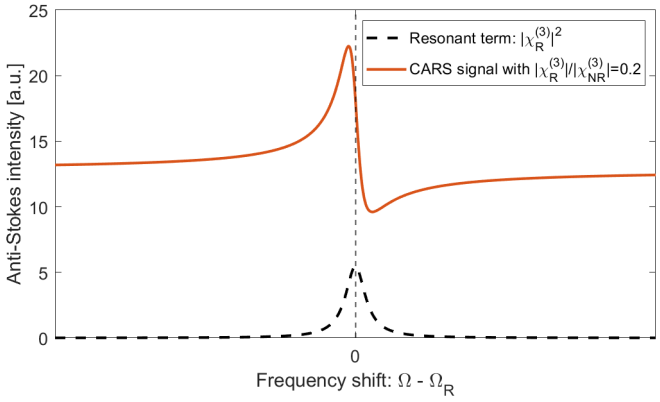

(c)

Figure 2.18: CARS signal varying the ratio between the resonant and the non-resonant contributions, respectively with (a) $\frac{|\chi_R^{(3)}|}{|\chi_{NR}^{(3)}|} = 2$, (b) $\frac{|\chi_R^{(3)}|}{|\chi_{NR}^{(3)}|} = 0.5$, (c) $\frac{|\chi_R^{(3)}|}{|\chi_{NR}^{(3)}|} = 0.2$.

The NRB signal shows some differences with respect to the resonant one.

1. At resonance, the NRB is dephased with respect to the resonant contribution.
2. Since the resonant contribution arises from the population of a vibrational level,

it will have a population time in the order of the nanoseconds and coherence time tipically in the order of the picoseconds. On the other hand, the NRB arises from electronic contribution, in which only virtual levels are populated. The virtual electronic levels show an extremely short coherence time, in the order of hundreds of femtoseconds.

Since only the resonant term is carrying information regarding the vibrational modes and therefore is the only meaningful part for spectroscopic applications, it is generally desired to remove the NRB from the CARS signal.

2.3.8. Broadband CARS

In the previous sections, the CARS process has been described considering narrowband picosecond pump and Stokes beams. This regime, called single-frequency regime, allows to reach extremely high acquisition speeds, up to the video-rate [44, 45]. However, the information content is strongly reduced with respect to SR, since the narrowband pulses allow one to probe a single vibrational transition. Broadband CARS represents the solution to this problem, since it allows to reach an information content comparable to SR spectroscopy retaining the high-speed acquisition, as shown in fig. 2.19.

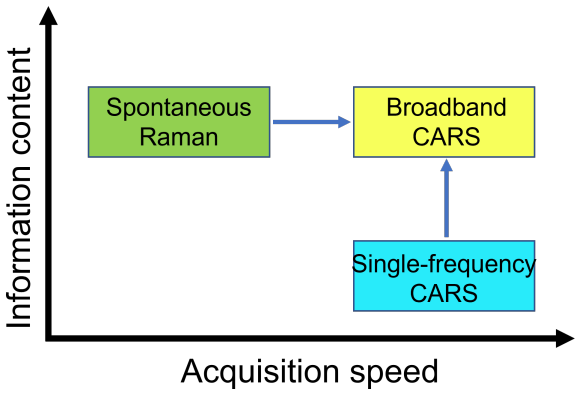

Figure 2.19: Comparison between SR and CARS techniques in terms of imaging speed and information content. Adapted from [20].

Despite numerous advancements in the detection systems that have increased speed and broadened spectral coverage, many B-CARS systems are built to capture Raman spectra only in the CH-stretching region [46] (2800 - 3100 cm^{-1}), a spectral range with a high density of oscillators. Accurate identification within chemically heterogeneous biological samples is difficult due to the rather vague spectral information in this region. The low wavenumber spectral area, commonly referred to as the "fingerprint", on the other

hand, exhibits sharp and identifiable peaks that offer excellent biological specificity [66]. The fingerprint region, however, has lower Raman signals, necessitating either longer integration times or greater average Stokes and pump beam powers to achieve a high enough SNR. The biological samples that were scanned might be harmed as a result of these restrictions. Furthermore, the Raman peaks in the fingerprint area have narrow linewidths and are spectrally crowded, necessitating the technical achievement of both high spectral resolution (down to 10 cm^{-1}) and extensive spectral coverage.

In the literature, a number of B-CARS microscopy setups covering the fingerprint region have been described. While some of them (the so-called hyperspectral CARS method [67]) take use of the quick frequency tuning of one of the two narrowband beams, multiplex CARS [47–51] aims to simultaneously measure the entire spectrum, including the fingerprint and the CH-stretching regions.

In multiplex CARS, the pump and Stokes frequencies are provided by a single ultrabroadband laser [68, 69] or by combining a narrowband pump with a broadband Stokes achieved through supercontinuum generation in a tapered fiber [52] or a photonic crystal fiber (PCF) [53, 54]. There are several ways to implement multiplex B-CARS detection: some are based on a time-domain Fourier transform approach [55–57] or use frequency combs [58], while others detect the signal in the frequency domain. In the frame of time-domain Fourier transform approach, Hashimoto *et al.* [39] reached the record acquisition speed of 24000 spectra/s covering the whole fingerprint region (200-1500 cm^{-1}). Exploting a multiplex approach, Camp *et al.* [47] managed to obtain ultrabroadband CARS signal (500-3500 cm^{-1}) with a pixel exposure time of 3.5 ms.

In the following chapter, we will describe a novel method for B-CARS that uses an amplified femtosecond ytterbium laser system operating at a 2-MHz repetition rate to produce pulses at 1035 nm with significantly more energy (at the μJ level) than conventional systems, typically operating at 40 or 80 MHz. This opens up two important benefits. The first is the potential to produce ultrabroadband red-shifted Stokes pulses that cover the entire relevant spectral region area (500-3100 cm^{-1}) exploiting supercontinuum (SC) generation [70] in a bulk crystal as opposed to PCFs, as was previously reported in literature. SC in bulk media represents a more compact, reliable, easy-to-use, and alignment-insensitive approach. It has outstanding long-term stability that is comparable with that of the pump laser source itself, significant mutual correlations between the intensities of its spectral components, and low pulse-to-pulse variations [59].

The lowered repeatition rate is the second benefit. On the one hand, a repetition rate of 2 MHz allows for a 0.5-μs temporal delay between two pulses, giving the system more time

to dissipate thermal energy and lessening photothermal damage [71]. On the other hand, for a given average power at the focus, constrained by sample degradation, more pulse energy leads to higher peak intensity, which, due to the non-linear nature of the optical effect, provides a stronger B-CARS signal. Therefore, higher SNR and/or acquisition speed can be reached, without sacrificing sample integrity.

The B-CARS signal is generated overlapping the narrowband pump pulse and the broadband Stokes pulse, obtained through SC generation. In this way, several vibrational modes are stimulated simultaneously allowing to obtain a ultrabroad CARS vibrational spectrum. The resolution is provided by the narrowband pump, therefore, it is beneficial to shrink its spectrum, but still preserving a pulse duration of around $1ps$ to successfully excite the modes of vibration.

An example of B-CARS signal obtained experimentally is reported in fig. 2.20:

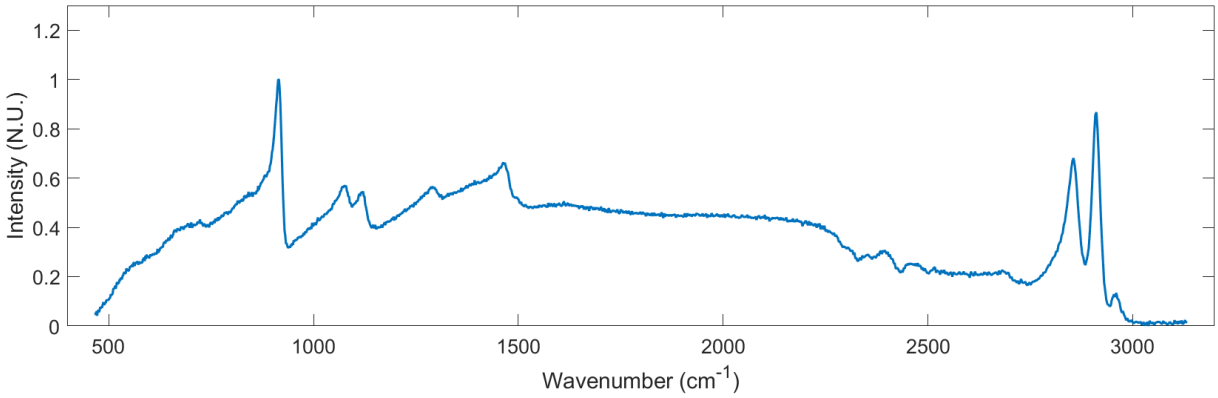

Figure 2.20: Example of experimentally measured B-CARS signal from Ethanol, spanning from 500 cm^{-1} to 3100 cm^{-1}.

It can be observed that the obtained spectrum covers both the fingerprint and the C-H stretching regions. The resonant and non-resonant contributions are both present, indeed the shape of the spectrum is different from the SR ones (an example of SR spectrum is reported in fig. 2.14). In order to retrieve the expected Lorentzian peaks, it is necessary to perform post-processing algorithms, which will be explained in section 3.3.

2.3.9. Two-color and three-color CARS

In section 2.3.7, we described the CARS process through the Jablonsky diagram in fig. 2.16a, however, in the Broadband CARS frame, two different processes can be distinguished depending on the order of interactions with the pump and Stokes pulses. In two-color CARS, the first interaction between light and matter is with a pump photon,

promoting the molecule to a virtual level, subsequently, the molecule, stimulated by the Stokes photon, decays reaching a vibrationally excited level. In the B-CARS picture, due to the broad spectrum of the Stokes pulse, many levels can be reached. Then, another pump photon acts as a probe, exciting the molecule to other virtual levels. Finally, the molecule decays emitting an anti-Stokes photon, giving rise to the CARS signal.

On the other hand, in three-color CARS, the first interaction is with a Stokes photon (which acts as a pump), which excites the molecule to a virtual level. Then, due to another interaction with the Stokes pulse, it decays to a vibrational level. Therefore, it is possible to observe this process only if the Stokes spectrum is broad and if all the colors arrive almost simultaneously, in order to allow two interaction with the same pulse (intra-pulse excitation). Subsequently, as in two-color CARS, a pump photon acts as a probe; the molecule reaches another virtual level and then decays emitting an anti-Stokes photon. The two processes are schematically shown in fig. 2.21.

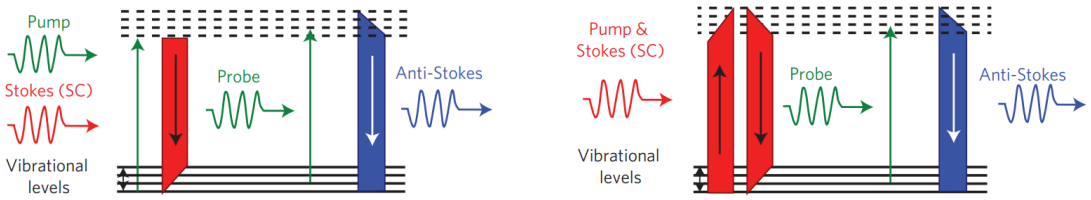

(a) Two-color CARS. (b) Three-color CARS.

Figure 2.21: Jablonsky diagram of (a) Two-color and (b) Three-color CARS. Adapted from [47].

In the three-color process, the source of the first two interactions is the same (intrapulse excitation), namely the Stokes pulse. Therefore, the excitation profile is determined by the permutations of available frequencies (energies) of light. Since the highest number of permutations is for closely spaced frequencies, the three-color excitation profile increases with decreasing wavenumber [47]. This makes three-color CARS particularly suitable for stimulating Raman transitions in the fingerprint region.

2.3.10. Time-delayed CARS

The difference in origin between resonant and non-resonant signals in CARS suggests a straightforward method for discriminating between the two contributions. The first two fields in vibrationally resonant CARS produce coherence in the medium. In the condensed phase, this coherence often lasts for picoseconds. Contrarily, the NRB is extremely short-lived, with the biggest contribution lasting only as long as the excitation pulse [72].

Since the non-resonant contribution has a coherence time much shorter than the resonant one, it is possible to isolate the resonant contribution increasing the delay between the second and third interactions between light and matter. This technique is called Time-delayed CARS (T-CARS).

In order to excite two-color CARS, there must be pump photons before and after the Stokes ones, therefore, a complete overlapping of the two pulses is needed. Thus, it is not possible to introduce a delay between the second and third interactions. On the other hand, three-color CARS is particularly suitable for realizing T-CARS. Indeed, the overlapping between the two pulses is not needed, since the pump pulse acts simply as a probe, and a certain delay is allowed. However, to obtain this result, it is necessary to compress the Stokes pulse and to avoid any temporal overlap between the pulses, since this would give rise to an unwanted non-resonant contribution. The main advantage of T-CARS is the physical NRB removal. Therefore, the obtained spectra are comparable to the SR ones without the need of post-processing. However, since the NRB also allows the amplification of the CARS signal, removing it reduces the sensitivity and consequently the acquisition time is increased.

2.3.11. Epi-detected CARS

In eq. (2.154) we found that the CARS signal is proportional to the square of the thickness of the illuminated sample. In order to obtain this result, it has been necessary to assume that the phase matching condition was satisfied, namely $\Delta \boldsymbol{k} L = 0$, in which $\Delta \boldsymbol{k} = 2\boldsymbol{k_P} - \boldsymbol{k_S} - \boldsymbol{k_{AS}}$. This approximation is generally valid for microscopy, since the tight focusing condition in achieved. However, till now we implicitly considered the forward propagating signal (F-CARS). If we took into account the backward propagating signal, even in tight focusing condition, the phase matching would not be possible. A scheme of a microscope able to detect both F-CARS and E-CARS is depicted in fig. 2.22.

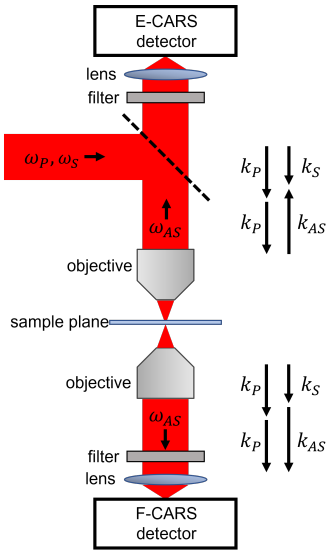

Figure 2.22: Scheme of E-CARS and F-CARS experimental set-up.

For backward propagating CARS, also called epi-detected CARS (E-CARS), the intensity can be calculated as [73]:

$$I_{AS}(L) \propto |\chi^{(3)}|^2 L^2 \,\mathrm{sinc}^2\left(\frac{|\boldsymbol{\Delta k}|L}{2}\right) I_P^2 I_S, \tag{2.160}$$

In this case, the only way to get $|\boldsymbol{\Delta k}|L \simeq 0$ is with $L \simeq 0$. Let us consider a thin sample immersed in a solvent. Since the F-CARS signal is proportional to L^2, the solvent signal will overwhelm the one of the sample, due to $L_{sample} \ll L_{solvent}$. On the other hand, the E-CARS signal of the solvent will be strongly reduced since the phase matching condition is not respected, while the sample's one will remain almost equal, since $|\boldsymbol{\Delta k}|L_{sample} \simeq 0$ is realized in both directions. Therefore, epi-detected CARS allows to enhance the signal to noise ratio of small scatterers with respect to the background signal coming from the solvent [73].

If the dispersion of the refractive index is negligible ($n_S \simeq n_P \simeq n_{AS} \simeq n$), it is possible to give an estimate of the critical thickness L_{crit} over which the E-CARS signal drops. Considering that the first zero of $\mathrm{sinc}(x)$ is for $x = \pi$, the required condition to have a relevant E-CARS signal is: $|\boldsymbol{\Delta k}|L \ll \pi$. For epi-detected CARS, assuming a collinear geometry:

$$|\boldsymbol{\Delta k}| = 2k_{AS} = \frac{4n\pi}{\lambda_{AS}}, \tag{2.161}$$

Hence, applying the condition $|\boldsymbol{\Delta k}|L \ll \pi$ to eq. (2.161), we get E-CARS if:

$$L \ll \frac{\lambda_{AS}}{4n}, \tag{2.162}$$

Thus, the epi-detected signal coming from sub-wavelength scatterers is enhanced with respect to the background coming from the solvent.

2.4. Supercontinuum generation

In this section, the non-linear optical processes giving rise to supercontinuum (SC) generation will be described. SC generation in bulk media will be analyzed in further detail.

2.4.1. Self Phase Modulation

In section 2.2.3, the four-wave mixing (FWM) phenomena have been described by means of the propagation equations. The goal of this section is to analyze in further detail one of the most common processes that arises during propagation, namely the Self Phase Modulation (SPM). In order to describe it, we assume the condition of degenerate FWM, which is characterized by the relation $\omega_1 = \omega_2 = \omega_3 = \omega_4 \equiv \omega_0$. Therefore, since also $k_1 = k_2 = k_3 = k_4$, we find that $\Delta k = 0$, thus, the process is always phase matched. Let us consider an incoming electric field, in this case written as:

$$E(t,z) = Re\left\{A(t,z)e^{i(\omega_0 t - k_0 z)}\right\}, \tag{2.163}$$

Let us now plug (2.163) in one of the propagation equations (2.110) (which are equivalent in case of degenerate FWM):

$$\frac{\partial A}{\partial z} + \frac{1}{v_g(\omega_0)}\frac{\partial A}{\partial t} = -\frac{i3\omega_0\chi^{(3)}}{8cn(\omega_0)}|A|^2 A, \tag{2.164}$$

Till now, we described the pulses propagation in the laboratory frame, that is, we made use of the set of spatio-temporal coordinates x, y, z, t. In many cases, it is beneficial to move to the local time frame, where the time is centered on the peak of the pulse. The set of spatio-temporal coordinates becomes: x, y, z, T, where T is defined as: $T \equiv t - \frac{z}{v_g(\omega_0)}$, where ω_0 is the central frequency of the pulse. Moving to the local time frame, it is necessary to change the partial derivative in space and time as follows:

$$\frac{\partial}{\partial t} \Rightarrow \frac{\partial}{\partial T} \quad \frac{\partial}{\partial z} \Rightarrow \frac{\partial}{\partial z} - \frac{1}{v_g(\omega_0)}\frac{\partial}{\partial T} \tag{2.165}$$

Thus, making use of (2.165), we can rewrite (2.164) as:

$$\frac{\partial A}{\partial z} + i\gamma|A|^2 A = 0, \tag{2.166}$$

Where γ is defined as $\gamma \equiv \frac{3\omega_0\chi^{(3)}}{8cn(\omega_0)}$. Let us now solve the equation (2.166) considering the following Ansatz:

$$A(z,T) = A(z=0,T)e^{i\phi(z,T)}, \tag{2.167}$$

Let us calculate the spatial derivative of the Ansatz (2.167):

$$\frac{\partial A}{\partial z} = i\frac{d\phi}{dz}A(z,T), \tag{2.168}$$

We can now plug (2.167) and (2.168) in (2.166) obtaining:

$$iA\frac{d\phi}{dz} + i\gamma|A|^2 A = 0, \tag{2.169}$$

Simplifying the equation we obtain:

$$\frac{d\phi}{dz} = -\gamma|A|^2, \tag{2.170}$$

It is possible to observe that there are no changes in the envelope during propagation, since $|A(z,T)|^2 = |A(z=0,T)|^2$. We can exploit this relation to solve (2.170), obtaining:

$$\phi(z,T) = -\gamma|A(z=0,T)|^2 z, \tag{2.171}$$

Therefore, the solution of equation (2.166) is:

$$A(z,T) = A(z=0,T)e^{-i\gamma|A(z=0,T)|^2 z}, \tag{2.172}$$

In conclusion, in case of propagation of pulses in third-order non-linear materials, where the dispersion has been neglected for simplicity, the envelope does not change, while the phase varies proportionally to the modulus square of the envelope at $z = 0$. Since the phase is modulated proportionally to the pulse itself, this phenomenon is called Self Phase Modulation [60].

The propagating electric field can be written as:

$$E(z,T) = Re\left\{A(z=0,T)e^{i[\omega_0 t - k_0 z - \gamma|A(z=0,T)|^2 z]}\right\}, \tag{2.173}$$

Where the phase in (2.173) is $\Phi(z,T) = i[\omega_0 t - k_0 z - \gamma|A(z=0,T)|^2 z]$. Let us now evaluate the instantaneous frequency:

$$\omega(z,T) = \frac{d\Phi}{dt} = \omega_0 - \gamma z \frac{d}{dt}|A(z=0,T)|^2, \tag{2.174}$$

Analyzing (2.174), we can draw some conclusions. Firstly, during the propagation, the pulse is chirped, namely, different frequencies arrive at different times, in particular:

1. For $T < 0$, $\omega(T) < \omega_0$,
2. For $T > 0$, $\omega(T) > \omega_0$

Therefore, the chirp introduced by SPM is similar to the one introduced by positive GVD, in which the red components arrive before the blue ones.

Secondly, while going through the material, the spectrum of the pulse is broadened. Both the described feature can be seen in fig. 2.23

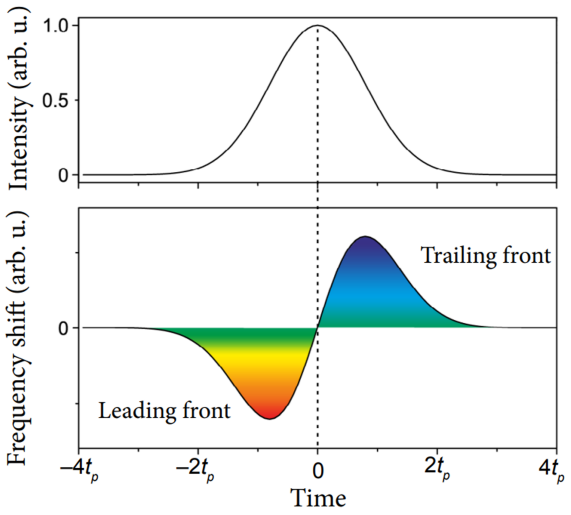

Figure 2.23: Pulse subjected to Self phase modulation: above, pulse intensity profile; below, variation of the instantaneous frequency. Adapted from [74].

2.4.2. Optical Kerr effect

The spatial counterpart of Self Phase Modulation is called Optical Kerr Effect. This phenomenon has the same origin of SPM, but can be analyzed from a different point of view. Let us assume the same initial conditions as the previous section, namely: degenerate Four Wave Mixing, so $\omega_1 = \omega_2 = \omega_3 = \omega_4 \equiv \omega_0$, where $\Delta k = 0$, and an incoming electric field described by (2.163).

Given these conditions, the third order polarization is described by one of the four equations in (2.106). We can write it, plugging in the electric field envelope and considering the degenerate FWM condition:

$$P^{(3)}_{\omega_0}(z,t) = \frac{3\epsilon_0\chi^{(3)}}{4}|A|^2 A e^{i(\omega_0 t - k_0 z)} + c.c., \tag{2.175}$$

Let us now take into account also the linear polarization, since both $P^{(3)}_{\omega_0}$ and $P^{(1)}$ are oscillating at ω_0. The linear polarization simply reads as:

$$P^{(1)}(z,t) = \epsilon_0\chi^{(1)}E(z,t) = \epsilon_0\chi^{(1)}Ae^{i(\omega_0 t - k_0 z)} + c.c., \tag{2.176}$$

Subsequently, the overall polarization oscillating at ω_0 can be found summing (2.175) and (2.176):

$$P_{\omega_0}(z,t) = \epsilon_0\chi^{(1)}Ae^{i(\omega_0 t - k_0 z)} + \frac{3\epsilon_0\chi^{(3)}}{4}|A|^2 A e^{i(\omega_0 t - k_0 z)} + c.c., \tag{2.177}$$

Expression (2.177) can be rewritten as:

$$P_{\omega_0}(z,t) = \epsilon_0\left[\chi^{(1)} + \frac{3\epsilon_0\chi^{(3)}}{4}|A|^2\right]E = \epsilon_0\chi E, \tag{2.178}$$

Where, in (2.178), χ is the generalized susceptibility, defined as:

$$\chi = \chi^{(1)} + \frac{3\chi^{(3)}}{4}|A|^2, \tag{2.179}$$

We can now generalize the relation $n_0^2 = \epsilon_r = 1+\chi^{(1)}$, in which n_0 is called the unperturbed refractive index, to the new expression of χ found in (2.179). Therefore, we can calculate the refractive index as:

$$n^2 = 1 + \chi = 1 + \chi^{(1)} + \frac{3\chi^{(3)}}{4}, \tag{2.180}$$

Proceeding with the calculations from (2.180), we find:

$$n = \sqrt{1 + \chi^{(1)} + \frac{3\chi^{(3)}}{4}} = n_0\sqrt{1 + \frac{3\chi^{(3)}}{4n_0^2}|A|^2}, \tag{2.181}$$

We can safely assume that $\frac{3\chi^{(3)}}{4n_0^2}|A|^2 \ll 1$, since it represents a small correction with respect to the unperturbed refractive index n_0. Thus, we can simplify (2.181) obtaining:

$$n \simeq n_0 + \frac{3\chi^{(3)}}{8n_0}|A|^2, \tag{2.182}$$

Let us take into account the expression of the intensity:

$$I(z,t) = \frac{1}{2}c\epsilon_0 n_0|A|^2, \tag{2.183}$$

From (2.183), we find:

$$|A|^2 = \frac{2I}{c\epsilon_0 n_0}, \tag{2.184}$$

We can now plug (2.184) in (2.182) finding:

$$n \simeq n_0 + \frac{3\chi^{(3)}I}{4c\epsilon_0 n_0^2}, \tag{2.185}$$

Analyzing (2.185), it is possible to define a new quantity, namely n_2, as:

$$n_2 = \frac{3\chi^{(3)}}{4c\epsilon_0 n_0^2}, \tag{2.186}$$

Finally, the Optical Kerr Effect is a correction of the refractive index dependent on the intensity of the pulse, and proportional to n_2, which is related to the third-order susceptibility of the material. Taking into account also the transverse profile of the pulse, starting from (2.185), and plugging in (2.186), we find:

$$n(t, \boldsymbol{r}) = n_0 + n_2 I(t, \boldsymbol{r}), \tag{2.187}$$

In order to understand the consequences of the Optical Kerr Effect on the propagation of the pulse, let us write the expression of the electric field of a pulse, taking into account the refractive index written in (2.187), and exploiting the relation with the wave number $k = \frac{\omega n}{c}$:

$$E = Re\left\{A\,\exp\left[i\left(\omega_0 t - kz\right)\right]\right\} = Re\left\{A\,\exp\left[i\left(\omega_0 t - \frac{\omega n_0}{c}z - \frac{\omega n_2}{c}zI\right)\right]\right\}, \tag{2.188}$$

We can extract the phase in (2.188) as:

$$\Phi(t,z) = \omega_0 t - \frac{\omega n_0}{c}z - \frac{\omega n_2}{c}zI, \tag{2.189}$$

Thus, the instantaneous frequency can be obtained deriving (2.189) in time:

$$\omega_i = \frac{d\Phi}{dt} = \omega_0 - \frac{\omega_0 n_2}{c}z\frac{dI}{dt}, \tag{2.190}$$

Equation (2.190), represents an expression analogous to (2.174), where the phase of the pulse changes due to the presence of the pulse itself. Therefore, the Optical Kerr Effect and the Self Phase Modulation are the same phenomenon, from two different perspectives.

Besides the temporal variation of the frequency, which has been analyzed in detail in the previous section, we can now evaluate the spatial consequence of the Kerr effect. Starting from (2.188), we can write the electric field in a slightly different manner, highlighting the accumulated phase, ϕ, over propagation:

$$E = Re\left\{A\,\exp\left[i\left(\omega_0 t - kz\right)\right]\right\} = Re\left\{A\,\exp\left[i\omega_0 t - i\phi\right]\right\}, \tag{2.191}$$

In (2.191) ϕ reads as:

$$\phi = \frac{\omega_0}{c}\left(n_0 + n_2 I(t,\boldsymbol{r})\right), \tag{2.192}$$

Hence, the accumulated phase over z is directly proportional to the intensity of the pulse. Let us take into account a gaussian-like pulse, where at $\boldsymbol{r} = \mathbf{0}$ we find the maximum intensity, while it decreases at the periphery. In this case, propagating in a third-order non-linear material, the central part of the pulse will experience a higher accumulated phase with respect to the periphery. Therefore, the material will behave as a lens, causing a focusing of the incoming light. Since the variation of the refractive index, which causes the lens-like behaviour, is due to the intensity profile itself, this phenomenon is called Self Focusing. A schematic representation of this phenomenon is depicted in fig. 2.24.

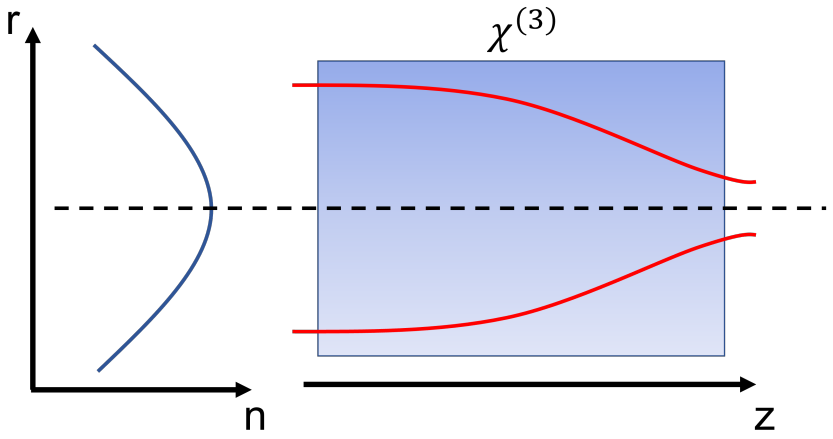

Figure 2.24: Schematic representation of Self-focusing. From the left, refractive index behaviour depending on the radial coordinate; $\chi^{(3)}$ material with propagation along the z-axis highlighting the focusing of the beam.

An excessive focusing could lead to an optical damage of the medium. However, Self Focusing is counterbalanced by a defocusing effect due to the generation of plasma, discussed in the next section.

2.4.3. Propagation of pulses in plasma

The self-focusing stage is a runaway effect in the sense that as the beam self-focuses, the intensity increases and so does the self-focusing effect. However, the beam cannot focus to a singularity; the beam collapse at the nonlinear focus is arrested by the multiphoton absorption and ionization, producing an energy loss and generating free electron plasma, which further absorbs and defocuses the beam [74].

In this section, the generation of plasma and its defocusing effect will be analyzed. Let us start with a simplified picture, which allows us to have a straightforward picture of the defocusing capability of plasma.

Let us assume that a plane wave is travelling through a medium characterized by the presence of plasma, which is an ensemble of positive or negative charges not bound. We will assume that only the electrons move inside the plasma, while the ions can be considered still. This approximation takes the name of Born-Oppenheimer approximation, and it is valid since, for the same electric field, electrons move thousand of times faster than ions due to the difference in mass at equal charge. Let us start from the propagation equation (2.12), in which we can now consider the plane wave approximation. Unlike how

we assumed in subsection 2.1.1, here the term $\mu_0 \frac{\partial J}{\partial t}$ can not be neglected, since there are free charges, and consequently there is a conduction current. Therefore, we obtain:

$$\frac{\partial^2 E}{\partial z^2} - \frac{1}{c^2}\frac{\partial^2 E}{\partial t^2} = \mu_0 \frac{\partial J}{\partial t}, \tag{2.193}$$

In which the conduction current can be written as:

$$J = -eN_e v, \tag{2.194}$$

In which, $e = 1.6 \cdot 10^{-19} C$ is the absolute value of the electron charge, N_e is the electron density in the medium and v is the electron velocity. Let us now calculate the time derivative of the conduction current (2.194):

$$\frac{\partial J}{\partial t} = -eN_e \frac{\partial v}{\partial t} = -eN_e a, \tag{2.195}$$

Where a is the electron acceleration. In equation (2.195) we implicitly assumed that the electron density remains the same over time, but we will relax this condition in the following. The electron acceleration can be calculated as:

$$a = \frac{F_e}{m_e} = \frac{-eE}{m_e}, \tag{2.196}$$

Plugging (2.196) in (2.195) we find:

$$\frac{\partial J}{\partial t} = \frac{e^2 N_e}{m_e} E, \tag{2.197}$$

Let us now plug (2.197) in (2.193):

$$\frac{\partial^2 E}{\partial z^2} - \frac{1}{c^2}\frac{\partial^2 E}{\partial t^2} = \frac{e^2 N_e \mu_0}{m_e} E, \tag{2.198}$$

Subsequently, the temporal Fourier transform is applied to (2.198), with $\tilde{E}(z, \omega) = \mathcal{F}\{E(z,t)\}$ and the Fourier property (2.27) is used, obtaining:

$$\frac{\partial^2 \tilde{E}}{\partial z^2} + \frac{\omega^2}{c^2}\tilde{E} = \frac{e^2 N_e \mu_0}{m_e}\tilde{E}, \tag{2.199}$$

Let us define the plasma frequency $\omega_p \equiv \sqrt{\frac{N_e e^2}{\epsilon_0 m_e}}$. We can write equation (2.199) as:

$$\frac{\partial^2 \tilde{E}}{\partial z^2} + \frac{\omega^2 - \omega_p^2}{c^2}\tilde{E} = 0, \tag{2.200}$$

Comparing (2.200) with the Helmoltz equation (2.33) and knowing (2.36), we can deduce that the refractive index in plasma is:

$$n_p = \sqrt{1 - \frac{\omega_p^2}{\omega^2}}, \tag{2.201}$$

Therefore, the larger is N_e the smaller is the refractive index n_p.

Till now we took into account plane waves propagating in a medium with a fixed density of free electrons N_e. We would like to extend the reasoning to the propagation of pulses, considering also the time-dependence of the free-electron density. We will make two approximations:

1. For every atom/molecule, only one electron can be detached.
2. Recombination among electrons and ions is neglected.

It is possible to prove that, even in this case, (2.197) is valid if we substitute the fixed electron density N_e with $n_e(t)$ defined as:

$$n_e(t) = N\left[1 - \exp\left(-\int_{\infty}^{t} w(t')dt'\right)\right], \tag{2.202}$$

Where, in equation (2.202), N is the density of atoms before the interaction and $w(t)$ is the ionization rate. The latter depends on the intensity as[7]:

$$w(t) \propto I^n, \tag{2.203}$$

Where, in equation (2.203), n is the number of photons to be absorbed in order to ionize the atoms. Therefore, taking into account also the definition of plasma frequency, we get:

$$\frac{\partial J}{\partial t} = \frac{e^2 n_e(t)}{m_e}E = \epsilon_0 \omega_{p,p}^2(t)E, \tag{2.204}$$

[7]We are implicitly assuming that we are in the multiphoton ionization regime, which is valid for Keldish parameter $\gamma \ll 1$. The Keldish parameter is calculated as $\gamma = \sqrt{\frac{I_p}{2U_p}}$, where I_p is the ionization potential and U_p is the ponderomotive energy.

Where the subscript "p,p" stands for "pulse, plasma". Equation (2.204) is formally equivalent to (2.197), therefore the same reasoning could be applied, retrieving:

$$n_{p,p} = \sqrt{1 - \frac{\omega_{p,p}^2}{\omega^2}}, \tag{2.205}$$

Unlike in (2.201), in (2.205) the electron density is not fixed, but depends on the ionization rate.

It is possible to observe that, since the ionization of electrons is caused by the pulse intensity, which is higher in the center, the center of the pulse experiences a smaller refractive index with respect to the periphery. Thus, the plasma acts as a defocusing lens, in which the accumulated phase is lower in the center.

2.4.4. Supercontinuum generation in bulk materials

In the previous sections, many non-linear phenomena have been described. When a high-intensity pulse propagates in a transparent medium, many of these processes are stimulated simultaneously, giving rise to a complex coupling between spatial and temporal effects. Eventually, a massive spectral broadening, preserving the spatial characteristics, can be induced. This phenomenon takes the name of Supercontinuum (SC) generation in bulk materials. The physical picture of SC generation in transparent bulk media could be understood in the framework of optical filamentation. Optical filamentation stems from the interplay between self-focusing, Self-Phase Modulation and multiphoton absorption/ionization-induced free electron plasma. In particular, the self-focusing induced by the Kerr effect is counteracted by the defocusing due to the propagation through plasma, generated by the pulse itself [75]. This interplay leads to the appearance of a stable structure called optical filament, that is able to propagate over extended distances much larger than the typical diffraction length while keeping a narrow beam size without the help of any external guiding mechanism. In fig. 2.25, the interplay between self-focusing (fig. 2.25 (a)) and defocusing due to plasma (fig. 2.25 (b)) giving rise to optical filamentation (fig. 2.25 (c)) are shown.

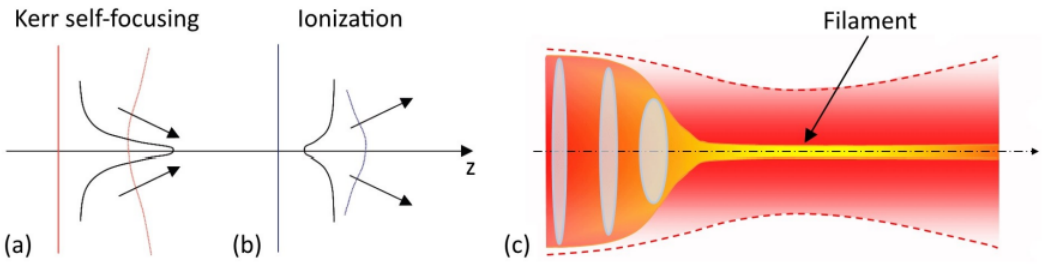

Figure 2.25: Schematic illustration of the filamentation process. (a) Self-focusing of a laser beam by optical Kerr effect. (b) Defocusing of the beam by the plasma. (c) Illustration of the collapse of the beam on itself by the Kerr effect leading to the ionization of the media with the consequent formation of a filament. Adapted from [76].

During the propagation, the pulse spectrum is broadened by the Self Phase modulation, as explained in section 2.4.1, and by the chromatic dispersion, which arises from the mismatch of GVD for different wavelengths. Furthermore, since new frequencies are generated, three-wave mixing processes are now possible, such as SFG or DFG[8], which give rise to a further broadening of the spectrum.

In the temporal domain, a pulse splitting can be observed. Due to the different spectral broadening induced by SPM on the two sides of the pulse, as can be seen in fig. 2.23, the leading front is centered on a lower frequency with respect to the trailing one. In case of normal GVD, lower frequencies propagate at higher velocity, thus, the leading front will travel faster than the trailing one, splitting the pulse in two. Moreover, for the same reason, a self-steepening of the two sub-pulses can be observed, originating from the different velocities of the sub-pulses peaks and tails. This last process induces a sharp intensity gradient in the temporal profile of the sub-pulses. As soon as the initial pulse splits, the spectrum is greatly broadened [74], as it can be seen experimentally and from numerical simulation, such as figure 2.26:

[8]Described in appendix A.1.

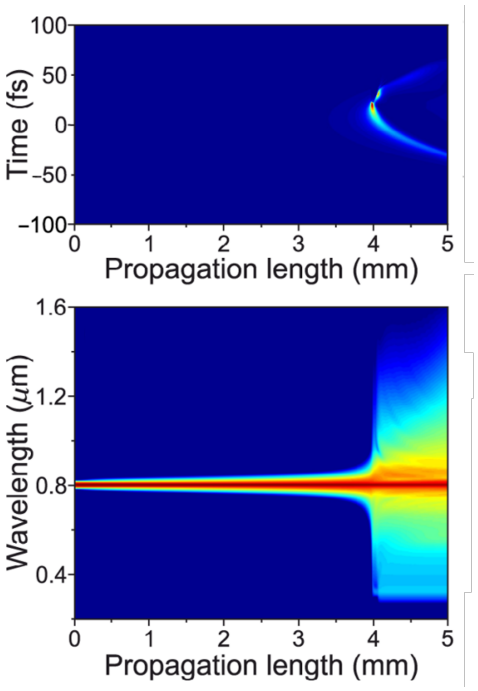

Figure 2.26: Top: numerically simulated temporal dynamics of 100 fs laser pulses propagating in a sapphire crystal with the input wavelengths of 800 nm in normal GVD medium. Bottom: corresponding spectral dynamics. Adapted from [74].

3 | Experiments and results

3.1. Experimental set-up

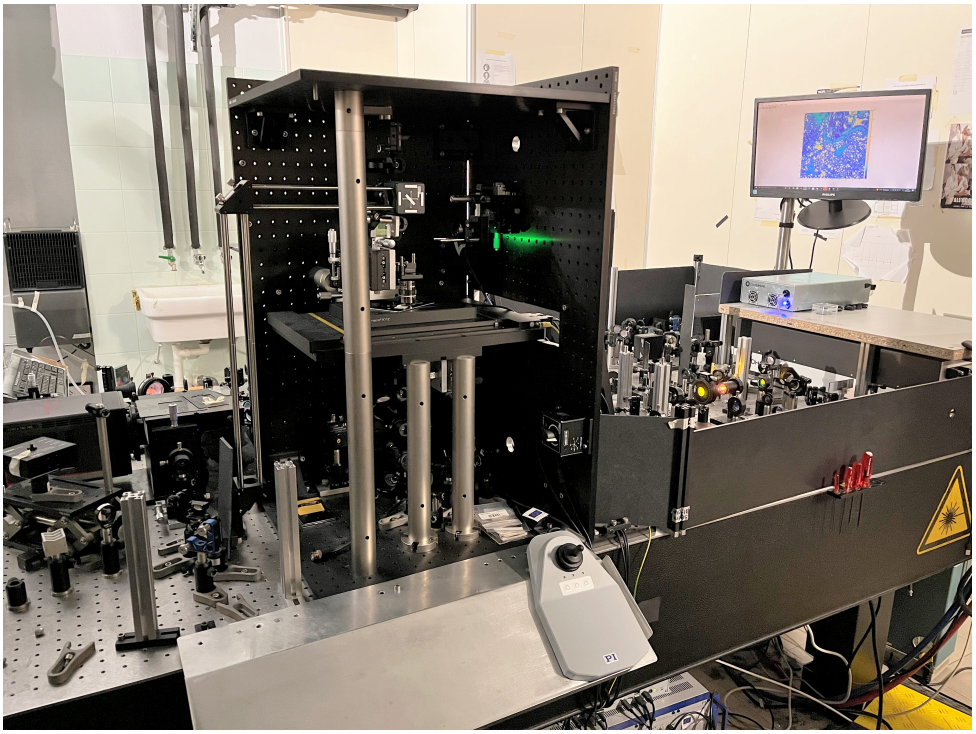

Figure 3.1: Picture of the experimental set-up.

The experimental set-up, shown in fig. 3.1, is based on a laser source (Monaco 1035, Coherent): a fiber-based Ytterbium pulsed laser system offering a wide range of output powers, till a maximum of 60 W, repetition rates, from 1 to 50 MHz and pulse durations, with a central wavelength at $\lambda_0 = 1035$ nm and a spectral bandwidth of 10 nm. A scheme of such set-up is depicted in fig. 3.2.

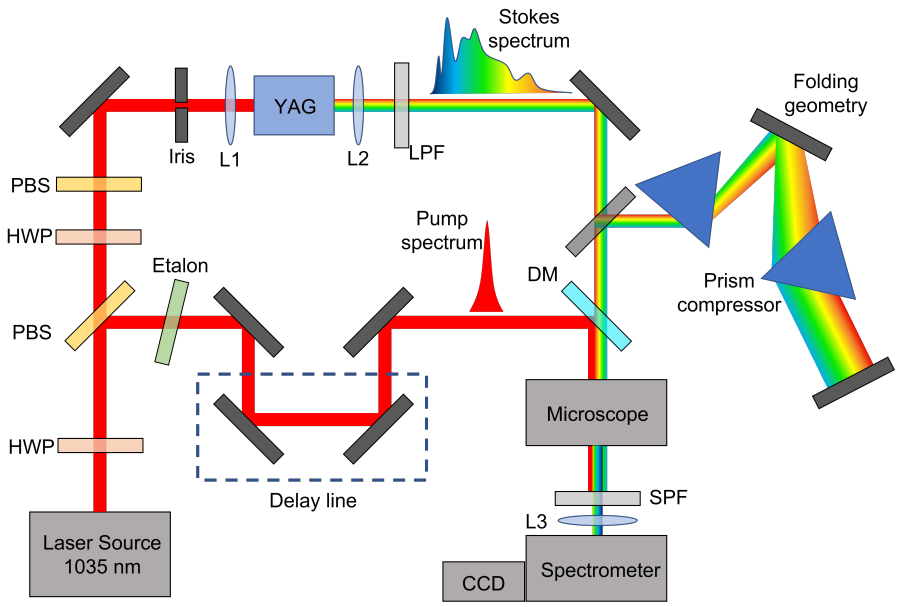

Figure 3.2: Scheme of the experimental set-up. Legend: HWP: half-wave plate; PBS: polarizing beam splitter; L1: 7.5 cm lens; L2: 7.5 cm lens; LPF: long pass filter; DM: dichroic mirror; SPF: short pass filter; L3: 3.5 cm lens.

For the experiments performed, a total output optical power of ≈ 5 W, a pulse duration of ≈ 268 fs and a repetition rate of 2 Mhz have been chosen.

The combination of a half-wave plate (HWP) and a polarizing beam splitter (PBS) allows to divide the initial beam into two replicas and to distribute the power in the two branches as desired.

The first replica passes through an etalon, which shrinks the bandwidth, generating narrowband pump pulses. The narrowband pump beam features $\simeq 1.1$ nm Full Width at half maximum, which for $\lambda_0 = 1035$ nm, gives a bandwidth in wavenumbers of approximately 10 cm^{-1}. It is crucial to have a narrowband pump pulse since its spectral bandwidth, together with the spectral resolution of the grating used to disperse the light after the microscopy unit, sets the spectral resolution in the CARS spectra. On the other hand, shrinking the bandwidth, the pulse duration increases due to the Fourier principle. It is important to keep the pulse duration in the order of 1 ps, in order to excite the molecular vibration in a impulsive way.

The other replica propagates through another HWP-PBS system, allowing to tune the intensity. Then, an iris allows to control the divergence of the beam, which is then focused by a 75 mm lens in a 10-mm-thick YAG crystal. The pulse energy of $\simeq 1.5\mu$J is enough for Supercontinuum generation in the near-infrared. Then, a second 75 mm lens ricollimates

the beam without changing the spot-size. Afterwards, a long pass filter (LP1050 or LP1200, Thorlabs depending on the experiment) selects the red shifted lobe of the SC (1050/1200-1600 nm), filtering out the fundamental. A picture of the SC generation is shown in fig. 3.3.

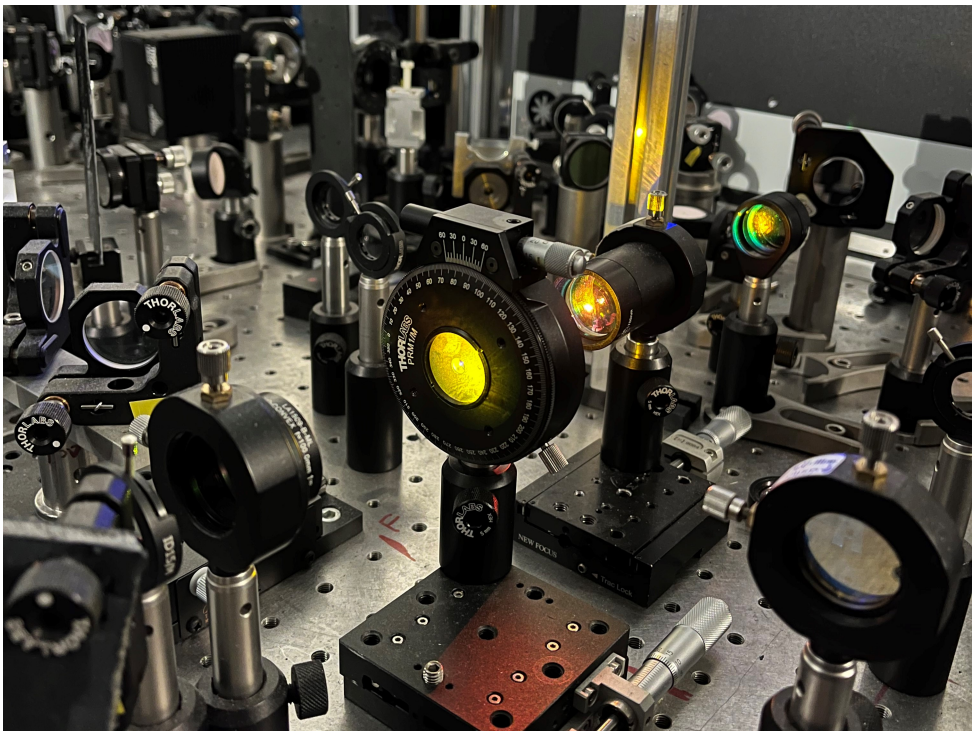

Figure 3.3: Picture of the SC generation stage.

The choice of the filter, and consequently of the Stokes bandwidth, depends on the experiment. Using LP1050 only the two-color spectrum is detected, while LP1200 is used to detect both two-color and three-color CARS. This second replica will be used as the Stokes pulse.

The optical path through the objectives and through the YAG crystal introduce a positive chirp characterized by a GDD $\simeq 8000$ fs^2. In order to compensate for this, a SF-11 prism compressor is employed with an apex-to-apex distance of 61 cm. A folding geometry was used in order to make the experimental set-up more compact. The goal of this part is to compensate in advance for the dispersion introduced by the microscope afterwards. Therefore, a negative GDD just after the prism compressor is desired. It can be observed that it is not necessary to compress the pump pulse because the initial duration is high enough to make the temporal broadening negligible, since, as explained in section 2.1.5, the longer is the pulse, the less the group velocity dispersion broadens it in time. Furthermore, the pump pulse spectrum is narrow, and the measured pulse duration ($\simeq 1$ ps, see section

3.2) is already close to the transform-limited one.

The spatiotemporal superposition of the two beams is realized using a dichroic mirror (Di02-R1064-25x36, Semrock) and a manual delay line mounted on the pump beam path.

Finally, the beams enters in a home-built confocal microscope (depicted in fig. 3.4) constituted of a pair of 100× air objectives (Olympus LCPLN100XIR, NA=0.85).

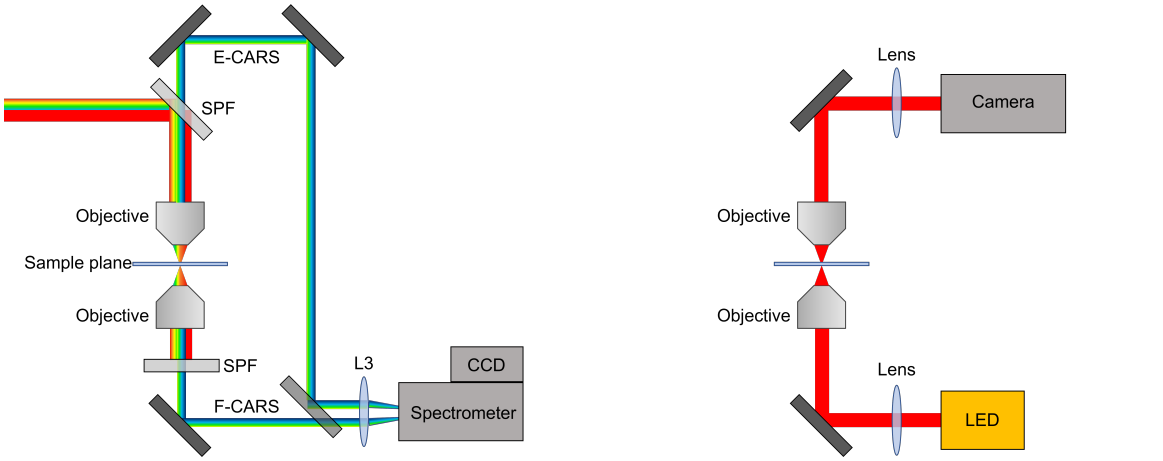

(a) Scheme of confocal nonlinear microscope detecting BCARS signal.

(b) Scheme of bright-field configuration.

Figure 3.4: Home-built confocal microscope. (a) Configuration exploited to detect the CARS signal, (b) configuration used to perform bright-field microscopy.

The pump and Stokes pulses are focused on the sample plane, then the E-CARS signal is recollimated by the first objective, while the F-CARS signal propagates through a second objective, identical to the first one. In both cases, the pulses go through a short pass filter (SP1000, Thorlabs), which selects the wavelengths below 1000 nm, filtering out pump and Stokes pulses while transmitting the CARS signal, since the last is centered at shorter wavelengths. Afterwards, the CARS signal is focused by a 3.5 cm lens (L3) on a spectrometer (Acton SP2150, Princeton Instrument), with a 600 gr/mm grating, which separates the different wavelengths. Then, the various frequencies reach a high-speed back-illuminated CCD Camera (BLAZE, Teledyne Princeton Instruments), characterized by an image area of 100 × 1340 pixels. The configuration described is used to perform high speed imaging in a raster scanning fashion. The sample is placed on a stepper motor controller which moves at constant speed on one axis and generates a trigger signal. Simultaneously, the CCD acquires a CARS spectrum at every trigger, performing a binning over the 100 rows, providing 1340 spectral points. The same procedure is repeated over many pixels, giving rise to an hyperspectral image. Every image is constituted of a

three-dimensional ($N \times M \times 1340$) matrix, where the first two dimensions represent the spatial axis, while the third dimension represents the spectral points.

The same microscope allows us to perform bright-field microscopy as well. In this case, a LED is used as light source, then a system composed by a lens, two objectives and another lens gives rise to a pseudo-Kohler illumination system. Finally, a camera (Thorcam, Thorlabs) in the image plane allows us to retrieve a wide-field image of the sample.

3.2. Sources characterization

In order to characterize the light sources used for the experiments, we employed a spectrometer (Avantes) and a non-collinear SHG-FROG set-up, described in section 3.2.1.

3.2.1. Frequency Resolved Optical Gating

Working with light in the pulsed regime, it is often needed to know the time duration, the shape and the spectrum of the pulses. There are several techniques which can be used to characterize them, however, when the pulse duration is in the order of tens or hundreds of fs this kind of measurement becomes challenging. Among the available techniques, frequency resolved optical gating [77] (FROG) is particularly robust and allows a complete characterization of a pulse, in particular, it allows to retrieve the electric field in time $E(t)$. Before describing the experimental set-up, the iterative approach exploited to find an unknown function $f(t)$, which represent the electric field $E(t)$, is described. A conceptual scheme can be found in figure 3.5.

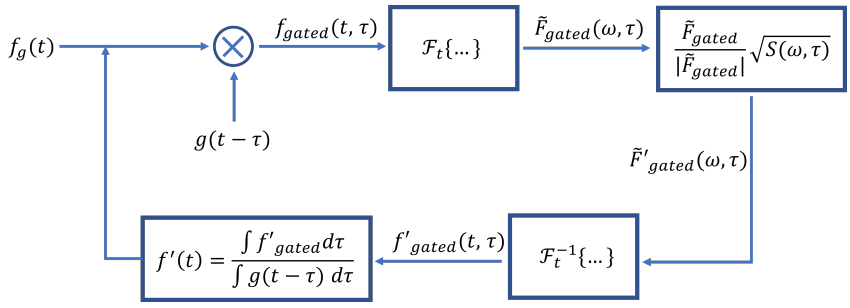

Figure 3.5: Conceptual scheme of the iterative algorithm used in FROG measurements.

Given an unknown function $f = f(t)$ and a known[1] gate function $g = g(t-\tau)$, where τ is the delay, let us define the gated function as: $f_{gated}(t,\tau) = f(t)g(t-\tau)$. The spectrogram

[1]The gating function could also be unknown, therefore this requirements will be relaxed in the following

of the gating function can be calculated as:

$$S(\omega, \tau) = |\mathcal{F}_t \{f_{gated}(t, \tau)\}|^2, \tag{3.1}$$

Where, in (3.1), $\mathcal{F}_t$ is the time Fourier transform. Knowing the spectrogram $S(\omega, \tau)$, which can be experimentally measured, it is possible to retrieve the unknown function $f(t)$ with the following iterative method:

1. An initial guess $f_g(t)$ is hypothesized.
2. Then, it is multiplied by the gating function obtaining $f_{gated}(t, \tau) = f_g(t)g(t - \tau)$.
3. Subsequently, the time Fourier transform is performed, finding the spectrogram $\tilde{F}_{gated}(\omega, \tau)$.
4. The amplitude of $\tilde{F}_{gated}$ is modified, in order to impose the right amplitude, which is the one of the spectrogram $S(\omega, \tau)$ measured experimentally exploiting (3.1), finding: $\tilde{F}'_{gated} = \frac{\tilde{F}_{gated}}{|\tilde{F}_{gated}|}\sqrt{S(\omega, \tau)}$.
5. Afterwards, the inverse Fourier transform is performed, obtaining: $f'_{gated}(t, \tau) = \mathcal{F}^{-1}\left\{\tilde{F}'_{gated}\right\}$.
6. Since we know that the gated function is the product of the unknown function $f(t)$, which is independent of the delay τ, and the known gating function $g(t - \tau)$, the following property holds:

$$\int_{-\infty}^{+\infty} f_{gated}(t, \tau)d\tau = \int_{-\infty}^{+\infty} f(t)g(t - \tau)d\tau = f(t)\int_{-\infty}^{+\infty} g(t - \tau)d\tau, \tag{3.2}$$

   Therefore, $f(t)$ could be retrieved from the integral in (3.2) as:

$$f(t) = \frac{\int_{-\infty}^{+\infty} f(t)g(t - \tau)d\tau}{\int_{-\infty}^{+\infty} g(t - \tau)d\tau}, \tag{3.3}$$

   Thus, since f'_{gated} is an estimate of the real f_{gated}, we can apply (3.3) as:

$$f'(t) = \frac{\int_{-\infty}^{+\infty} f'_{gated}(t, \tau)d\tau}{\int_{-\infty}^{+\infty} g(t - \tau)d\tau}, \tag{3.4}$$

7. Finally, we can substitute the initial guess $f_g(t)$ with $f'(t)$ and iterate till convergence.

Let us now describe the experimental setup which allows to perform such measurements.

The scheme of such set-up is reported in figure 3.6.

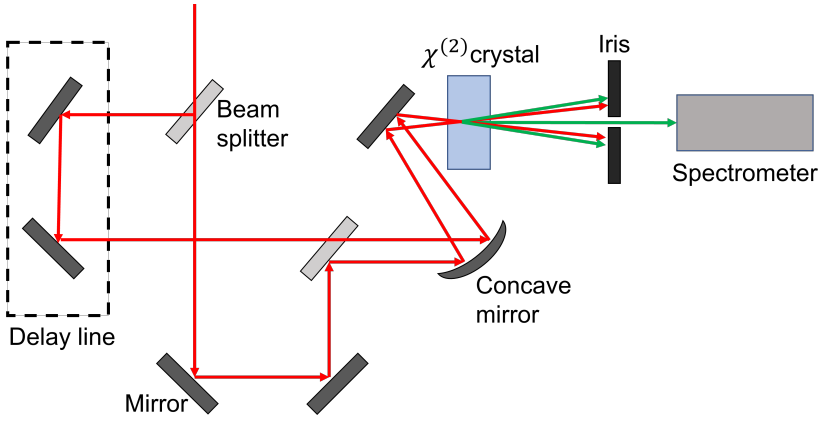

Figure 3.6: Conceptual scheme of the experimental set-up used to perform SHG-FROG.

There are many ways to implement a FROG set-up, such as polarization-gating FROG [78] or Self-diffraction FROG [79], which offer reliable results but are cumbersome to implement. On the other hand, Non-collinear Second Harmonic Generation FROG (Non-collinear SHG-FROG) offers the best trade-off between robustness and practical implementation, and therefore will be discussed and performed experimentally. As we can see in fig. 3.6, the pulse, which is described by the electric field in time $E(t)$, is splitted by a first beam splitter, generating two copy of the same pulse. Subsequently, one of the two copies is delayed by a quantity τ through a delay line (a set of two mirrors which can be moved in space), and is therefore described by $E(t-\tau)$. Finally, the two copies of the pulse are focused by mean of a concave mirror in a $\chi^{(2)}$ crystal, generating second harmonic of the two beams[2]. The set-up depicted in figure 3.6 is balanced: both the copies of the pulse go through the same amount of glass. Furthermore, a curved mirror instead of a lens is used to focus the beams, reducing the introduced dispersion. If the pulses are overlapping in time and space, the Sum frequency generation (SFG) can be stimulated (the green horizontal arrow depicted in figure 3.6). Only the SFG is selected through an iris and it is analyzed with a spectrogram.

From subsection A.1, we know that the electric field of the SFG is proportional to the product of the electric fields of the summing waves, therefore we can write:

$$E_{SF}(t,\tau) \propto E(t)E(t-\tau), \tag{3.5}$$

Thus, $E_{SF}(t,\tau)$ represents the gated function f_{gated} in the scheme described above, while

[2]Second order non-linear optical phenomena, such as Second Harmonic generation (SHG) or Sum frequency generation (SFG) are described in appendix A.1

$E(t)$ and $E(t-\tau)$ are respectively $f(t)$ and $g(t-\tau)$. Substituting (3.5) in (3.1), we measure the spectrogram as:

$$S(\omega,\tau) = \left|\mathcal{F}\left\{E_{SF}(t,\tau)\right\}\right|^2 \propto \left|\int_{-\infty}^{+\infty} E(t)E(t-\tau)e^{-i\omega t}dt\right|^2, \tag{3.6}$$

In which, moving the delay line in the experimental set-up, the time delay τ can be changed. Unlike before, the gating function $E(t-\tau)$ is unknown, however, it can be shown that the iterative procedure described above can be applied anyway. The main advantage of Non-collinear SHG-FROG is that it does not have any background, since the SF is generated only when the pulses are overlapping in time. Furthermore, we expect a symmetric spectrogram $S(\omega,\tau)$ with respect to τ, as it can be observed in the spectrogram in fig. 3.7 experimentally measured and reported as an example. This feature offers an additional way to check whether the measurement is performed correctly.

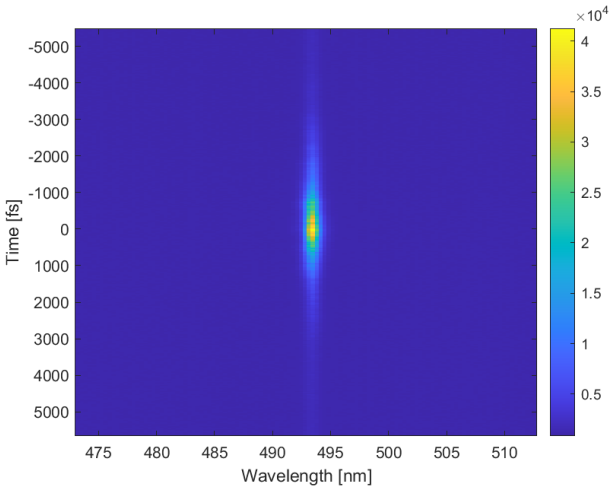

Figure 3.7: Example of spectrogram experimentally measured. The incoming pulse has central wavelength at 1035 nm and its duration is 1 ps.

Before performing the iterative analysis, it is also possible to have an estimate of the pulse duration analyzing $S(\omega,\tau)$. Integrating $S(\omega,\tau)$ over the frequencies, we obtain the energy of the SF pulse depending on the delay τ:

$$U_{SF}(\tau) \propto \int_{-\infty}^{+\infty} |E_{SF}|^2 dt = \int_{-\infty}^{+\infty} |E(t)|^2 |E(t-\tau)|^2 dt, \tag{3.7}$$

Exploiting the relation between electric field and intensity $I(t) = \frac{1}{2}c\epsilon_0|E(t)|^2$, we can

write (3.7) as:

$$U_{SF}(\tau) \propto \int_{-\infty}^{+\infty} I(t)I(t-\tau)dt = C_I(\tau), \tag{3.8}$$

In which $C_I(\tau)$ is the intensity autocorrelation function. Knowing $C_I(\tau)$ and measuring its full width at half maximum $\Delta\tau_{C_I}$, and making an assumption on the shape of the pulse, it is possible to get an estimate of the pulse duration Δt_{pulse} and of the intensity profile $I(t)$. In particular:

1. If $I(t)$ is a gaussian function, then $\Delta\tau_{C_I} = \sqrt{2}\Delta t_{pulse}$,
2. If $I(t)$ is a sech^2 function, then $\Delta\tau_{C_I} = 1.55\Delta t_{pulse}$,
3. If $I(t) = e^{-t/\tau_p}H(t)$, where $H(t)$ is the Heavyside function, then $\Delta\tau_{C_I} = 2\Delta t_{pulse}$,

Performing this kind of measurement on the spectrogram in figure 3.7 and assuming it has a sech^2 shape, we find the intensity profile depicted in figure 3.8 and a pulse duration equal to 1 ps.

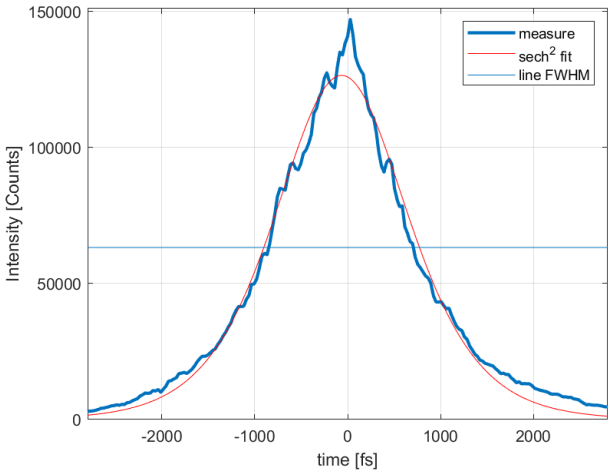

Figure 3.8: Intensity profile of the pump pulse obtained integrating the spectrogram over the wavelenghts.

The main drawback of SHG-FROG is that, since both the spectrogram $S(\omega, \tau)$ and the intensity auto-correlation $C_I(\tau)$ are symmetric with respect to the introduced delay τ, we do not get any information about the sign of the chirp of the pulse. A simple way to check whether the pulse presents positive or negative dispersion, is to repeat the measurement making the pulse pass through a piece of glass. In this way some positive group delay dispersion (GDD) is introduced. If Δt_{pulse} increases, then the initial GDD is positive, while if it decreases, the initial GDD is negative.

3.2.2. Pump pulse characterization

Let us begin with the characterization of the pump pulse before the etalon.

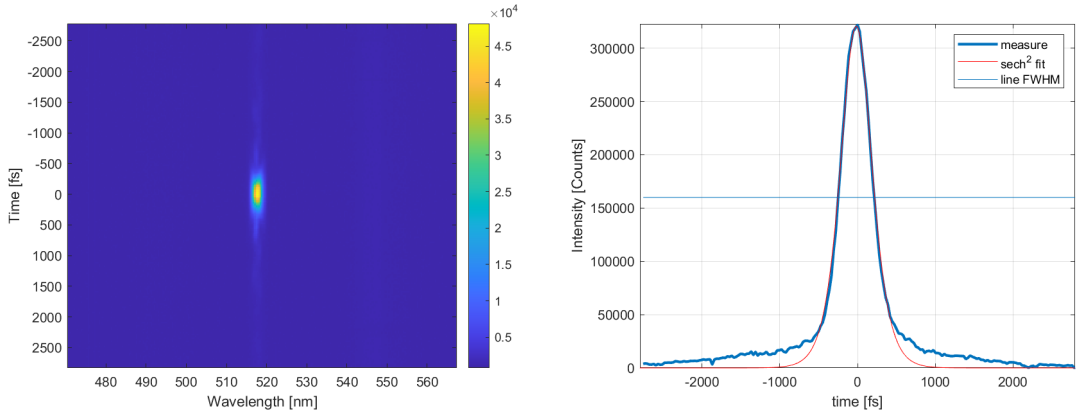

(a) Spectrogram of pump pulse before etalon.

(b) Intensity autocorrelation in time of pump pulse before etalon.

Figure 3.9: FROG characterization of pump pulse before the etalon: (a) Spectrogram of the SFG of the two replicas arising in the FROG set-up, Colorbar: intensity in arbitrary units. (b) Intensity autocorrelation in time, fitted with a sech^2 and highlighting the FWHM. The SFG was obtained focusing the beams on a 1 mm-thick BBO crystal.

As it can be seen in fig. 3.9a, the SFG is centered at $\simeq$ 517.5 nm, which corresponds to half of the fundamental wavelength. The measured pulse duration, assuming a sech^2 shape[3], is 288 fs. Therefore, before passing through the etalon, the pump pulse has a duration slightly longer than the initial one (268 fs), this difference is due to the passage through the HWP and the PBS, which introduce positive dispersion. Let us proceed with the pump pulse after the etalon.

[3]This will be assumed in all the FROG measurements shown. The link between the pulse duration Δt_{pulse} and the intensity autocorrelation FWHM $\Delta\tau_{CI}$ is: $\Delta\tau_{CI} = 1.55\Delta t_{pulse}$

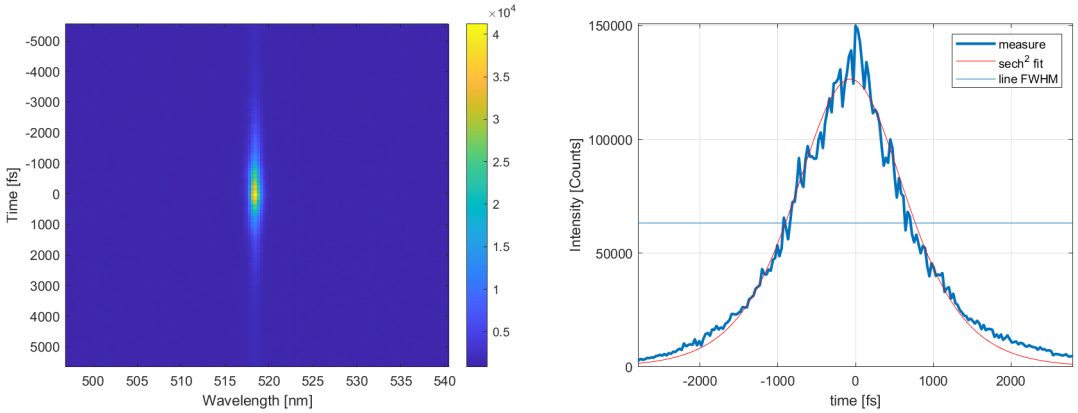

(a) Spectrogram of pump pulse after etalon.

(b) Intensity autocorrelation in time of pump pulse after etalon.

Figure 3.10: FROG characterization of pump pulse after the etalon: (a) Spectrogram of the SFG of the two replicas arising in the FROG set-up, Colorbar: intensity in arbitrary units. (b) Intensity autocorrelation in time, fitted with a sech^2 and highlighting the FWHM. The SFG was obtained focusing the beams on a 1 mm-thick BBO crystal.

In this case the pulse duration is equal to 1.06 ps. An increase of the time FWHM was expected, since, narrowing the spectrum, the temporal duration increases, as stated by the Fourier principle. The pulse spectrum after the etalon was measured with a spectrometer. The result is reported in fig. 3.11.

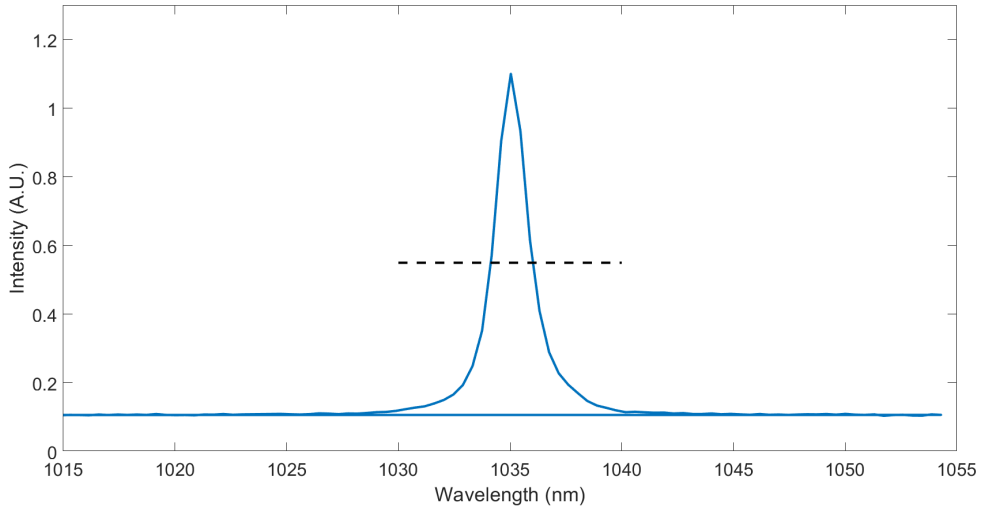

Figure 3.11: Pump pulse spectrum after the etalon. The dashed line highlights the half of the peak.

It can be observed that the bandwith of the pulse is narrow, namely, its FWHM is equal to 1.28 nm. With this bandwidth, a spectral resolution of ≈ 10 cm^{-1} can be reached.

3.2.3. Stokes pulse characterization

Let us proceed with the characterization of the Stokes pulse. In particular, the spectrum of the SC was measured with a spectrometer and a FROG analysis of the broadband pulse before and after compression was performed.

As we can see in fig. 3.12, in which the spectrum of the Stokes pulse is shown, Supercontinuum generation in YAG greatly broadens the bandwidth, reaching almost 1600 nm. The sharp decrease of intensity at 1050 nm is due to the presence of the LPF, employed to filter out the fundamental (when the LPF1200 is used, the sharp decrease results shifted to 1200 nm).

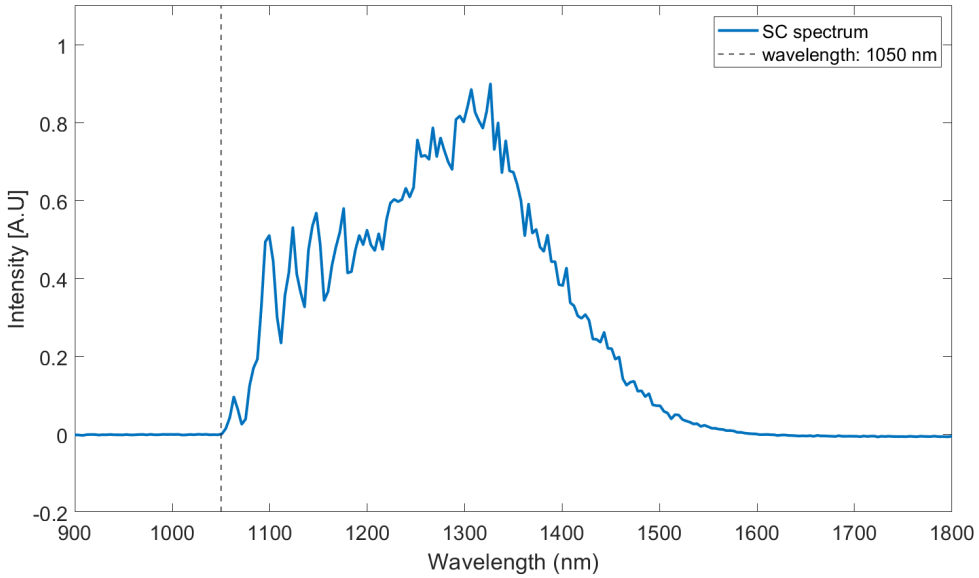

Figure 3.12: Stokes pulse spectrum after SC generation and LPF. The measurement is performed with a spectrometer (Avantes), with an integration time equal to 1 ms and averaging over 10000 spectra.

We can now move to the SHG-FROG analysis before compression, depicted in fig. 3.13.

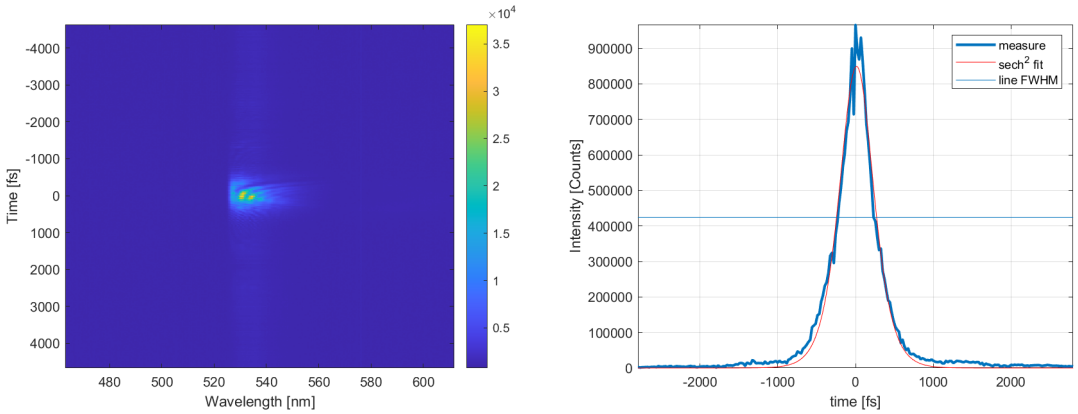

(a) Spectrogram of Stokes pulse before compression.

(b) Intensity autocorrelation in time of Stokes pulse before compression.

Figure 3.13: FROG characterization of Stokes pulse before compression: (a) Spectrogram of the SFG of the two replicas arising in the FROG set-up, Colorbar: intensity in arbitrary units. (b) Intensity autocorrelation in time, fitted with a sech^2 and highlighting the FWHM. The SFG was obtained focusing the beams on a 300 μm-thick BBO crystal. A thinner crystal, with respect to the pump pulse measurements, is needed to satisfy the phase matching condition for a broader bandwidth.

Before compression, the Stokes pulse duration reaches 315 fs and it is characterized by a positive GDD introduced by the propagation through several optical elements (two PBS, two HWP and the YAG crystal). The microscope objectives will introduce a further group delay dispersion, approximately 5000 fs^2. The overall positive GDD, considering all the optical elements in the beam path, is equal to 8000 fs^2 at the sample plane. Since the pulse spectrum is particularly broad, with a bandwidth $\simeq$ 500 nm, the Stokes pulse is particularly sensitive to GDD and would reach a FWHM in time of more than 3 ps without compression. Therefore, a compression is necessary.

It can be observed in the spectrogram shown in fig. 3.13a that $S(\lambda, \tau) \simeq 0$ for $\lambda < \lambda_{cut} =$ 525 nm, due to the presence of a LPF with a cut-off at $\lambda_{LPF} = 2\lambda_{cut} = 1050$ nm.

The goal of the compression is to add a negative GDD to compensate in advance for the dispersion introduced by the objectives and by the other optical elements, in order to reach GDD$\simeq$ 0 at the sample plane. In fig. 3.14, the FROG measurement of the Stokes pulse after compression is shown.

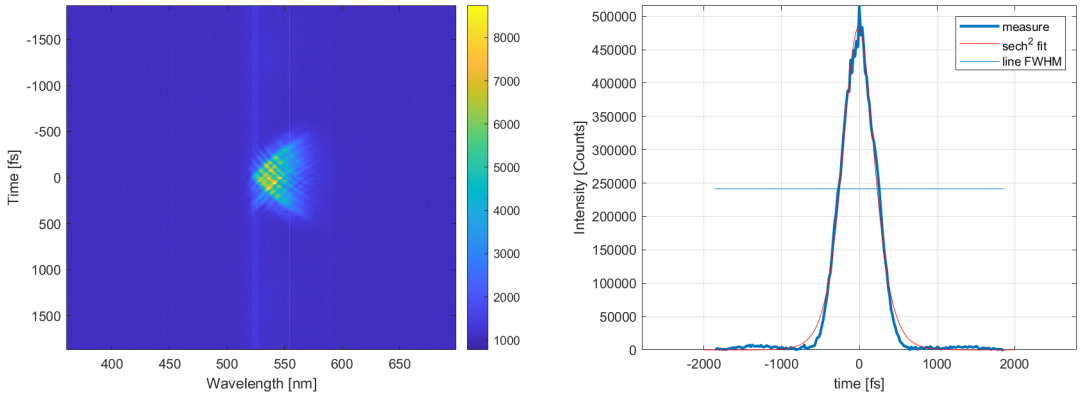

(a) Spectrogram of Stokes pulse after compression.

(b) Intensity autocorrelation in time of Stokes pulse after compression.

Figure 3.14: FROG characterization of Stokes pulse after compression: (a) Spectrogram of the SFG of the two replicas arising in the FROG set-up, Colorbar: intensity in normalized units. (b) Intensity autocorrelation in time, fitted with a sech^2 and highlighting the FWHM. The SFG was obtained focusing the beams on a 300 μm-thick BBO crystal.

The pulse duration after compression, and before the microscope, is 300 fs, which is similar to the one measured before compression. However, in this case the prism compressor introduced a negative GDD of -8000 fs^2, which is calculated plugging the prism material (SF-11) and the apex-to-apex distance (61 cm) in eq. (2.76). Therefore, the total GDD is negative before the microscope. In order to verify it, the same measurement has been repeated adding a piece of glass: this optical element adds a positive GDD simulating the one introduced in the microscope. We expect a strong decrease in the pulse duration, since the GDD gets close to zero. In fig. 3.15 this measurements is shown.

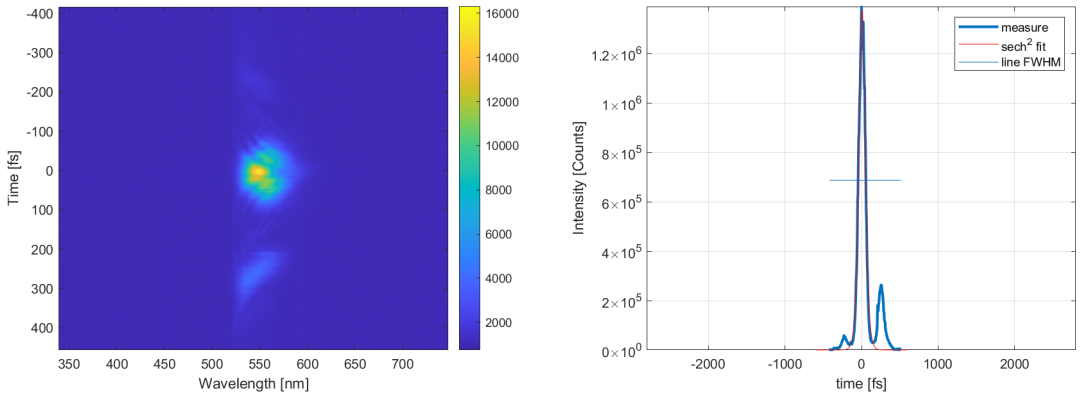

(a) Spectrogram of Stokes pulse after compression and propagation through glass.

(b) Intensity autocorrelation in time of Stokes pulse after compression and propagation through glass.

Figure 3.15: FROG characterization of Stokes pulse after compression and propagation through glass: (a) Spectrogram of the SFG of the two replicas arising in the FROG set-up, Colorbar: intensity in arbitrary units. (b) Intensity autocorrelation in time, fitted with a sech^2 and highlighting the FWHM. The SFG was obtained focusing the beams on a 300 μm-thick BBO crystal.

After propagating through a normally dispersive medium, the Stokes pulse results compressed in time, with a pulse duration of 57 fs. Thus, the hypothesis of negative GDD after the prism compressor is confirmed, and we expect a similar pulse duration at the sample plane. It can be observed that a pre-pulse and a post-pulse appear, respectively at the leading and trailing front of the pulse intensity autocorrelation, and they can be observed in the spectrogram as well, fig. 3.15a, for positive and negative times. The presence of these anomalies is due to the double reflection inside the piece of glass, which gives rise to a replica of the Stokes pulse, causing an unexpected SFG at positive and negative delays. Since the autocorrelation in non-collinear SHG-FROG should be symmetric with respect to the time delay, any asymmetry should be traced back to experimental inaccuracies.

3.3. Data processing

3.3.1. Noise reduction through singular value decomposition

Due to the high acquisition speed of data in CARS microscopy, the random noise floor could be problematic, especially for imaging applications. Furthermore, it could distort the lineshape of the peaks, reducing the effectiveness of NRB removal algorithms. Several methods allow the reduction of noise in a measured spectrum, such as moving-mean

techniques or Fourier transform based approaches. In this work we use singular value decomposition (SVD) since it can be applied directly to hyperspectral images, performing a simultaneous denoising of all the spectra contained in the data matrix. Starting from an acquired image, characterized by spatial dimensions $n \times m$ and by s spectral components, the first step is a reshaping of the data set, in order to have a bidimensional matrix $\boldsymbol{A}$ with s rows and $l = n \times m$ columns. Afterwards, SVD is applied to the matrix, which is rewritten as:

$$\boldsymbol{A} = \boldsymbol{U}\boldsymbol{S}\boldsymbol{V}^H, \tag{3.9}$$

A schematic representation of (3.9) is reported in fig. 3.16.

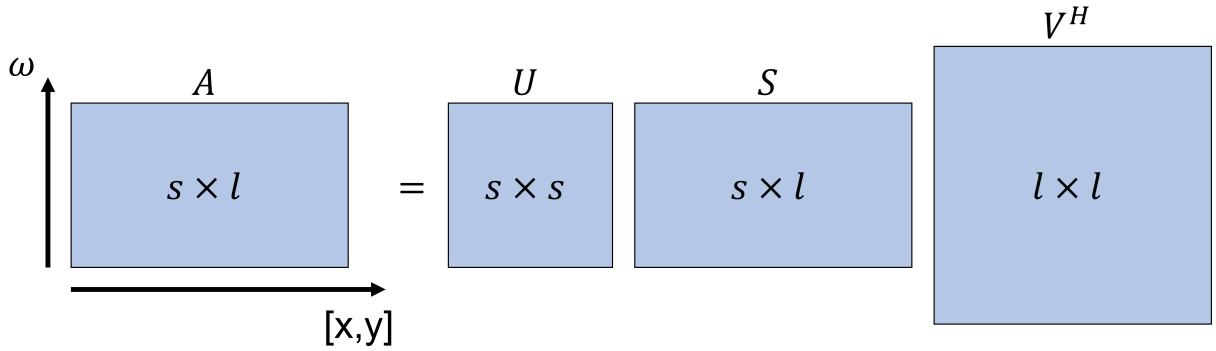

Figure 3.16: Schematic representation of SVD decomposition.

In which the H-superscript indicates the Hermitian transpose; $\boldsymbol{U}$ and $\boldsymbol{V}$ are unitary matrices whose columns are the left and right singular vectors, respectively. In particular, $\boldsymbol{U}$ is an $s \times s$ matrix and is composed of spectral basis vectors, while, $\boldsymbol{V}$ is a $l \times l$ unitary matrix and is composed of spatial basis vectors. $\boldsymbol{S}$ is a $s \times l$ rectangular diagonal matrix whose entries are non-negative real numbers, known as singular values, denominated λ_i, where the subscript i indicates the row (or the column) of the singular value. Moreover, since the initial matrix $\boldsymbol{A}$ is real, the Hermitian transpose of $\boldsymbol{V}$ is equal to the transpose $\boldsymbol{V}^T$. The SVD decomposition can be thought as a decomposition of the $\boldsymbol{A}$ matrix in a weighted, ordered sum of contributes, each represented by λ_i. The first singular values represent the highly spatio-spectral coherent contribute, while, increasing the order i, the lower coherent parts can be found. From the spectral point of view, the lower i-s give the low-frequency terms, while the higher ones correspond to the high-frequency contributions. Therefore, setting to zero all the singular values over a certain i, we remove the singular vector with the least spatio-spectral coherence. Since the noise is characterized by a complete randomness in space and by a high-frequency in spectra, removing the λ_i with high i, we are effectively denoising the data [80]. After having set to zero all the λ_i, for

$i > i_{filter}$, changing the matrix $\boldsymbol{S}$ to $\boldsymbol{S_{filtered}}$, the denoised matrix $\boldsymbol{A_{denoised}}$ can be found as:

$$\boldsymbol{A_{denoised}} = \boldsymbol{U}\boldsymbol{S_{filtered}}\boldsymbol{V}^T. \tag{3.10}$$

3.3.2. NRB removal algorithms

In section 2.3.7 the resonant and non-resonant contributions to the CARS signal have been analyzed. For spectroscopic applications, only the resonant one is meaningful, thus, the NRB should be removed in order to obtain a vibrational spectrum, characterized by Lorentzian peaks. Several physical techniques could be implemented in order to remove the NRB before acquisition, such as Time-resolved CARS [81] or Box-CARS [82]. However, the NRB actually amplifies the weak Raman signal, enabling high-sensitivity detection, thus, its physical removal leads to weaker signals, lower SNRs, and greater experimental complexity. Therefore, numerical methods aiming at removing the non-resonant part after acquisition have been developed. These methods can be divided in two main classes: the ones based on the maximization of entropy (Maximum Entropy method: MEM) [83] and the ones relying on phase retrieval through Kramers-Kronig (KK) relations [84].

In section 2.3.6 it has been shown that the CARS intensity depends directly on the modulus squared of the third-order non-linear susceptibility $\chi^{(3)}$. In (2.159c), the relation has been developed finding that:

$$I_{AS} \propto \left|\chi_R^{(3)}\right|^2 + \left|\chi_{NR}^{(3)}\right|^2 + 2\chi_{NR}^{(3)} Re\left\{\chi_R^{(3)}\right\}, \tag{3.11}$$

The relevant spectral information are contained in the first term of the right-hand side of (3.11). It is also known that the resonant susceptibility $\chi_R^{(3)}$ is a complex number, where the real part presents a dispersive shape, while the imaginary part presents a Lorentzian shape. On the other hand, the non-resonant susceptibility $\chi_{NR}^{(3)}$ is real if far from electronic resonances. It could be demonstrated that knowing the phase $\varphi(\omega)$ of $\chi^{(3)}$ allows to get the same spectral information embedded in $\left|\chi_R^{(3)}\right|^2$. Therefore, both MEM and KK methods aim at retrieving the phase of $\chi^{(3)}$.

Let us proceed with the description of the Maximum Entropy method. The MEM hypothesis states that any inferences made from incomplete data should be consistent with maximized entropy of the associated probability distribution, given the constraints of the known information. This hypothesis can be applied to compute a power spectrum $S(\nu)$

associated with discrete measured data [83]. This could be applied to model the CARS lineshape as:

$$S(\nu) = \left| \frac{\beta}{1 + \sum_{k=1}^{M} a_k \exp(-2\pi i k \nu)} \right|^2 \equiv \left| \frac{\beta}{A_M(\nu)} \right| \tag{3.12}$$

Where, in (3.12), ν is the frequency, normalized to run from 0 to 1 over the experimental range, A and β are complex coefficients, and M is the number of correlation coefficients used in reconstructing the spectrum. M can be as high as the number of spectral points (N); however, the higher order coefficients represent primarily noise, so that typically $M \leq N/2$ is used. The coefficients a_k and β can be found solving the Toeliptz equation (3.13):

$$\begin{bmatrix} C_0 & C_1^* & \cdots & C_M^* \\ C_1 & C_0 & \cdots & C_{M-1}^* \\ \vdots & \vdots & \ddots & \vdots \\ C_M & C_{M-1} & \dots C_0 & \end{bmatrix} \begin{bmatrix} 1 \\ a_1 \\ \vdots \\ a_M \end{bmatrix} = \begin{bmatrix} |\beta|^2 \\ 0 \\ \vdots \\ 0 \end{bmatrix} \tag{3.13}$$

Where $*$ denotes the complex conjugate and C_k are the discrete Fourier transform of the CARS spectrum at a discrete set of normalized frequencies $\nu_n = n/N$, with $n = 0, 1, \ldots, N$, calculated as:

$$C_k = N^{-1} \sum_{n=0}^{N-1} S(\nu_n) exp(2\pi i k \nu_n), \tag{3.14}$$

Substituting the values of the coefficients a_k and β (which are found solving (3.13), taking (3.14) into account) in eq. (3.12), it is possible to find $A_M(\nu)$, from which the spectral phase ϕ_{CARS} can be retrieved as:

$$\phi_{CARS}(\nu) = arg[A_M(\nu)], \tag{3.15}$$

This result is obtained directly from the measured spectrum, however, in (3.15), the NRB contribution has not been taken into account yet. Indeed, the measured spectral phase can be written as:

$$\phi_{CARS}(\nu) = \varphi_{vib}(\nu) + \psi_{nrb}(\nu), \tag{3.16}$$

Where, in (3.16), $\varphi_{vib}(\nu)$ contains the vibrational spectrum information, while $\psi_{nrb}(\nu)$ is introduced by the presence of NRB. The NRB phase term can be calculated applying the

same procedure to a reference spectrum acquired from models materials, such as coverslip glass. Eventual reference deviations from the actual NRB are assumed to contribute to a slowly varying baseline that can be subtracted.

Let us move to the phase retrieval method exploiting Kramers-Kronig (KK) relations. According to the KK connection, a function, $f(\omega)$, has an explicit, causal relationship between its real and imaginary components. As a result, if just the real (or imaginary) component is known, the imaginary (or real) component can be determined. In CARS spectroscopy, neither the real nor the imaginary part of $\chi^{(3)}$ is directly accessible. However, there is an explicit connection between the complex norm of the function and the phase if the function is square integrable [84]:

$$ln\left(|f(\omega)|\right) = -\tilde{\mathcal{H}}\left\{\phi\right\}, \tag{3.17}$$

$$\phi = \tilde{\mathcal{H}}\left\{ln\left(|f(\omega)|\right)\right\}, \tag{3.18}$$

In which $\tilde{\mathcal{H}}$ is the Hilbert transform. In order to calculate it, the complex modulus of the function or its phase over an infinite frequency range should be known. However, since only a portion of the spectrum can be effectively measured, a windowed version of the Hilbert transform, $\tilde{\mathcal{H}_w}$, is exploited. $\tilde{\mathcal{H}_w}$ is defined as:

$$\tilde{\mathcal{H}_w}\left\{f(x);\omega_a,\omega_b\right\} = \frac{\mathcal{P}}{\pi}\int_{\omega_a}^{\omega_b}\frac{f(x')}{x-x'}dx', \tag{3.19}$$

Where ω_a and ω_b are the limits of the covered spectral range. $\mathcal{P}$ is the Cauchy principal value.

As long as two conditions are met:

1. The Raman peaks contained within this window are not impacted by those outside of the window
2. Any electronic resonances, encompassed in the non-resonant susceptibility $\chi^{(3)}_{NR}$, are far from the resonant ones (as it is normally the case with infrared stimulation),

the Hilbert transform is related to its windowed version (3.19) by the relation:

$$\tilde{\mathcal{H}_w}\left\{\frac{1}{2}ln\left|\chi^{(3)}\right|^2\right\} \simeq \tilde{\mathcal{H}}\left\{\frac{1}{2}ln\left|\chi^{(3)}\right|^2\right\} + \epsilon(\omega), \tag{3.20}$$

where $\epsilon(\omega)$ is an additive error term. Let us consider the CARS signal intensity, I_{CARS}. In section 2.3.6 we wrote it in terms of the pump and Stokes intensities, however, it could also be written in term of electric fields as:

$$I_{CARS}(\omega) = \left|\left\{[E_S(\omega) \otimes E_P(\omega)]\,\chi^{(3)}(\omega)\right\} * E_P(\omega)\right|^2 \equiv |\tilde{C_{st}}|^2|\tilde{\chi}^{(3)}|^2, \tag{3.21}$$

Where, in (3.21), $\otimes$ and $*$ are the cross-correlation and the convolution operators respectively. The correlation between pump and probe fields can be defined as $C_{st} = [E_S(\omega) \otimes E_P(\omega)]$, and is called the coherent stimulation profile. Assuming a spectrally narrow pump, an effective stimulation profile $\tilde{C_{st}}$ and an effective non-linear susceptibility can be introduced as:

$$\tilde{C_{st}}(\omega) \equiv \frac{[C_{st}(\omega) * E_P(\omega)]}{\int E_P(\omega)d\omega}, \tag{3.22}$$

$$\tilde{\chi}^{(3)}(\omega) \equiv \chi^{(3)}(\omega) * E_P(\omega), \tag{3.23}$$

Therefore, performing the windowed Hilbert transform (3.19) of the logarithm of the CARS signal intensity (3.21), taking into account (3.20) and applying the property (3.18), we find:

$$\phi_{CARS} = \tilde{\mathcal{H}_w}\left\{\frac{1}{2}ln\left(I_{CARS}(\omega)\right)\right\} \simeq \epsilon(\omega) + \tilde{\mathcal{H}_w}\left\{\frac{1}{2}ln\left|\tilde{C_{st}}(\omega)\right|^2\right\} + \tilde{\mathcal{H}}\left\{\frac{1}{2}ln\left|\tilde{\chi}^{(3)}(\omega)\right|^2\right\}, \tag{3.24}$$

Applying again the Hilbert transform property (3.18) to (3.24), we find:

$$\phi_{CARS} \simeq \epsilon(\omega) + \tilde{\mathcal{H}_w}\left\{\frac{1}{2}ln\left|\tilde{C_{st}}(\omega)\right|^2\right\} + arg\left[\chi_R^{(3)} + \chi_{NR}^{(3)}\right], \tag{3.25}$$

Where the arg operator extracts the phase. The measured phase contains several contributes: the error ϵ, due to the use of the windowed version of the Hilbert transform, the contribution from the effective stimulation profile, and from both the resonant and non-resonant parts of the susceptibility. If it was possible to measure the NRB intensity I_{NRB}, we could apply the windowed Hilbert transform to the ratio I_{CARS}/I_{NRB}, obtaining:

$$\phi_{CARS/NRB} = \tilde{\mathcal{H}_w}\left\{\frac{1}{2}ln\left(\frac{I_{CARS}(\omega)}{I_{NRB}(\omega)}\right)\right\} \simeq \epsilon(\omega) + \tilde{\mathcal{H}_w}\left\{\frac{1}{2}ln\left|\tilde{C_{st}}(\omega)\right|^2\right\} + \\ - \left[\epsilon(\omega) + \tilde{\mathcal{H}_w}\left\{\frac{1}{2}ln\left|\tilde{C_{st}}(\omega)\right|^2\right\}\right] + arg\left[\chi_R^{(3)} + \chi_{NR}^{(3)}\right] - arg\left[\chi_{NR}^{(3)}\right] \simeq \\ arg\left[\chi_R^{(3)} + \chi_{NR}^{(3)}\right], \tag{3.26}$$

Where in the last passage of (3.26) we implicitly assumed that, since we are generally far from electronic resonances, $\chi_{NR}^{(3)}$ is real. Using the ratio of the CARS and NRB intensities as our signal, the complex spectrum can be written as:

$$I_{CARS/NRB} = \sqrt{\frac{I_{CARS}(\omega)}{I_{NRB}(\omega)}}\exp i\phi_{CARS/NRB} \simeq \frac{|\tilde{\chi}^{(3)}|}{|\tilde{\chi}_{NR}^{(3)}|}\exp iarg\left[\chi_R^{(3)} + \chi_{NR}^{(3)}\right], \tag{3.27}$$

The Raman-like spectrum can be extracted as the imaginary part of $I_{CARS/NRB}$ in (3.27):

$$Im\left\{I_{CARS/NRB}\right\} = \frac{Im\left\{\chi_R^{(3)}(\omega)\right\}}{\left|\chi_{NR}^{(3)}\right|}, \tag{3.28}$$

Where the imaginary part of the third-order non-linear susceptibility contains the information regarding the vibrational spectrum. Therefore, the retrieved spectrum is directly proportional to the spontaneous Raman one, scaled by the non-resonant component.

The described method relies on a precise measurement of the non-resonant background. However, up to now, no approach has been found to measure the non-resonant contribution alone. Typically, the CARS signal coming from a material without Raman signature, such as glass or water, is used as a reference. However, this leads to a multiplicative complex error which should be taken into account.

Let us consider the reference measurement, I_{ref}, instead of I_{NRB}, which are linked by the multiplicative relation: $I_{ref}(\omega) = \xi(\omega)I_{NRB}(\omega)$, where ξ is assumed to be real and positive.

Let us calculate the phase of the ratio I_{CARS}/I_{ref}, similarly to what we did in eq. (3.26):

$$\phi_{CARS/ref} = \tilde{\mathcal{H}_w}\left\{\frac{1}{2}\ln\left(\frac{I_{CARS}(\omega)}{\xi(\omega)I_{NRB}(\omega)}\right)\right\} \simeq \phi_{CARS/NRB} + \underbrace{\tilde{\mathcal{H}_w}\left\{\frac{1}{2}\ln\left(\frac{1}{\xi(\omega)}\right)\right\}}_{\phi_{err}}, \tag{3.29}$$

As we did in (3.27), we can calculate the imaginary part of the spectrum obtained as the ratio $I_{CARS/ref} = I_{CARS}/I_{ref}$, where we use I_{ref} instead of I_{NRB}:

$$Im\left\{I_{CARS/ref}\right\} = \underbrace{\sqrt{\frac{1}{\xi(\omega)}}}_{A_{err}(\omega)} \sqrt{\frac{I_{CARS}(\omega)}{I_{NRB}(\omega)}} \sin\left[\phi_{CARS/NRB} + \phi_{err}\right] \tag{3.30}$$

From eq. (3.29) and eq. (3.30), it can be seen that using a reference instead of the real NRB leads to an amplitude (A_{err}) and a phase (ϕ_{err}) error. A_{err} and ϕ_{err} are linked by the relationship:

$$\begin{aligned} \ln A_{err}(\omega) &= -\tilde{\mathcal{H}}\left\{\phi_{err}(\omega)\right\}, \\ \phi_{err}(\omega) &= \tilde{\mathcal{H}}\left\{\ln A_{err}(\omega)\right\}, \end{aligned} \tag{3.31}$$

Where the Hilbert transform property (3.18) has been used. However, since the Hilbert transform of a constant is equal to zero, there is an ambiguity in eq. (3.31). In particular, if $\xi(\omega)$ is multiplied by a constant α, the phase error remains the same:

$$\phi_{err}(\omega) = \tilde{\mathcal{H}}\left\{\ln\frac{1}{\alpha\xi(\omega)}\right\} = \tilde{\mathcal{H}}\left\{\ln\frac{1}{\xi(\omega)}\right\}. \tag{3.32}$$

The phase and amplitude distortions can be solved following two main steps:

1. Remove phase error via detrending $\phi_{CARS/ref}$ and correct part of the amplitude error exploiting the relationship in (3.31),
2. Correct for scaling errors, related to the constant α, and for the use of the windowed version of the Hilbert transform in step 1, leading to ϵ_{err}. The second step is performed via unity centering of the phase corrected spectrum [84].

Let us begin with the first step. The phase $\phi_{CARS/ref}(\omega)$ is qualitatively similar to a Raman-like spectrum, since peaks extend positively over a baseline. However, the slowly-varying phase error ϕ_{err} causes a slowly-varying deviation from the zero baseline. Therefore, isolating the erroneous baseline allows to find ϕ_{err}. Using traditional baseline detrending methods, $\phi_{err}(\omega)$ can be extracted from $\phi_{CARS/ref}(\omega)$ and removed. Moreover, using eq. (3.31), part of the amplitude error can be corrected. The two corrections can be implemented multiplying the retrieved spectrum $I_{CARS/ref}$ by a complex phase-correction multiplier. The phase corrected spectrum I_{pc} reads as:

$$I_{pc} = I_{CARS/ref}\left\{\frac{1}{\exp\left[-\tilde{\mathcal{H}}_w\left\{\phi_{err}(\omega)\right\}\right]}\exp\left[-i\phi_{err}(\omega)\right]\right\} = \\ = \sqrt{\frac{I_{CARS}(\omega)}{I_{ref}(\omega)}}\exp i\phi_{CARS/ref}\left\{\frac{1}{\exp\left[-\tilde{\mathcal{H}}_w\left\{\phi_{err}(\omega)\right\}\right]}\exp\left[-i\phi_{err}(\omega)\right]\right\}, \tag{3.33}$$

Let us proceed implementing the second step. In eq. (3.32) we saw that retrieving A_{err} from ϕ_{err} leads to an ambiguity related to the scaling constant α. Furthermore, in eq. (3.33), $\tilde{\mathcal{H}}_w$ was used instead of $\tilde{\mathcal{H}}$, causing a window-effect error $\epsilon_{err}(\omega)$:

$$\tilde{\mathcal{H}}\left\{\phi_{err}(\omega)\right\} = \tilde{\mathcal{H}}_w\left\{\phi_{err}(\omega)\right\} + \epsilon_{err}(\omega), \tag{3.34}$$

To finalize the error correction, one needs to account for the A_{err} ambiguity and $\epsilon(\omega)$. Both of these variables can be found by examining the real component of the phase-corrected spectrum in eq. (3.33). Since the real component of eq. (3.27) is unity centered, which means that $\left\langle |\tilde{\chi}^{(3)}|/|\tilde{\chi}^{(3)}_{NR}|\cos\phi_{CARS/NRB}\right\rangle = 1$, any alteration of the mean of the real component in eq. (3.33) is caused by the presence of the scaling constant α, thus, one could measure this mean and normalize I_{pc} by this value. Nevertheless, ϵ_{err} might give this mean a frequency-dependent component. Using numerical means, though, one can find a slowly varying centerline and normalize the phase-corrected spectrum, thus removing α and ϵ_{err} in one step. Finally, a rescaled, phase-corrected, complex spectrum $I_{pc,sc}$ may be calculated as:

$$I_{pc,sc} = \frac{I_{pc}(\omega)}{\langle Re\left\{I_{pc}(\omega)\right\}\rangle(\omega)} = \frac{|\tilde{\chi}^{(3)}|}{|\tilde{\chi}^{(3)}_{NR}|}\exp i\phi_{CARS/NRB}, \tag{3.35}$$

Comparing eq. (3.35) with eq. (3.27) it can be seen how the NRB can be removed from the CARS signal even using a reference measurement of the non-resonant background in the Kramers-Kronig relations [84].

In conclusion, it has been proven how, starting from a measured CARS signal, it is possible to retrieve the vibrational Raman-like spectrum, removing the NRB through phase retrieval, exploiting two possible methods, namely the Maximum Entropuy method and the Kramers-Kronig relations.

3.3.3. Multivariate curve resolution

In section 3.1 we described the experimental set-up and how it is capable of providing hyperspectral images. A great advantage of this kind of images is that they allow to distinguish different chemical species thanks to different features in their vibrational spectrum. However, the Raman peaks are often overlapped, especially in biological sample, hence visualizing the image at a specific Raman shift is usually not enough to get a satisfactory contrast between different chemical species. Several methods have been developed to exploit the spectral information in order to provide chemical maps. We can divide them into two groups: unsupervised and supervised methods, based on their key distinctions. For unsupervised algorithms, no prior knowledge about the pure components is needed. Therefore, to find the separate spectral components, the program initially uses data mining. Contrarily, supervised approaches require the spectrum profiles of pure components or a portion of the chemical concentration maps, which makes the data processing a linear fitting or segmentation problem in order to produce chemical maps.

Unsupervised methods allow to study unknown samples, since no knowledge a priori is needed to perform the analysis. This feature makes them suitable for diagnostic purposes. Among the unsupervised methods, MCR has been proven to show the best results [85] and it was used in this work. MCR is a nonnegative matrix factorization (NMF) algorithm aiming to decompose a hyperspectral image into chemical concentration maps. It can be applied to both raw CARS data or to data-set where the NRB was removed. We can define the initial hyperspectral image as a $n \times m \times s$ matrix, where n and n correspond to the spatial dimensions x and y, while s is the spectral dimension. MCR assumes that the spectral data are a linear combination of k pure components with nonnegative concentrations, thus, the initial matrix can be expressed as:

$$D = CS^T + w, \tag{3.36}$$

Where $D \in R^{n \cdot m \times S}$ is the raster-transformed 2D data matrix of the initial hyperspectral images, $C \in R^{n \cdot m \times k}$ contains the concentration map of the pure components, $S \in R^{k \times s}$ represents the spectral profiles of the components and w is related to the noise in measurements. MCR aims at finding the concentration and spectral matrices C and S solving the inverse problem in eq. (3.36). Matrices C and S can be found exploiting an Alternating Least Square (ALS) algorithm. ALS solves the inverse problem alternating two steps:

1. Fixes S and finds the optimal C,
2. Fixes C and finds the optimal S,

The optimization is performed iteratively minimizing the Frobenious norm $\|D - CS^T\|^2$ under the non-negative constraints $C \geq 0$ and $S \geq 0$. As a result, neither the calculated abundance maps nor the resultant spectra may have negative values. The convergence criterion used is that the change in percentage of standard deviation of residuals between two successive iterative cycles reaches the predefined constraint value, often set at 0.1 %. Compared to other factorization techniques, MCR analysis has the benefit that the results can be meaningfully interpreted as nonnegative abundance maps and spectral intensities [85].

3.4. Experimental results

3.4.1. Broadband CARS on solvents

In this subsection the experimental result of Broadband CARS on solvents are shown. The samples were sandwidched between two 170 μm glass coverslips. The set-up described in section 3.1 allows us to obtain broadband two-color and three-color CARS spectra (depending on the filter used on the Stokes pulse and on the compression introduced by the prism compressor) covering a wide wavelength range (780-992 nm), which corresponds to the interval in wavenumbers 470-3330 cm^{-1}. When the LPF at 1050 nm is used, two and three-color CARS signals overlap. In this case, we reduced the time compression through the prisms compressor, increasing the time duration of the Stokes pulse. Thus, since different colors arrive at different times, we prevent intra-pulse excitation, exciting only the two-color signal.

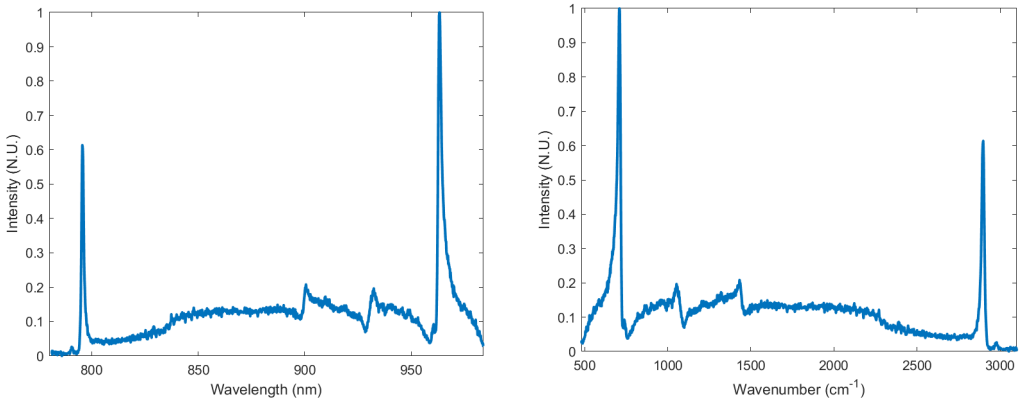

(a) Two-color B-CARS raw data from DMSO in wavelengths.

(b) Two-color B-CARS raw data from DMSO in wavenumbers.

Figure 3.17: Raw Two-color B-CARS data from DMSO acquired with a pixel dwell time of 0.8 ms, 1250 spectra-per-second. The data are shown in (a) wavelength and (b) wavenumbers.

In fig. 3.17 the raw data of two-color B-CARS on DMSO are shown. The spectrum is converted in wavenumbers by means of the relation (2.131). Afterwards, the non-resonant background is removed from the B-CARS spectra through phase retrieval exploiting the Kramers-Kronig method described in section 3.3.2. Since it is not possible to acquire the real NRB, a reference measurement is performed on a glass coverslip. The result of such measurement is shown in fig. 3.18a.

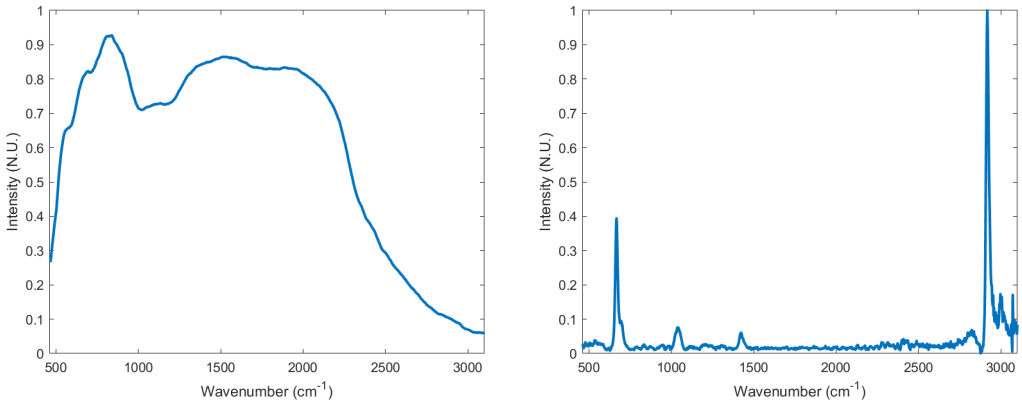

(a) Reference NRB.

(b) B-CARS data from DMSO after NRB removal.

Figure 3.18: (a) Non-resonant background reference signal from a glass coverslip, averaged over 10000 acquisitions. (b) CARS spectrum of DMSO after NRB removal. Pixel dwell time: 0.8 ms, Spectra per second: 1250.

As we can see in fig. 3.18, after the NRB removal, the spectrum is constituted of a series of Lorentzian peaks over a zero-baseline. Since the KK method for phase retrieval is based on the ratio between the CARS and NRB intensities, when the NRB signal gets close to zero, the retrieved CARS spectrum in such region can not be considered meaningful, since all the fluctuations are enhanced. Therefore, is usually necessary to cut part of the final spectra to have only significant results. In fig. 3.19, the two-color CARS spectra before and after NRB removal of DMSO, Toluene, Ethanol, Methanol, Isopropanol and Acetone are shown. Moreover, in order to validate the results, a comparison with Sponaneous Raman (SR) spectra[4] has been also performed.

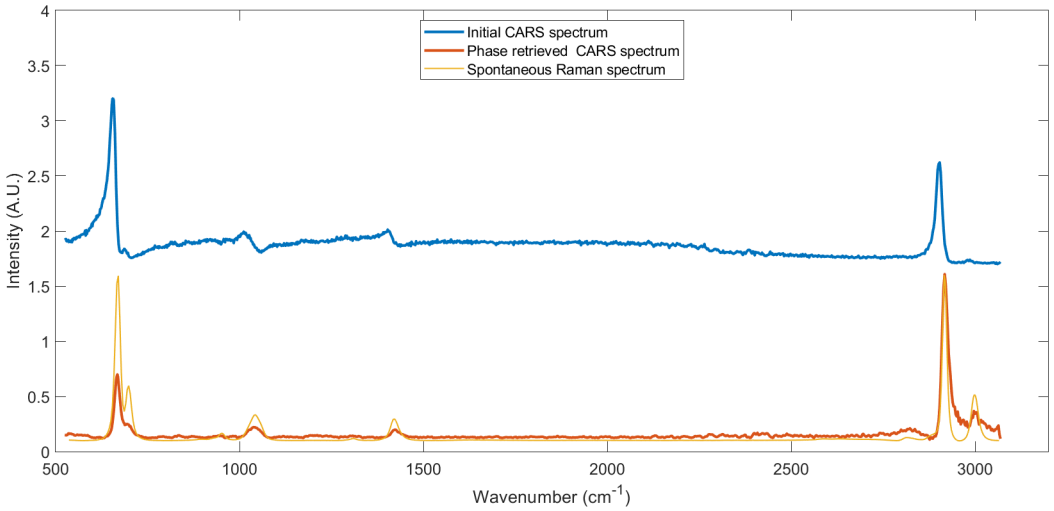

(a) Two-color B-CARS before and after NRB removal and SR spectra from DMSO.

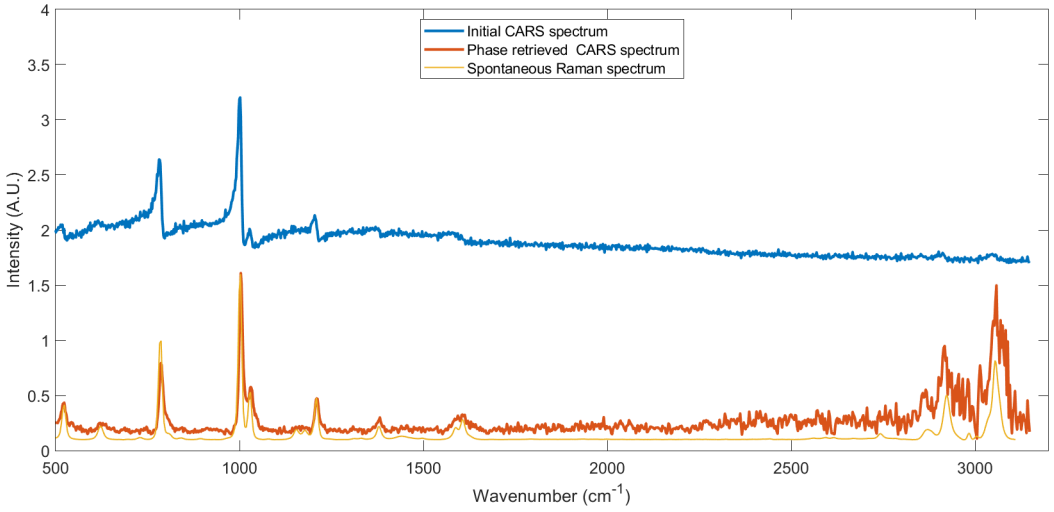

(b) Two-color B-CARS before and after NRB removal and SR spectra from Toluene.

[4]SR spectra are measured with a home-built set-up, presented in appendix B.1, with an integration time of 5 s. Moreover, an average over five measurements is performed, in order to increase the SNR.

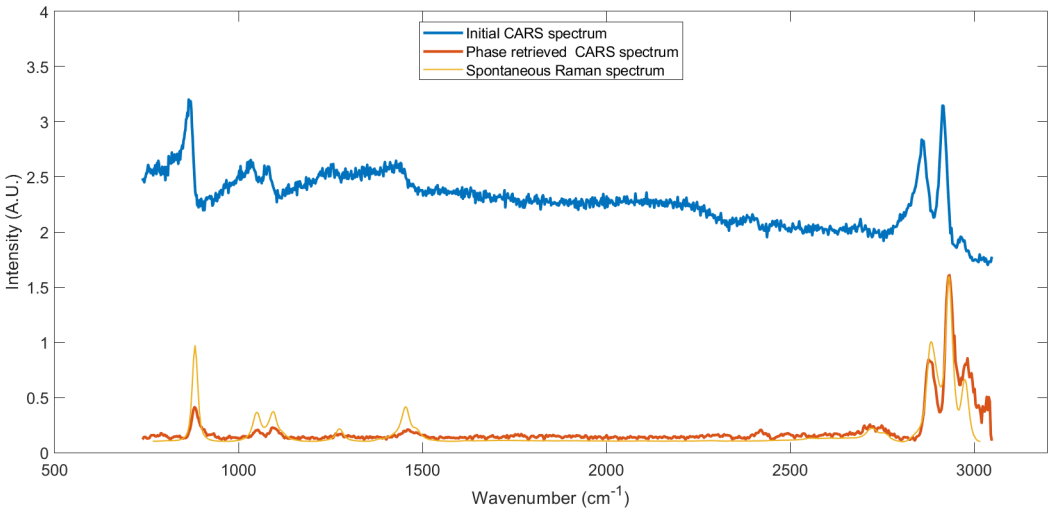

(c) Two-color B-CARS before and after NRB removal and SR spectra from Ethanol.

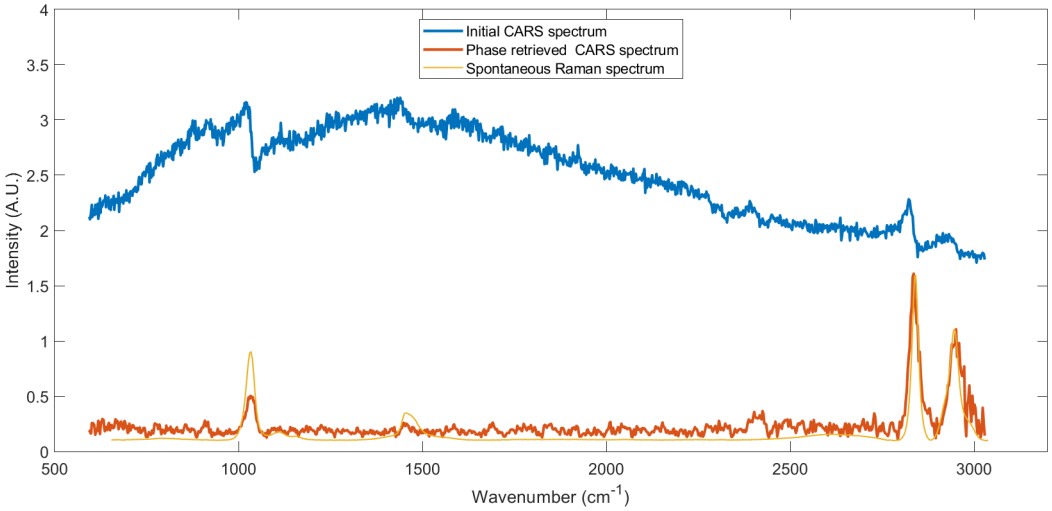

(d) Two-color B-CARS before and after NRB removal and SR spectra from Methanol.

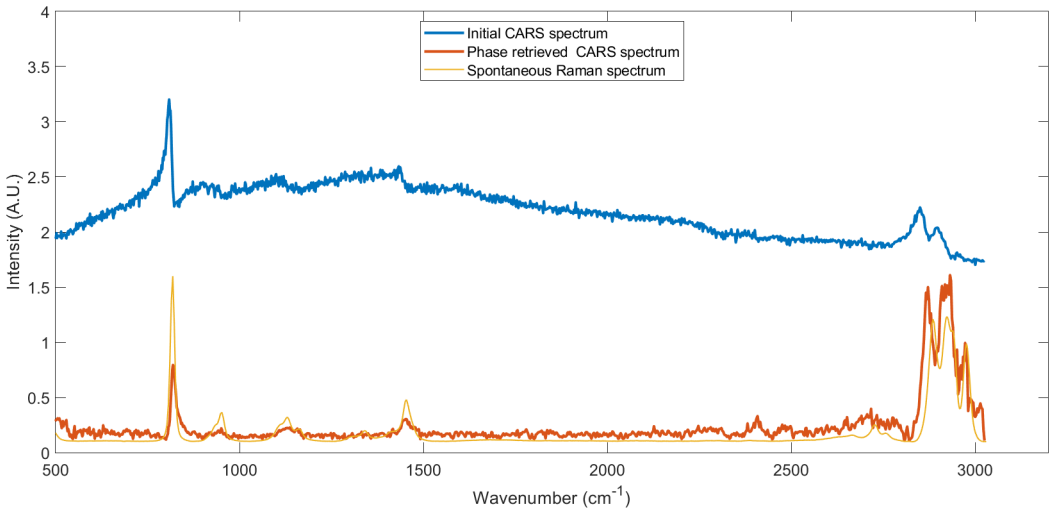

(e) Two-color B-CARS before and after NRB removal and SR spectra from Isopropanol.

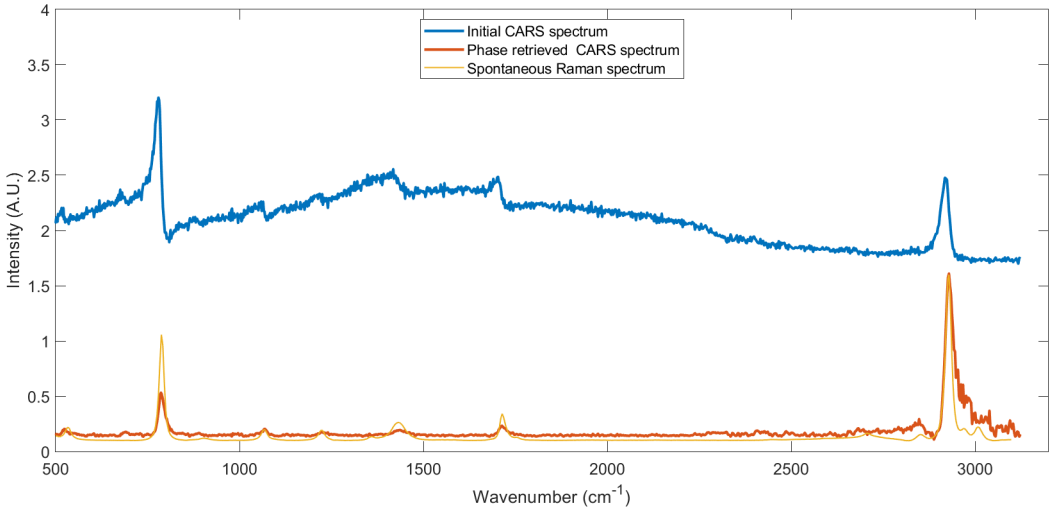

(f) Two-color B-CARS before and after NRB removal and SR spectra from Acetone.

Figure 3.19: Two-color B-CARS spectra of solvents before and after non-resonant background removal through phase retrieval and comparison with SR spectra. The spectra acquired are respectively from: (a) DMSO; (b) Toluene; (c) Ethanol; (d) Methanol; (e) Isopropanol; (f) Acetone. Integration time: 0.8 ms, Spectra per second: 1250.

The spectra were acquired setting the CCD exposure time at 0.8 ms, which is the minimum allowed by the detector electronics. The raw spectra (blue lines in fig. 3.19) show the characteristic distortion of the lineshape due to the interference between resonant and non-resonant contributions. After the NRB removal, the spectra (red lines in fig. 3.19) show a great accordance with SR spectra both in spectral position of the peaks and relative amplitude. In this case, no denoising methods were applied. All the solvents

show peaks in both the fingerprint and the C-H stretching regions. It can be observed a great accordance with the SR spectra, proving that our set-up is capable of performing reliable spectroscopies.

The same measurements were repeated increasing the time-compression of the Stokes pulse, reaching 57 fs duration at the sample plane, and changing the LPF filtering out the Stokes spectrum, in particular, the wavelength of the LPF was moved from 1050 to 1200 nm. In this way, the minimum Raman shift which can be excited through two-color CARS can be calculated as:

$$RS_{min} = \lambda_P^{-1} - \lambda_{S,min}^{-1}, \tag{3.37}$$

Since the minimum lambda in the Stokes pulse, due to the presence of LPF1200, is equal to 1200 nm, eq. (3.37) gives $RS_{min} = 1329\ \mathrm{cm}^{-1}$. Therefore, below $1329\ \mathrm{cm}^{-1}$, the signal is given by three-color CARS. The spectra with the contribution of both two and three-color CARS are shown in fig. 3.20 and fig. 3.21.

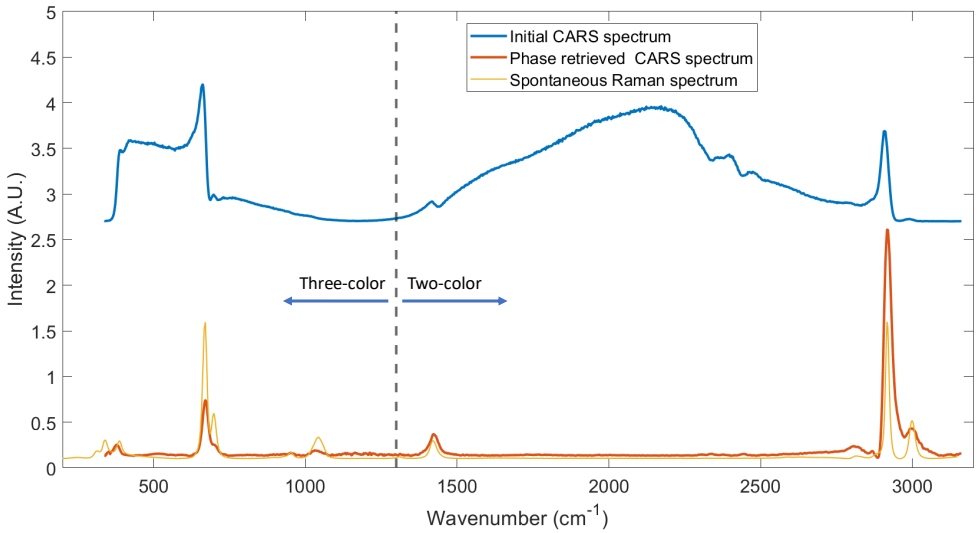

Figure 3.20: Two and three-color B-CARS spectra before and after NRB removal and spontaneous spectrum of DMSO. Dashed line: $1329\ \mathrm{cm}^{-1}$. Integration time: 1.2 ms, Spectra per second: 833

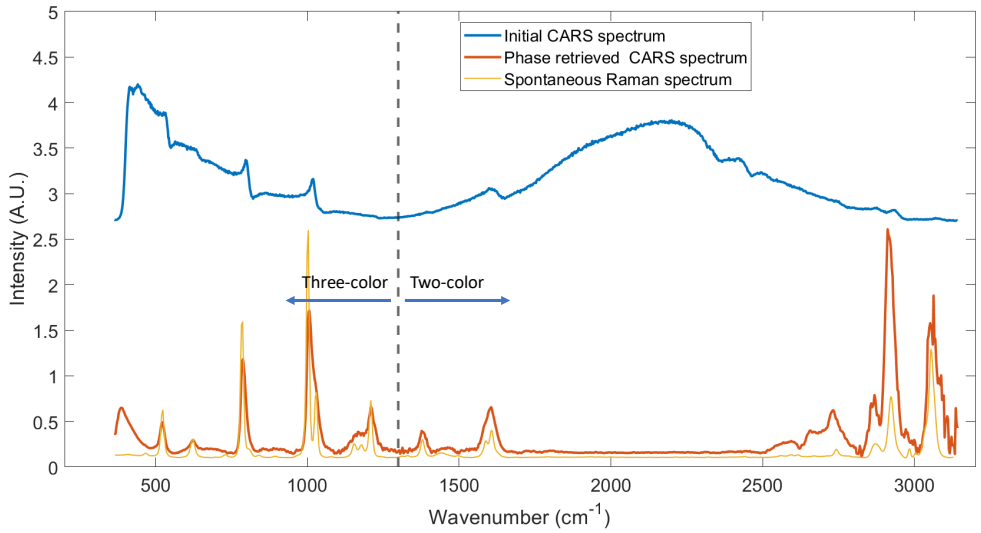

Figure 3.21: Two and three-color B-CARS spectra before and after NRB removal and spontaneous spectrum of Toluene. Dashed line: 1329 cm^{-1}. Integration time: 1.2 ms, Spectra per second: 833.

It can be seen that the raw CARS spectrum has a different shape. The Three-colours signal is characterized by an increasing intensity for lower wavenumbers, since the number of intrapulse permutation is higher for low Raman shifts. Also in this case, after having applied KK phase retrieval algorithm, an optimum agreement with the SR spectra can be appreciated.

3.4.2. Broadband CARS on subcellular acids

After having assessed the performance of the system on solvents, we proceeded acquiring biologically relevant data. In particular, subcellular acids were investigated. In this case, a drop of the samples was placed on a 170 μm glass coverslip. The experiments were performed with a LPF at 1050 nm filtering the Stokes pulse, therefore, only two-color CARS contribution can be seen. The spectra of Palmitoleic, Arachidonic, Linoleic, Oleic and Docosahexonic acids were acquired and are shown in fig. 3.22. The investigated acids are fatty acids (FA), that is aliphatic monocarboxylic acids derived from or contained in esterified form in an animal or vegetable fat, oil or wax [86]. Palmitoleic acid is a monounsaturated FA present in all tissues, but in higher concentrations in the liver [87, 88]. Arachidonic acid is a polyunsaturated acid present in the phospholipids of cellular membranes in the body and is abundant in the brain, muscles and liver [89]. It also constitutes 5-15% of the total FAs in most mammal tissue membrane phospholipids [90]. Linoleic acid is an essential polyunsaturated acid occurring in cell membranes and used in the

biosynthesis of Arachidonic acid [89]. Oleic acid is the most prevalent monounsaturated FA in nature. It is found in the phospholipids that make membranes, cholesterol esters, and wax esters [91]. Docosahexonic acid is a polyunsaturated FA especially concentrated in the grey matter of the brain and in the rod outer segments of the retina [92].

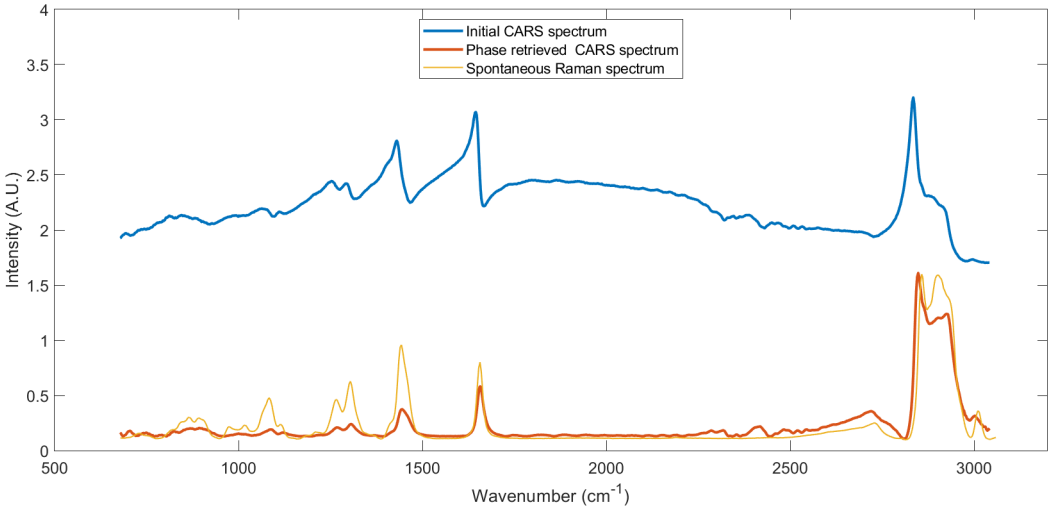

(a) B-CARS before and after NRB removal and SR spectra from Palmitoleic Acid.

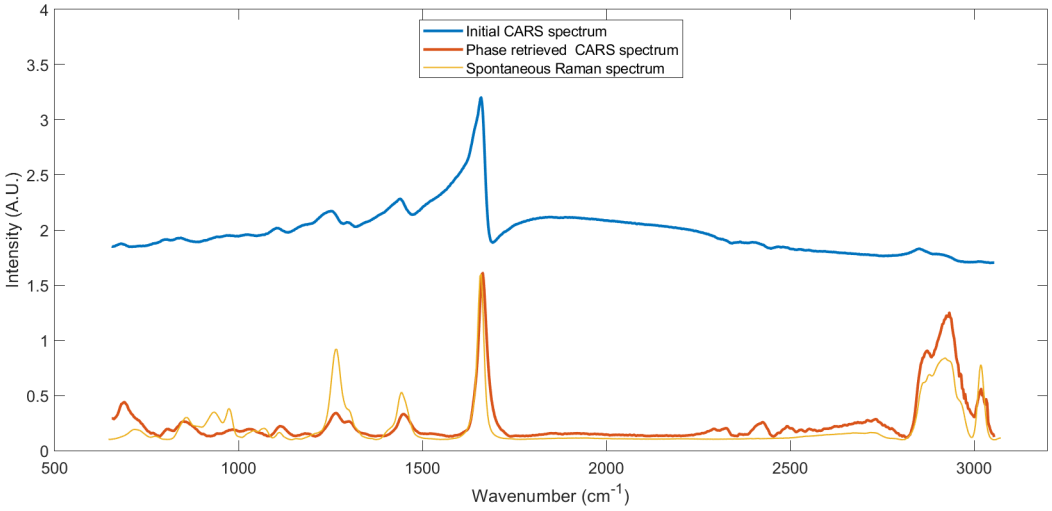

(b) B-CARS before and after NRB removal and SR spectra from Arachidonic Acid.

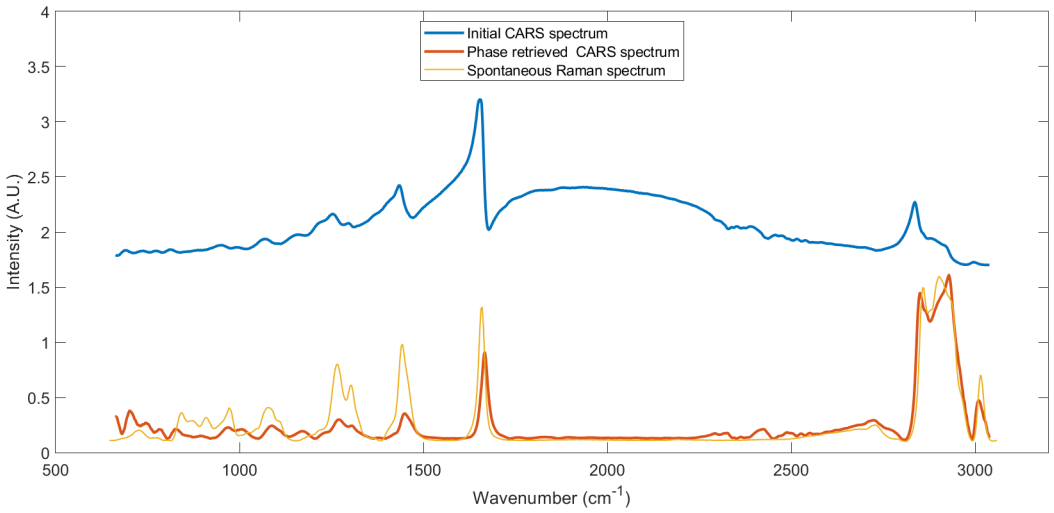

(c) B-CARS before and after NRB removal and SR spectra from Linoleic Acid.

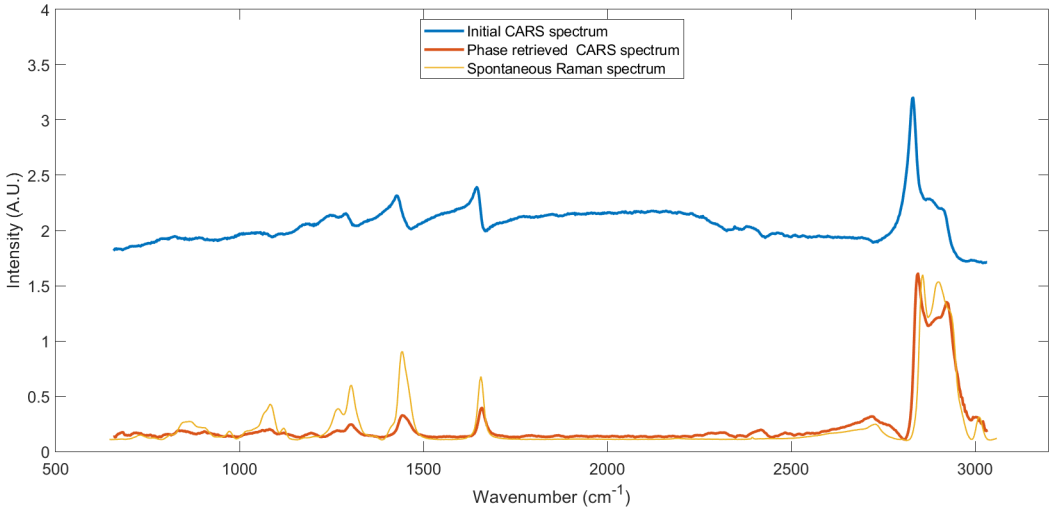

(d) B-CARS before and after NRB removal and SR spectra from Oleic Acid.

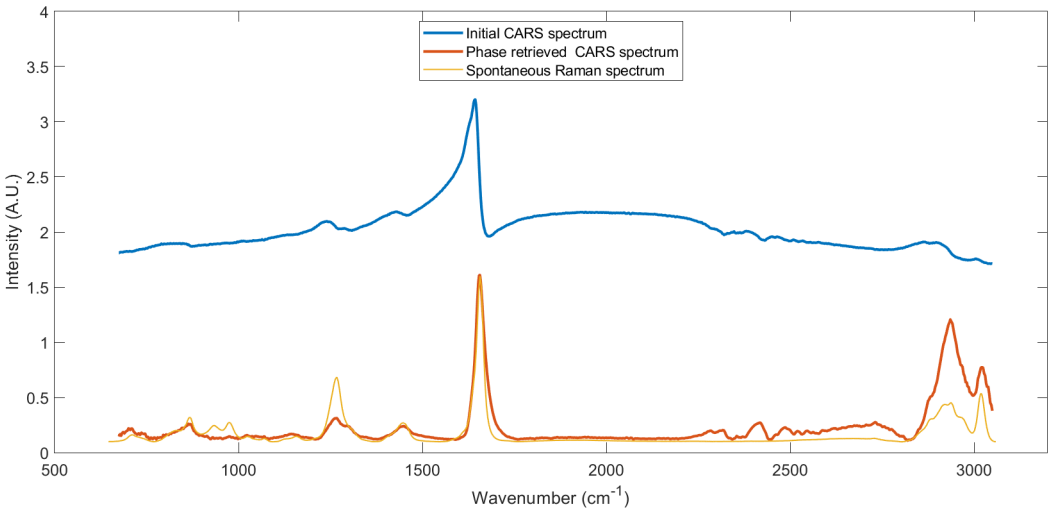

(e) B-CARS before and after NRB removal and SR spectra from Docosahexonic Acid.

Figure 3.22: Two-color B-CARS spectra of subcellular acids before and after NRB removal through phase retrieval and comparison with SR spectra. The spectra acquired are respectively from: (a) Palmitoleic Acid; (b) Arachidonic Acid; (c) Linoleic Acid; (d) Oleic Acid; (e) Docosahexonic Acid. BCARS integration time: 20 ms, 100 averages. Spectra per second: 50.

The spectra were acquired setting the CCD exposure time at 20 ms and an average over 100 measurements have been performed. A higher integration time with respect to solvents measurement was necessary since the intensity of the signal was much lower. The average over many measurement allowed to reach a remarkable SNR. An optimum agreement with the SR spectra can be observed, especially in spectral position.

FAs show three characteristic spectral regions in the fingerprint region of the Raman spectrum: 1060-1090 and 1110-1180 cm^{-1} due to the ν(C-C) stretching vibrations; ≈1300 cm^{-1}, due to δ(CH2) twisting vibrations; 1400-1500 cm^{-1}, caused by δ(CH3) or δ(CH2) deformations, respectively [89]. Analyzing the differences among the spectra in these regions allows to distinguish the different acids. Furthermore, intense band can be seen at 1640-1675 cm^{-1} and at 2800-3000 cm^{-1} due to the C=C and C-H stretching respectively. The C-H stretching region differs from one acid to another and can be successfully exploited to distinguish the various species. It can also be further divided in three parts: 2800-2888 cm^{-1} which is due to CH2 groups; 2909-2967 cm^{-1}, caused by the CH3 groups [93]; an additional feature at ≈ 3000 cm^{-1} related to =C-H moieties which can be seen only in unsaturated FA [89].

3.4.3. Broadband CARS on crystals

B-CARS has gained particular interest in the biomedical field. However, it could be successfully exploited to assess solid state materials as well. In this field, CARS has been used to analyze mainly low-dimensional materials so far. In particular, studies on carbon nanotubes [94, 95], graphene [96–98], and hexagonal boron nitride have been performed [99]. Only recently, BCARS has been exploited to asses single-crystal samples by Hempel *et al.* [100]. In this section, we present an analysis of a single-crystal sample of Lithium Niobate (LN), a ferroelectric crystal frequently employed, particularly in integrated optics, electro-optic modulators, and nonlinear optics [101–105], since it is simple to alter the crystal structure to produce ferroelectric domains. The two-color B-CARS of LN in forward and backward directions are shown in fig. 3.23 and fig. 3.24.

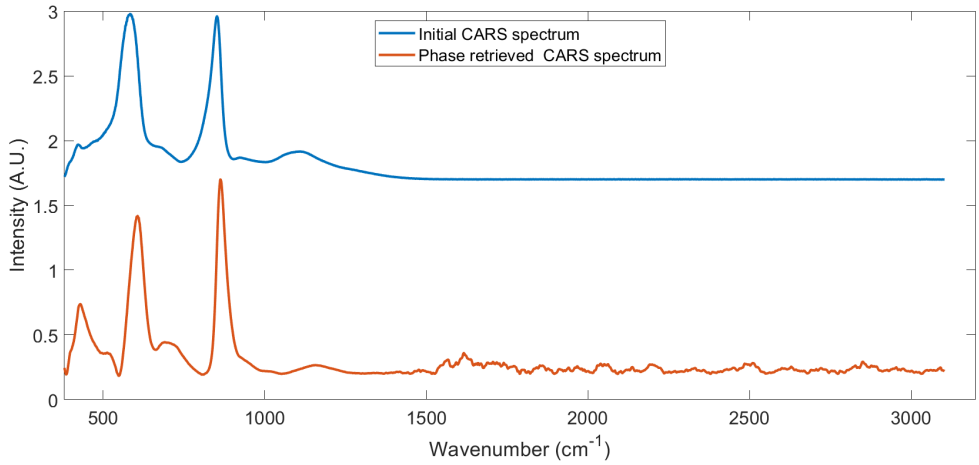

Figure 3.23: Forward BCARS spectra of LiNbO3. Integration time: 0.8 ms, Spectra per second: 1250.

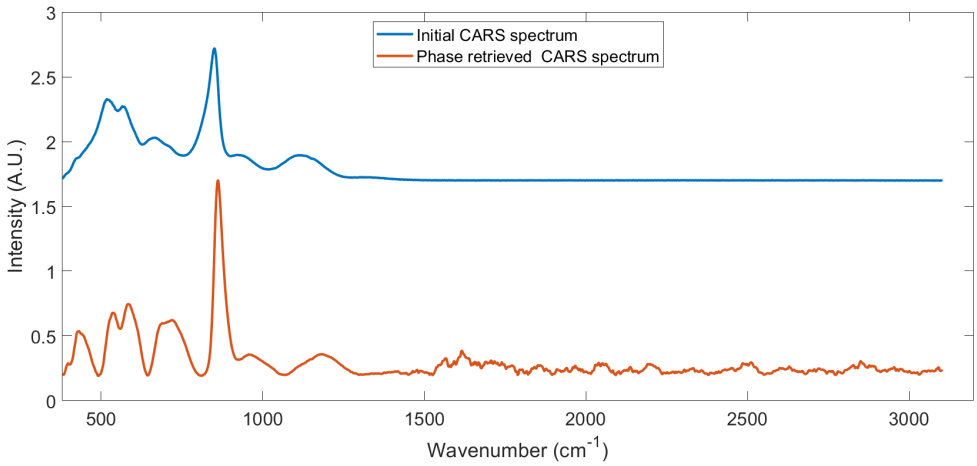

Figure 3.24: Backward BCARS spectra of LiNbO3. Integration time: 0.8 ms, Spectra per second: 1250.

The forward and backward detected spectra present some unexpected differences. Since there are no subwavelength scatterers in the uniform crystal sample, the backward CARS signal should simply be due to a backreflection of the forward one. Therefore, we expected similar spectra with different intensities. However, the Raman peaks are in different positions. The explanation of such phenomenon is beyond the scope of this work. However, we proved that B-CARS spectroscopy can be successfully applied to solid state crystals.

3.4.4. Broadband CARS imaging on test sample

In order to test the ability to distinguish different chemical species, an heterogeneous test sample has been investigated. A mixture of 10-μm polystyrene (PS) and 8-μm polymethylmethacrylate (PMMA) beads were immersed in DMSO and sandwidched between two 170 μm glass coverslips. Figure 3.25 shows the single-pixel raw two-color B-CARS spectra correspondent to the three different species in the sample.

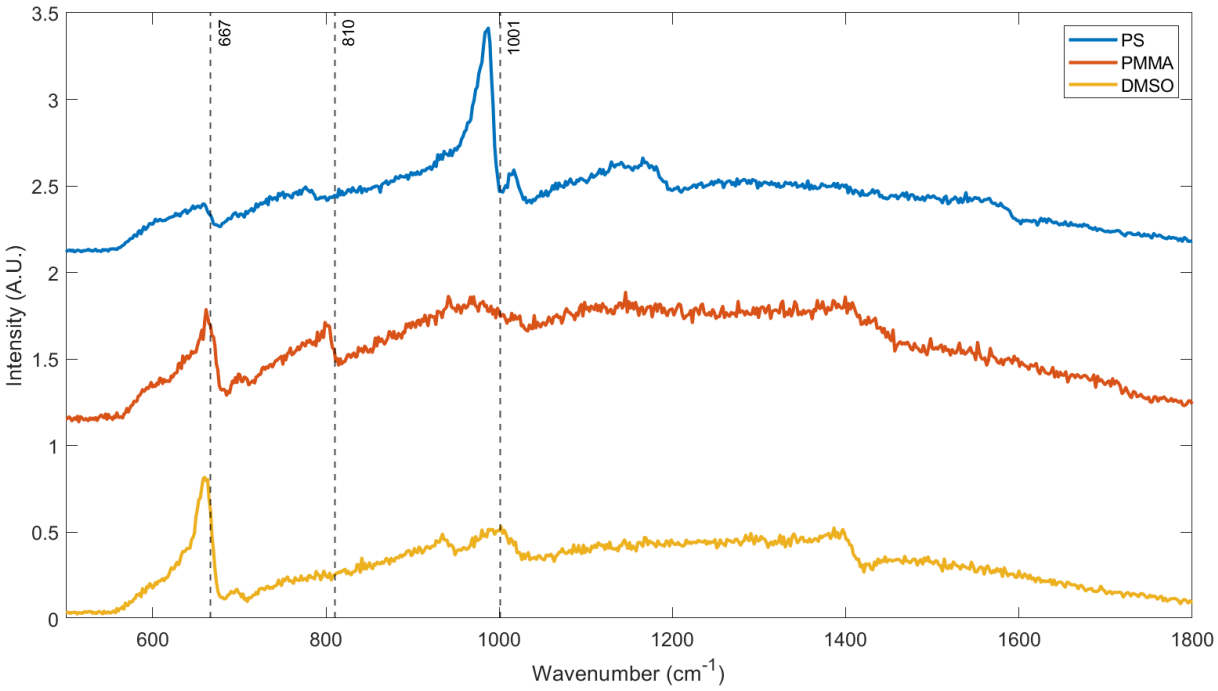

Figure 3.25: Raw two-color B-CARS spectra of the different chemical species before NRB removal. Integration time: 0.8 ms, Spectra per second: 1250.

In this case, only the fingerprint region is shown, since analyzing the main peaks of the constituents in this spectral area allows us to successfully distinguish them. In particular, it can be observed a characteristic peak at 667 cm^{-1} for DMSO, at 810 cm^{-1} for PMMA, and at 1001 cm^{-1} for PS. The acquisition of the raw CARS spectra was repeated for 100 $\times$ 95 pixels in a raster scanning fashion, as explained in section 3.1, obtaining a hypercube with dimensions 100 $\times$ 95 $\times$ 1340, where the last dimension corresponds to the spectral points. These images were acquired with 0.8 ms pixel dwell time, achieving the high-speed acquisition rate of 1250 spectra per second.

The raw CARS images shown in fig. 3.26 are centered at a specific spectral point, corresponding to the wavenumber of the main peak of the different species.

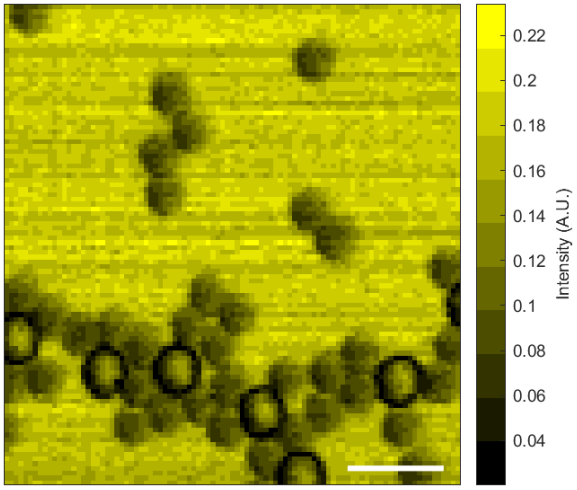

(a) CARS image centered at 667 cm^{-1}.

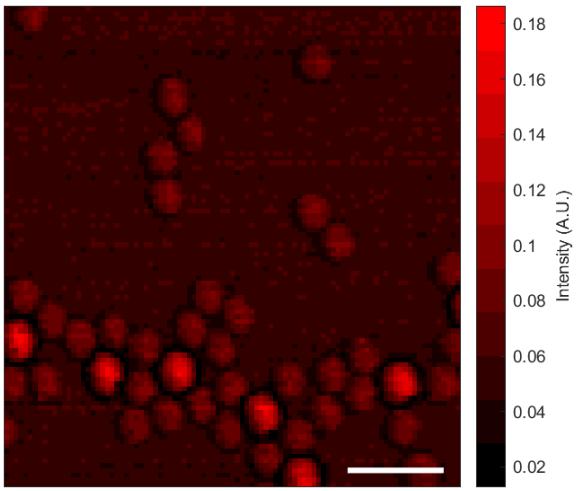

(b) CARS image centered at 810 cm^{-1}.

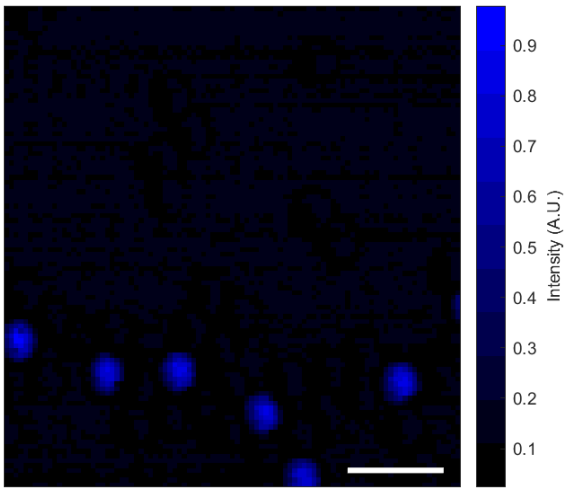

(c) CARS image centered at 1001 cm^{-1}.

Figure 3.26: Raw CARS images of test sample at specific wavenumbers, corresponding to the main peaks of the constituents: (a) 667 cm^{-1}, highlighting DMSO, (b) 810 cm^{-1}, highlighting PMMA, (c) 1001 cm^{-1}, highlighting PS. Scale bars: 20 μm. Pixel dwell time: 0.8 ms, Spectra per second: 1250.

Afterwards, we applied an SVD algorithm to the hypercube to reduce the noise of the spectra, as explained in section 3.3.1. Then, we performed a KK phase retrieval in order to isolate the resonant signal. Subsequently, trough an MCR-ALS analysis, we obtained a concentration map of the three components. With this information we generated a false-color image of the sample, shown in fig. 3.27.

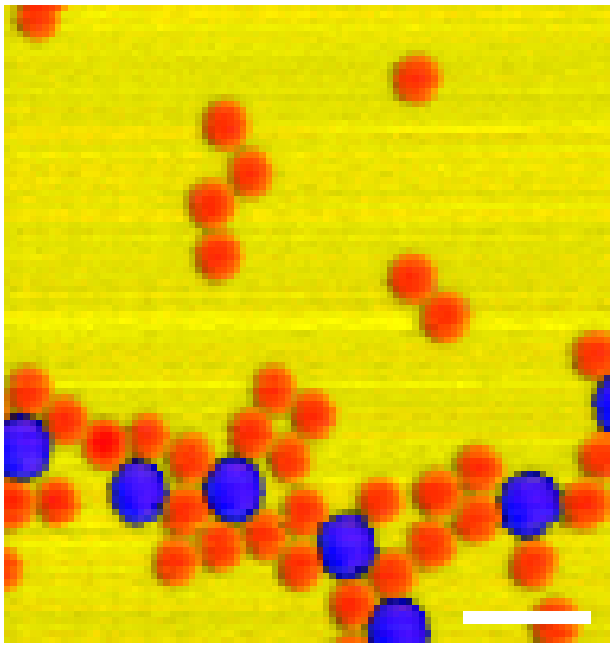

Figure 3.27: False-colours image of test sample obtained through MCR-ALS of B-CARS spectra after NRB removal. Different colours correspond to different chemical species in the sample: yellow for DMSO, red for PMMA beads, blue for PS beads. Scale bar: 20 μm.

The chemical constituents have been successfully distinguished without using any initial guess or prior knowledge on the spectra. The MCR-ALS algorithm also allowed us to retrieve the spectral profiles of the constituents, shown in fig. 3.28.

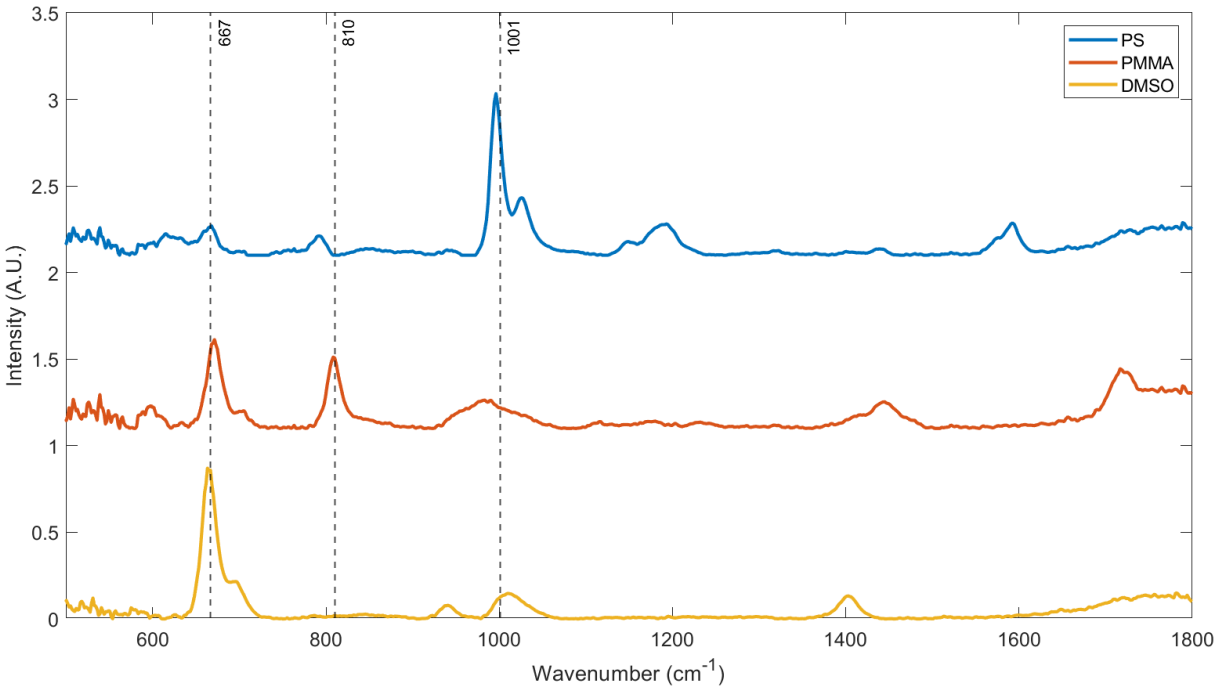

Figure 3.28: Spectra of the different chemical species obtained through MCR-ALS of B-CARS spectra after NRB removal.

After NRB removal through KK and MCR-ALS algorithm, the spectra appear comparable with SR ones, and clearly show the main peaks of the species.

We repeated the experiment on the same type of sample, but changing the LPF applied on the Stokes pulse. The cut-off wavelength was moved from 1050 to 1200 nm in order to detect both the two and three-color CARS signals, as explained in section 3.4.1. In fig. 3.29 the raw CARS spectra of PS, PMMA and DMSO are shown.

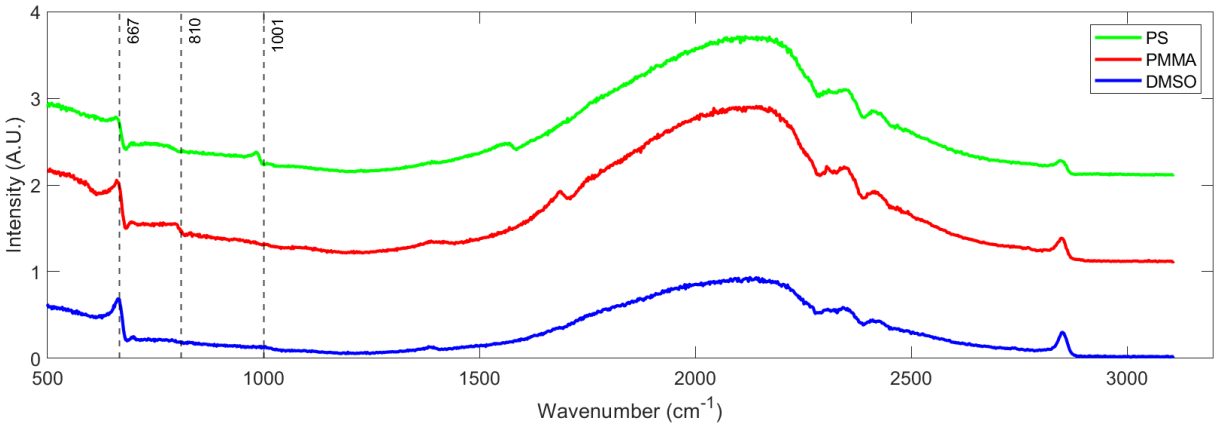

Figure 3.29: Raw two/three-color B-CARS spectra of the different chemical species before NRB removal. Pixel dwell time: 10 ms, Spectra per second: 100.

In fig. 3.29 it is already possible to distinguish the different peaks of the three species. Afterwards, SVD denoising, KK phase retrieval and MCR-ALS algorithm were applied. The resulting false colour image is shown in fig. 3.30.

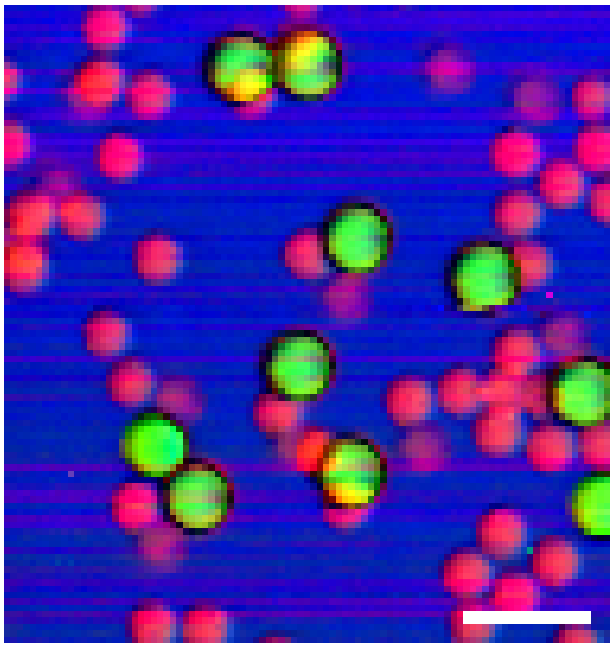

Figure 3.30: False-colours image of test sample obtained through MCR-ALS of B-CARS spectra after NRB removal. Different colours correspond to different chemical species in the sample: blue for DMSO, red for PMMA beads, green for PS beads. Scale bar: 20 μm.

It is possible to observe that the different species are successfully distinguished. MCR-ALS algorithm also provides the spectra of the different components, which are shown in fig. 3.31.

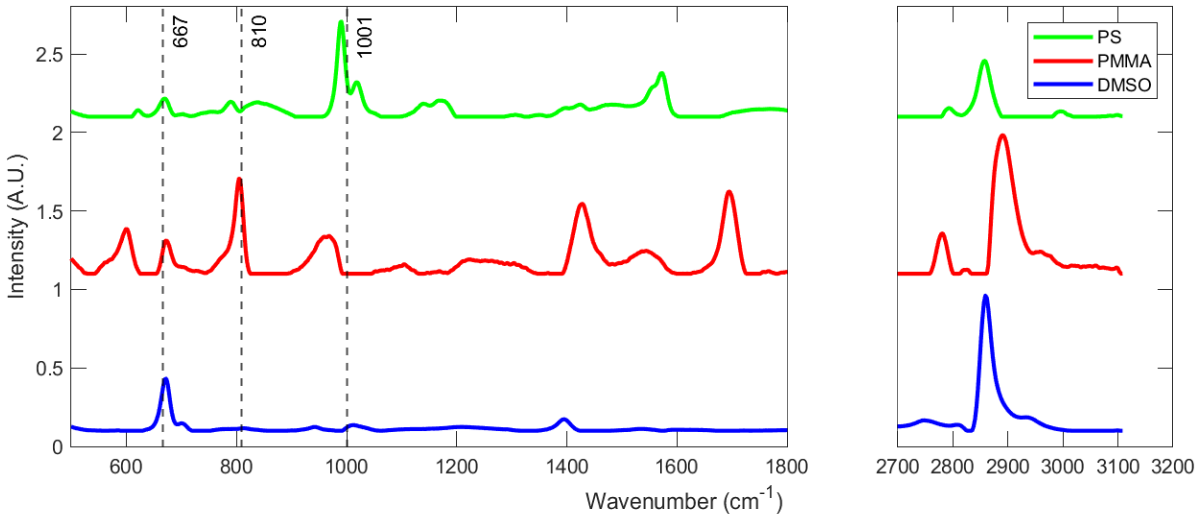

Figure 3.31: Spectra of the different chemical species obtained through MCR-ALS of B-CARS spectra after NRB removal.

The different peaks can be clearly distinguished, in particular, PS beads show a peak at 1001 cm^{-1}, PMMA beads are characterized by a peak at 810 cm^{-1}, while DMSO has a peak at 667 cm^{-1}. We can also observe differences in the spectral positions of the peaks in the C-H stretching region.

In the aformentioned experiments, the forward CARS signal was analyzed. We repeated the experiment on different samples, analyzing the backward CARS. As it was explained in section 2.3.11, due to phase matching reasons, the epi-detected CARS signal coming from the solvent should be critically reduced, while the ones from sub-wavelength scatterers should retain the same intensity of its forward counterpart. In order to prove this, we performed some experiments on samples constituted of PS and PMMA beads with $<1\mu$m diameters immersed in DMSO. Unfortunately, due to the low SNR, it was not possible to obtain relevant results from these analysis. However, we managed to obtain a backward CARS image of 3 μm PS beads in DMSO, shown in fig. 3.32, obtained performing the sum over the spectral dimension of the hypercube.

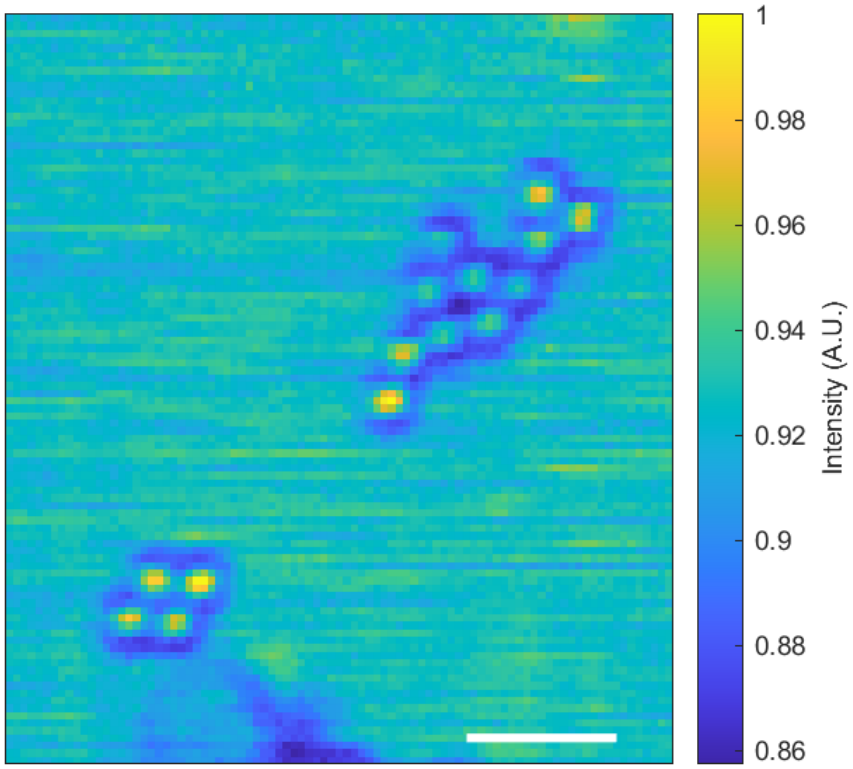

Figure 3.32: B-CARS image of test sample (3 μm PS beads in DMSO) before NRB removal. Pixell dwell time: 20 ms, Spectra per second: 50. Scale bar: 20 μm.

In this case, since the dimension of the beads does not respect the condition in eq. (2.162), we did not expect to see signal. Therefore, the retrieved data can be traced back to the forward CARS backreflected by the glass coverslip. Indeed, no relevant intensity differences can be observed between the signal from the solvent and the beads, as shown in fig. 3.33.

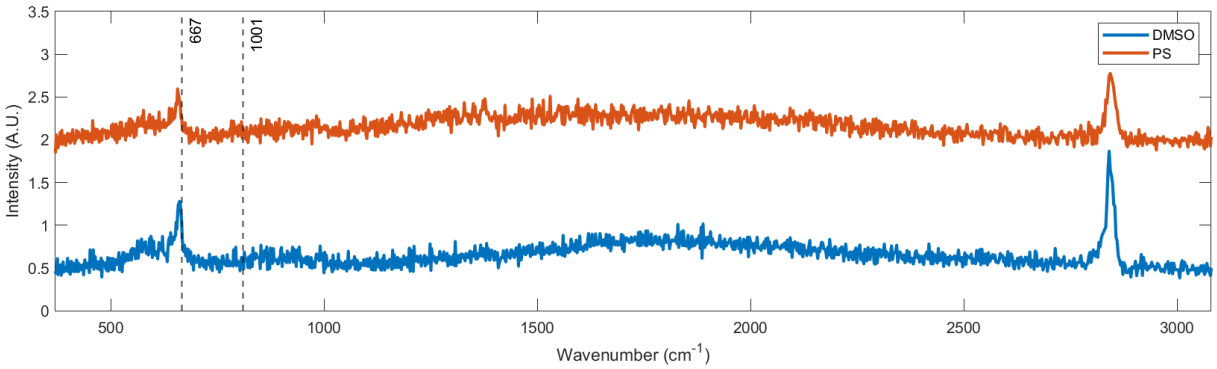

Figure 3.33: Raw B-CARS spectra epi-detected of the different chemical species before NRB removal.

3.4.5. Broadband CARS imaging on biological sample

B-CARS has been proved to be a successful way to perform imaging of biological tissues [47, 66]. In this section, we show the ability of our experimental set-up to execute such images. Figure 3.34 presents an image of a murine head and neck tissue sample, which was collected with 10 ms pixel dwell time over a 250 μm $\times$ 250 μm area (250 pixels $\times$ 250 pixels). It was obtained from a the raw CARS hypercube (250 $\times$ 250 $\times$ 1340) summing over the spectral dimension, before denoising and NRB removal. To perform the measurement, the sample was sandwidched between two 170 μm quartz coverslips. In this case, the LPF at 1050 nm was used, therefore, only the two-color CARS signal can be seen.

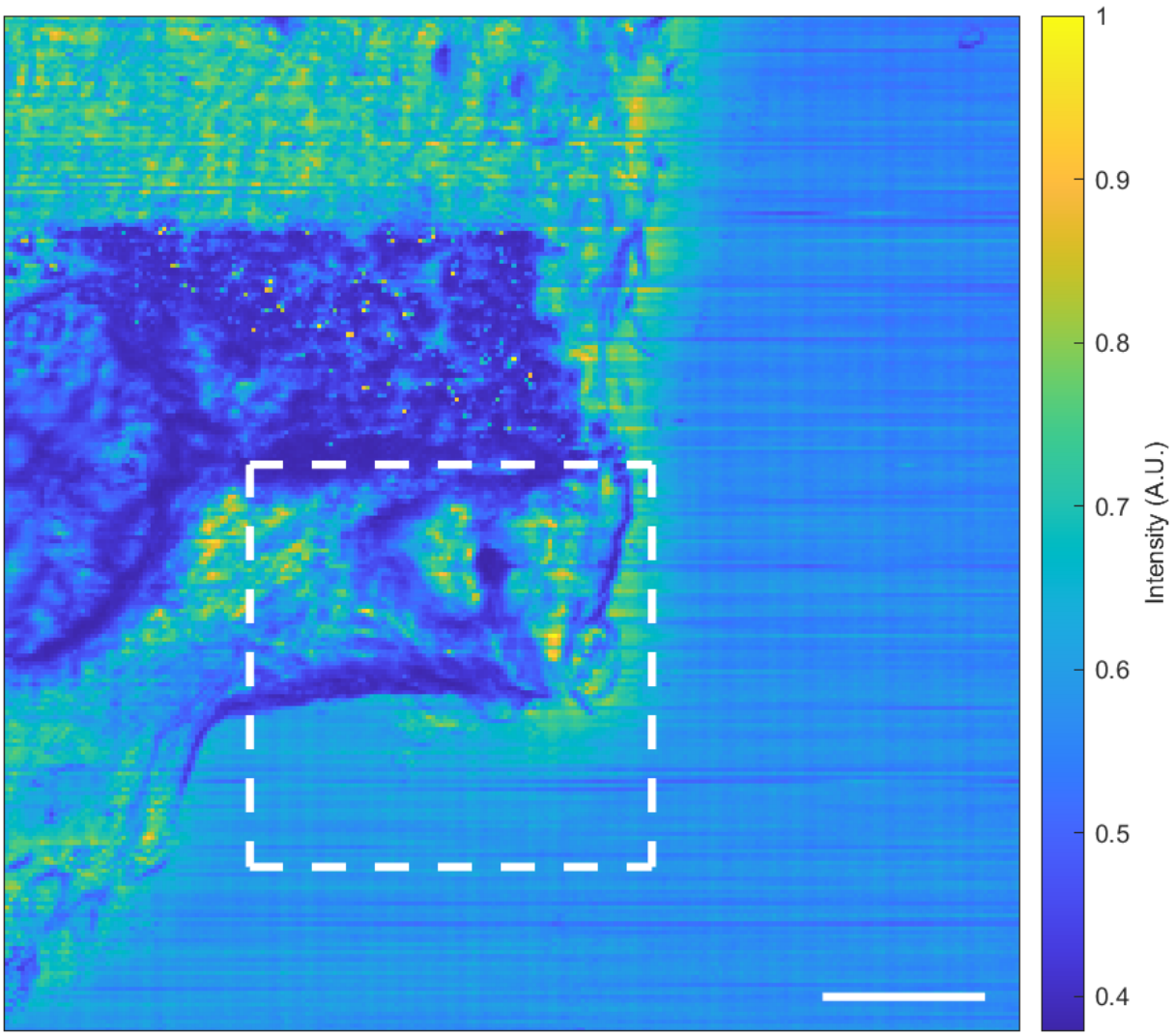

Figure 3.34: B-CARS image of a murine head and neck tissue sample, before NRB removal, obtained summing over the spectrum. Dashed line: portion analyzed through MCR-ALS. Pixel dwell time: 10 ms, Spectra per second: 100. Scale bar: 40 μm.

Afterwards, a portion of this image was analyzed applying an SVD noise-reduction and a KK phase retrieval algorithms[5]. Finally, an MCR-ALS analysis was performed, obtaining the spectra and concentration maps of pure components from the sample. The number of components in the algorithm can be arbitrarly selected. We obtained the best result fixing it to three, where one of the constituents is simply the glass coverslip, from which we do not expect any vibrational signature. In fig. 3.35, the false-colour image resulting from the concentration map is shown, where the parts of biological tissue are depicted in red and green, while the glass in blue.

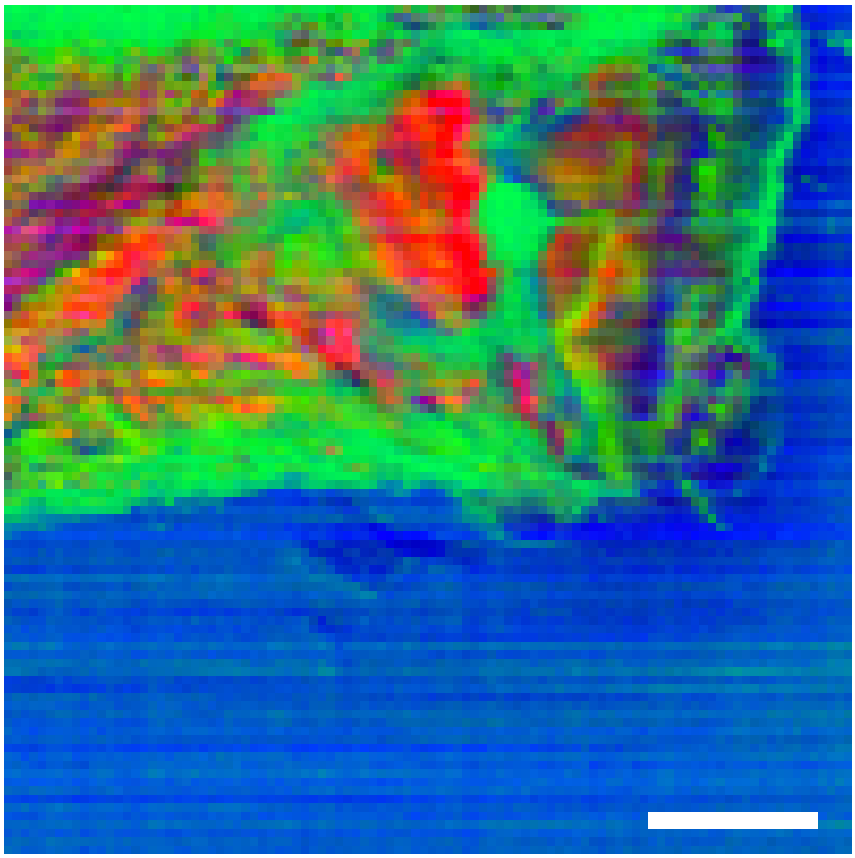

Figure 3.35: B-CARS false colour image after NRB removal obtained through MCR-ALS analysis. Red and green: biological tissue, blue: glass. Scale bar: 20 μm.

The correspondent spectra are shown in fig. 3.36 (only the fingerprint and the C-H stretching region are shown, since no peaks appear in the spectral region in-between, namely the silent region). As we expected, in the glass spectrum no vibrational peaks can be seen. On the other hand, the biological spectrum shows several peaks in the fingerprint region and a band in the C-H stretching region.

[5]It can be noticed that the portion of sample above the analyzed one is damaged. This is due to previous measurements which burnt part of the sample.

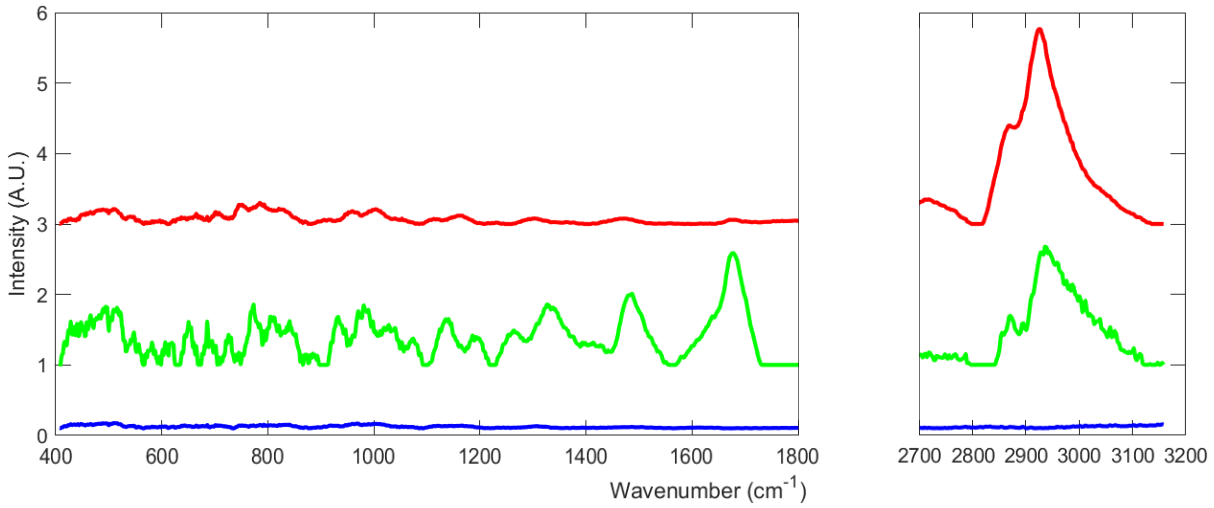

Figure 3.36: B-CARS spectra after NRB removal obtained through MCR-ALS analysis. Red and green: biological tissue, blue: glass.

The spectrum shows a peak at ≈ 1670 cm^{-1}, which can be traced back to amide I/C = C stretching in proteins [66], a peak at ≈ 1488 cm^{-1}, due to nucleotides, a band at ≈ 1300 cm^{-1} due to CH_2 deformations[47]. In order to validate the experiment, a result from Camp *et al.*[47] has been reported in fig. 3.37, showing a great accordance, especially in the regions between 1200-1800 cm^{-1} and 2800-3200 cm^{-1}.

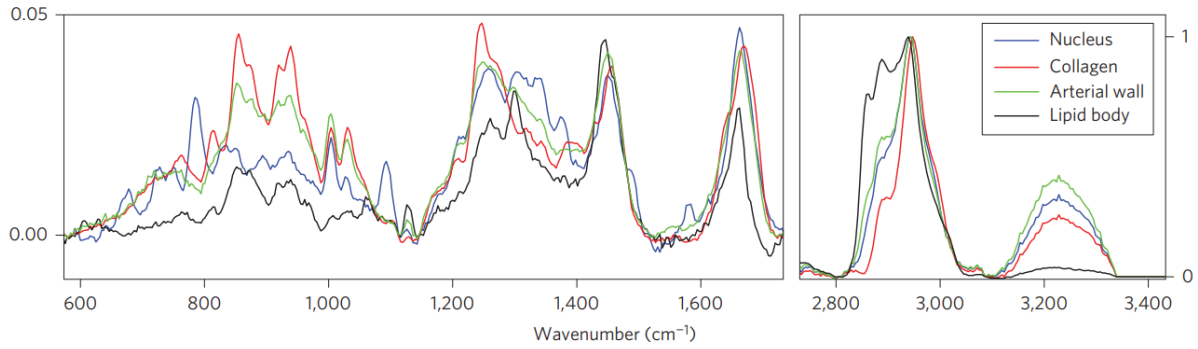

Figure 3.37: B-CARS spectra after NRB removal of different biological specimen. Graph taken from [47].

Eventually, we performed an analogous experiment, imaging a longitudinal section of murine spine (vertebrae). Figure 3.38 shows the raw CARS image of such sample, obtained summing over the spectral dimension of the hypercube. The data were collected with 10 ms pixel dwell time over a 200 $\times$ 200 μm area. In this case, both two and three-color CARS signal were detected, since the LPF1200 was used to cut the broadband spectrum of the Stokes pulse.

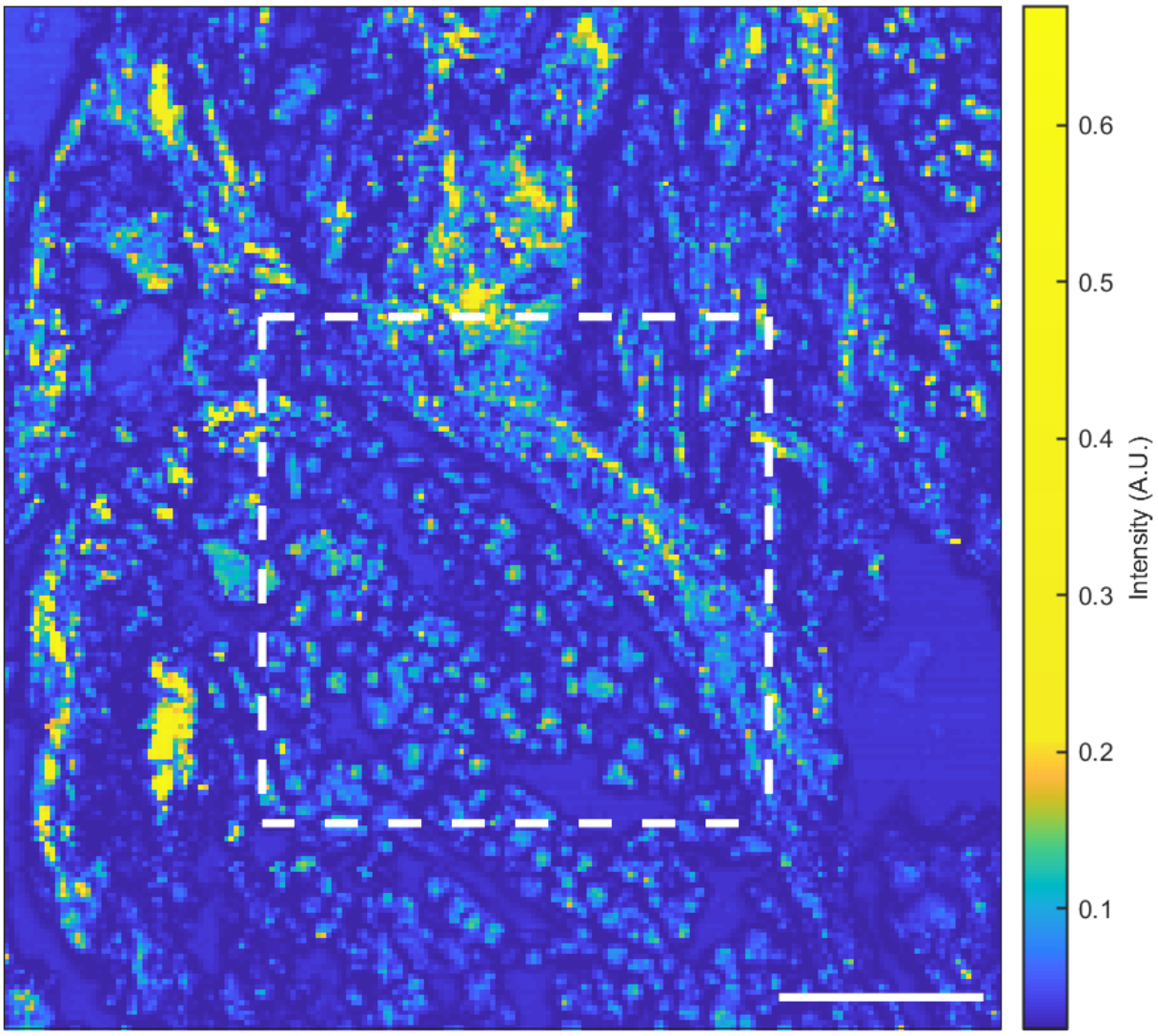

Figure 3.38: B-CARS image of a murine vertebra, before NRB removal, obtained summing over the spectrum. Dashed line: portion analyzed through MCR-ALS. Pixel dwell time: 10 ms, Spectra per second: 100. Scale bar: 40 μm.

Subsequently, the dashed portion of fig. 3.38 was analyzed in further detail. We applied SVD denoising, KK phase retrieval and MCR-ALS algorithms. The number of components in MCR-ALS was set to three. We generated a false color image, shown in fig. 3.39, resulting from the concentration map of the constituent.

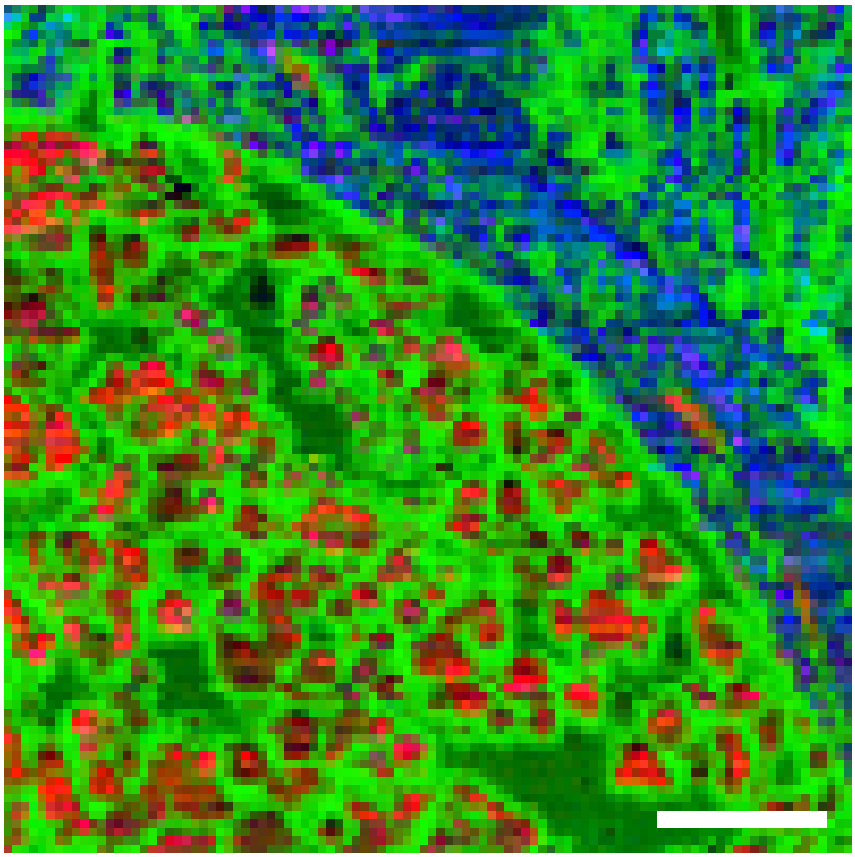

Figure 3.39: B-CARS false colour image after NRB removal obtained through MCR-ALS analysis. Blue: bone, red: marrow, green: background. Scale bar: 20 μm.

We can clearly see that three different constituents are distinguished in the image. The correspondent spectra are shown in fig. 3.40.

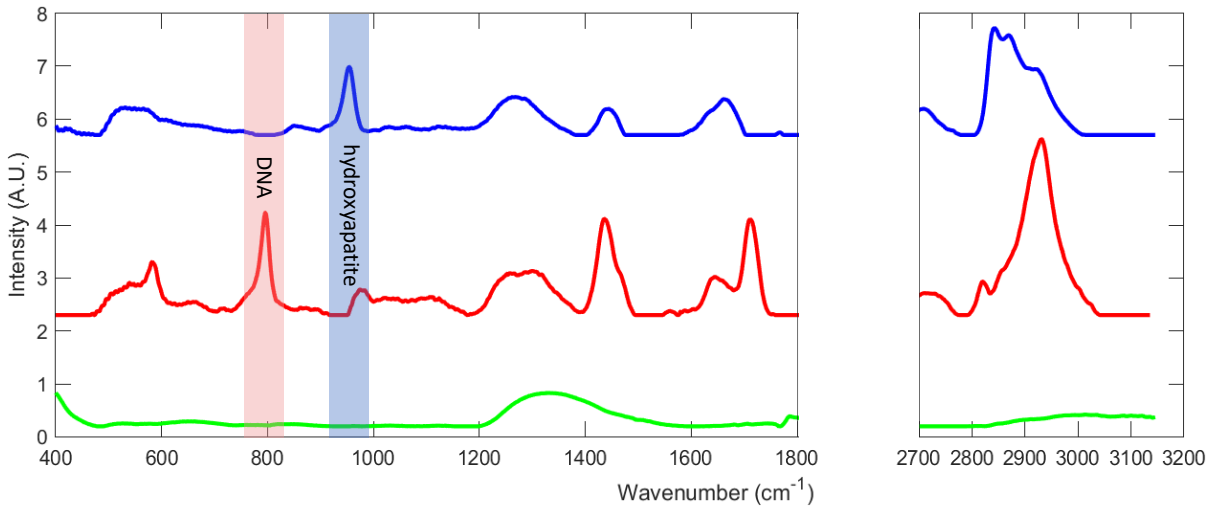

Figure 3.40: B-CARS spectra after NRB removal obtained through MCR-ALS analysis. Blue: bone, red: marrow, green: background.

Analyzing the fingerprint region of the first spectrum (in blue), we can observe an intense band between 940-980 cm^{-1}, which is associated to phosphate bonds in hydroxyapatite, a band at $\approx$ 1250 cm^{-1}, due to the presence of amide III in proteins, a peak at 1440 cm^{-1}, caused by the CH_2 in proteins and lipids, and a band at $\approx$ 1655 cm^{-1}, linked to amide I in proteins [66]. These spectrum characteristics unambiguously correspond to bone, which is primarily distinguished by mineral crystals, mostly calcium phosphate (hydroxyapatite), embedded in an organic protein-rich matrix. The second spectrum (in red) can be easily distinguished from the first one due to the absence of the band at 940-980 cm^{-1}, indicating the absence of hydroxyapatite, and by the presence of a band at $\approx$ 790 cm^{-1}, typically assigned to DNA, mainly found in cells. Furthermore, stronger signal can be seen in the region between 1440-1700 cm^{-1}, indicating a higher concentration of lipids and proteins. Thus, the red spectrum can be assigned to bone marrow, characterized by a high cellular fraction, and consequently by an abundance of DNA. The green spectrum is simply associated to empty regions in the sample. In conclusion, in both the analyzed samples we were able to distinguish the biological tissue from the background and retrieve the spectra of the different chemical species. Furthermore, analyzing the murine vertebra, we successfully recognized the bone and the marrow, separating spatially the constituents.

3.4.6. Time delayed CARS

Eventually, we exploited our set-up to perform time delayed CARS measurements on DMSO and Toluene. After having temporally synchronized the pulses, we manually introduced some delay between pump and Stokes pulses changing the path length of the

pump pulse. We measured the two and three-color CARS spectra for different delays. The results of such measurements are shown in fig. 3.41 and fig. 3.42.

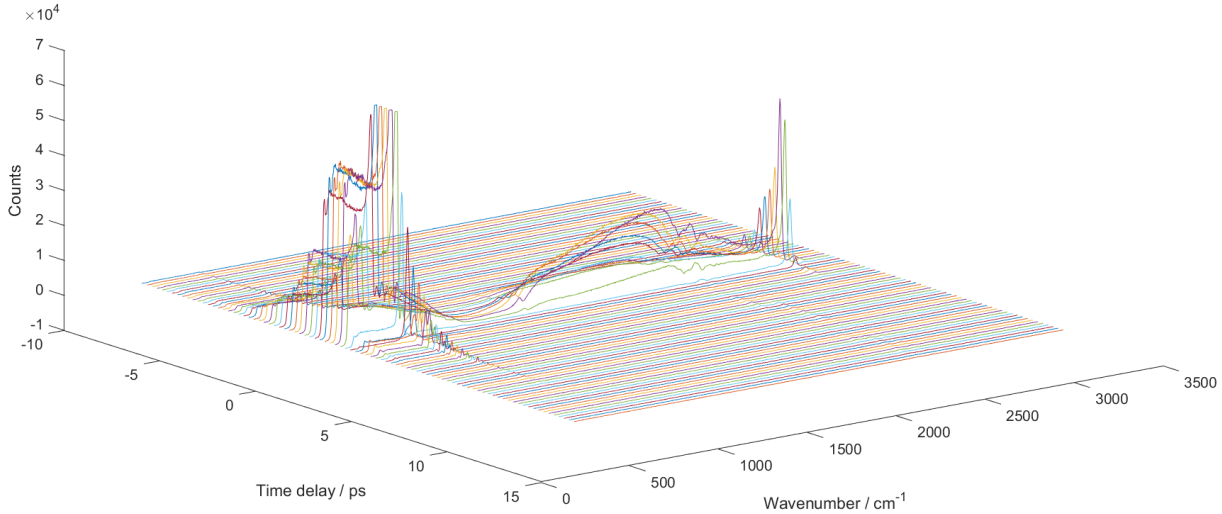

Figure 3.41: Time delay B-CARS DMSO.

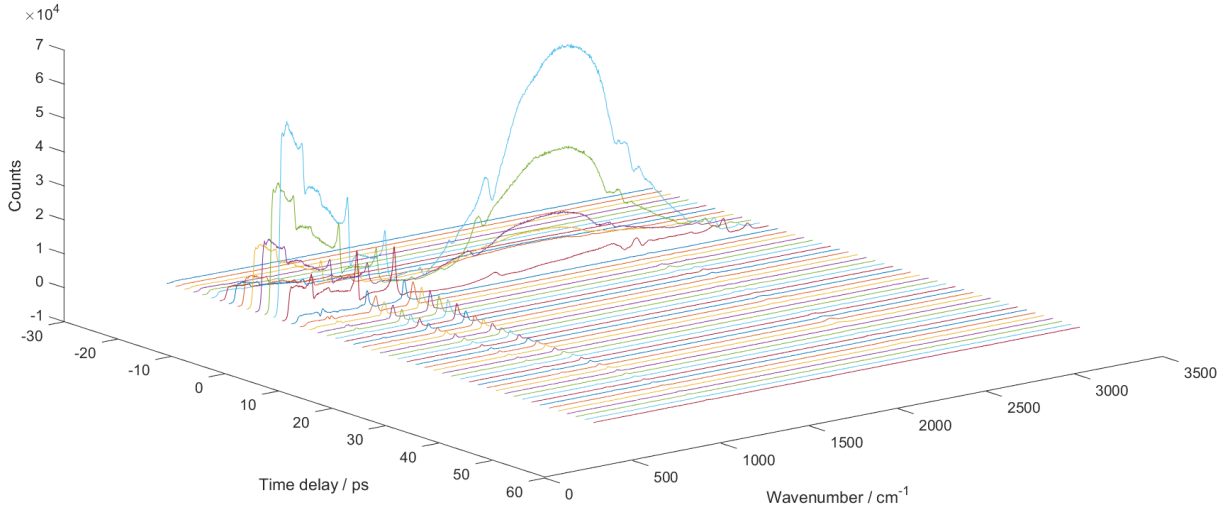

Figure 3.42: Time delay B-CARS Toluene.

As explained in section 2.3.7, the resonant contribution in CARS is characterized by a coherence time in the order of picoseconds, since vibrational levels are populated. On the other hand, the non-resonant contribution arises from electronic contributions, in which only virtual levels are populated. The virtual electronic levels show an extremely short coherence time, in the order of hundreds of femtoseconds. In section 2.3.10, we explained how increasing the delay between the second and third interaction with the beams it is

possible to probe only the resonant part, obtaining Lorentzian peaks without NRB [6]. Increasing the delay between pump and Stokes pulses, we expect to see a reduction of the NRB after few hundreds of femtoseconds. The resonant contribution in two-color CARS should also decrease, since there should be pump photons before and after the Stokes pulse, and increasing the delay between the two pulses we are not respecting this condition. On the other hand, in three-color CARS, the first two interaction are with the Stokes pulse, therefore, increasing the delay between Stokes and pump, in which the latter acts only as a probe, we will detect only the resonant signal, which is characterized by higher coherence time. In both fig. 3.41 and fig. 3.42, we can observe how the NRB and the two-color CARS signal decrease dramatically increasing the delay. By contrast, the vibrational peaks at low wavenumbers (in the three-color CARS region) change shape, going from the distorted shape typical of CARS, to a Lorentzian shape directly comparable to SR spectra. In conclusion, we were able to perform time delayed CARS measurement, proving the underlying theory.

[6]This method is not often applied in spectroscopy and microscopy application because, removing the non-resonant contribution, we remove also the heterodyne amplification of the CARS signal, consequently reducing the SNR.

4 | Conclusions and future developments

This master thesis is focused on Broadband Coherent anti-Stokes Raman scattering (B-CARS) microscopy and spectroscopy. B-CARS microscopy allows one to perform label-free, non-invasive and non-destructive imaging of biological samples at high-speed acquisition, and it has been applied in the field of biology, medicine and chemistry. The CARS signal is a third-order non-linear optical process arising from the interaction of two ultrashort laser pulses at different wavelengths and the sample. The CARS signal is constituted by a resonant and a non-resonant contributions. The resulting signal is affected by a non-resonant background (NRB) which distorts the lineshape of the peaks with respect to the Lorentzian shape obtained through spontaneous Raman spectroscopy. In order to retrieve the typical Raman vibrational spectra, post processing methods are typically employed.

In this work, we showed how our home-build experimental set-up allows us to successfully execute spectroscopy of different liquid and solid samples and to achieve high-speed imaging. The light source is constituted by a fiber-based Ytterbium pulsed femtosecond laser (Monaco, Coherent), providing 268 fs pulses at a rate of 2 MHz, with a wide range of output powers, up to 60 W. The source is used to generate two beams, pump and Stokes, with different features, which have been characterized by means of frequency resolved optical gating (FROG). In particular, the pump pulse has a time duration of $\approx$ 1 ps and is narrowband, since it passes through an etalon which shrinks the bandwidth reaching $\approx$ 1.2 nm, setting the spectral resolution at $\approx$ 10 cm^{-1}. By contrast, the Stokes pulse is broadband, since it is generated propagating the laser pulse through a YAG crystal, triggering supercontinuum (SC) generation. SC generation in bulk media offers many advantages with respect to other methods (such as SC generation in tapered filters or photonic crystal fibers): it is more compact, reliable, easy-to-use and alignment-insensitive. In this way, we were able to broaden the Stokes pulse spectrum up to $\approx$ 1600 nm, covering the entire Raman active region (500-3200 cm^{-1}). Afterwards, a prism compressor allows us to reduce the time duration of the Stokes pulse, reaching a time full width at half maximum

of $\approx$ 30 fs at the sample plane.

We were able to distinguish two different CARS processes, namely, two-color and three-color CARS. In the former case, the molecules in the sample are excited by the pump pulse and reach a virtual level, then, stimulated by the Stokes pulse, they decay to many vibrational levels. A further interaction with the pump probes the sample, retrieving the complete vibrational spectrum. On the other hand, in the three-color CARS mechanism, the first two interactions are impulsively with the Stokes pulse, and the pump pulse acts simply as a probe in the third interaction. The intensity of three-color CARS depends on the number of intrapulse permutations exciting a certain vibrational transition. Since it increases decreasing the wavenumber, this process is particularly suitable to investigate the fingerprint region (characterized by lower wavenumbers). Two long pass filters (LPF) were used to set the minimum wavelength of the broadband pulse. If the cut-off wavelength is set at 1050 nm, the different processes overlap and, since two-color CARS has a higher intensity, it was the only visible. However, setting the cut-off at 1200 nm, the two-color CARS can only excite the vibrational transition over $\approx$ 1330 cm^{-1}. Therefore, in the range 500-1330 cm^{-1} the three-color CARS mechanism was clearly distinguishable. After having acquired a spectrum, we exploited Kramers-Kronig (KK) phase retrieval algorithms to remove the NRB.

We performed two-color B-CARS spectroscopy, spanning the entire Raman-active region, on a few solvents: DMSO, Toluene, Ethanol, Methanol, Isopropanol and Acetone. We acquired the data at high speed (0.8 ms per spectra, limited by the CCD reading time) obtaining an excellent agreement with the reference spectra, measured with a Spontaneous Raman set-up in our laboratory. We repeated the measurement on DMSO and Toluene changing the LPF (moving the cut-off wavelegnth from 1050 to 1200 nm) detecting both two and three-color CARS getting similar results (in this case the acquisition time was slightly higher: 1 ms, due to the lower signal-to-noise ratio (SNR)). We proved that CARS spectroscopy can also be applied to solid state samples, such as Lithium Niobate. We achieved two-color B-CARS spectroscopy of the whole Raman spectrum on subcellular acids, in particular: Palmitoleic, Arachidonic, Linoleic, Oleic and Docosahexonic acids. We found results in optimum agreement with the reference SR spectra. In this case, the acquisition time was 20 ms per spectrum.

We exploited our experimental set-up also to perform imaging. We acquired hyperspectral data in a raster scanning fashion moving the sample with a stepper motor. Afterwards, we applied a singular-value decomposition (SVD) denoising algorithm, a KK phase retrieval to remove the NRB and finally a multi-variate curve resolution (MCR) analysis, based on alternating least square (ALS) algorithms, in order to find the vibrational spectra of the

chemical species in the sample and the relative concentration maps. We applied the aforementioned method on test samples made of PS and PMMA beads immersed in DMSO. We investigated the fingerprint region detecting the two-color CARS signal distinguishing clearly the three constituents and generating a false-colour image. We acquired such data at high-speed, with a pixel dwell time of only 0.8 ms. We repeated the experiment detecting both two and three-color CARS over the entire Raman spectrum obtaining similar results, but at a lower speed (pixell dwell time: 10 ms). Finally, we demonstrated the ability of our set-up to perform imaging detecting the backward propagating CARS from test samples.

We achieved imaging on biological samples, in particular on a murine head and neck tissue and on a slice of a murine vertebra. In the former case, we detected only the two-color signal over the entire vibrational spectrum with a pixel dwell time equal to 10 ms, successfully distinguishing the biological tissue from the background, retrieving biological spectra in great agreement with the literature. In the latter case, we acquired both the two and three-color CARS with a pixel dwell time of 10 ms. We managed to clearly distinguish the bone and the marrow, and to retrieve the relative spectra. We generated a false-colors image where the various constituents are highlighted in different colors.

Finally, we performed time-delayed CARS on DMSO and Toluene showing a physical way to successfully remove the NRB.

Referring to current technological needs, the proposed Broadband CARS microscope may be used to answer urgent biomedical questions, such as senescence and autophagic processes related to cancer in human cells. Similarly, histopathology may also benefit from the advantages provided by the system. In this case, the detection of complex vibrational features over the entire fingerprint and C-H regions, with high spatial resolution and covering relevant tissue regions, would help to measure the detailed biochemical composition of a sample (spectral histopathology), supporting medical doctors in making informed diagnostic and therapeutic decisions.

Bibliography

[1] Chandrasekhara Venkata Raman and Kariamanikkam Srinivasa Krishnan. A new type of secondary radiation. *Nature*, 121(3048):501–502, 1928.

[2] Gisela Eckhardt, Robert W. Hellwarth, Fred J. McClung, Steven E. Schwarz, Daniel Weiner, and E. J. Woodbury. Stimulated raman scattering from organic liquids. *Physical Review Letters*, 9:455–457, 1962.

[3] T. H. Maiman. Stimulated optical radiation in ruby. *Nature*, 187(4736):493–494, Aug 1960. ISSN 1476-4687. doi: 10.1038/187493a0. URL `https://doi.org/10.1038/187493a0`.

[4] Tatsuo Yajima and Masamoto Takatsuji. Higher order optical mixing of raman laser light in nonlinear dielectric media. *Journal of the Physical Society of Japan*, 19:2343–2344, 1964.

[5] P. D. Maker and R. W. Terhune. Study of optical effects due to an induced polarization third order in the electric field strength. *Phys. Rev.*, 148:990–990, Aug 1966. doi: 10.1103/PhysRev.148.990. URL `https://link.aps.org/doi/10.1103/PhysRev.148.990`.

[6] R. F. Begley, A. B. Harvey, R. L. Byer, and B. S. Hudson. Raman spectroscopy with intense, coherent, anti-stokes beams. *Journal of Chemical Physics*, 61(6):2466–2467, January 1974. ISSN 0021-9606. doi: 10.1063/1.1682352.

[7] N. Bloembergen. The stimulated raman effect. *American Journal of Physics*, 35 (11):989–1023, 1967. doi: 10.1119/1.1973774. URL `https://doi.org/10.1119/1.1973774`.

[8] R. W. Hellwarth. Theory of stimulated raman scattering. *Phys. Rev.*, 130:1850–1852, Jun 1963. doi: 10.1103/PhysRev.130.1850. URL `https://link.aps.org/doi/10.1103/PhysRev.130.1850`.

[9] A. Laubereau and Wolfgang Karl Kaiser. Vibrational dynamics of liquids and solids

investigated by picosecond light pulses. *Reviews of Modern Physics*, 50:607–665, 1978.

[10] Haim Lotem, Robert T. Lynch, and Nicolaas Bloembergen. Interference between raman resonances in four-wave difference mixing. *Physical Review A*, 14:1748–1755, 1976.

[11] Y R Shen and N R Bloembergen. Theory of stimulated brillouin and raman scattering. *Physical Review*, 137(6A):A1787–A1805, mar 1965.

[12] M. D. Duncan, J. Reintjes, and T. J. Manuccia. Scanning coherent anti-stokes raman microscope. *Opt. Lett.*, 7(8):350–352, Aug 1982. doi: 10.1364/OL.7.000350. URL `http://opg.optica.org/ol/abstract.cfm?URI=ol-7-8-350`.

[13] Andreas Zumbusch, Gary R. Holtom, and X. Sunney Xie. Three-dimensional vibrational imaging by coherent anti-stokes raman scattering. *Phys. Rev. Lett.*, 82: 4142–4145, May 1999. doi: 10.1103/PhysRevLett.82.4142. URL `https://link.aps.org/doi/10.1103/PhysRevLett.82.4142`.

[14] Evelyn Ploetz, Stefan Laimgruber, Stefan Berner, Wolfgang Zinth, and Peter Gilch. Femtosecond stimulated raman microscopy. *Applied Physics B*, 87:389–393, 2007.

[15] Christian W. Freudiger, Wei Min, Brian G. Saar, Sijia Lu, G. R. Holtom, Chengwei He, Jason C Tsai, Jing xuan Kang, and X. Sunney Xie. Label-free biomedical imaging with high sensitivity by stimulated raman scattering microscopy. *Science*, 322:1857 – 1861, 2008.

[16] James B. Pawley. *Handbook of biological confocal microscopy*. Springer, 2007.

[17] Jeff W Lichtman and José-Angel Conchello. Fluorescence microscopy, Nov 2005. URL `https://www.nature.com/articles/nmeth817`.

[18] M. Bruchez, M. Moronne, P. Gin, S. Weiss, and A. Alivisatos. [pdf] semiconductor nanocrystals as fluorescent biological labels.: Semantic scholar, Jan 1998. URL `https://www.semanticscholar.org/paper/Semiconductor-nanocrystals-as-fluorescent-labels.-Bruchez-Moronne/028bda91ddee26d14cdc0da69d3b716022d736ec`.

[19] Tsien RY;. The green fluorescent protein. URL `https://pubmed.ncbi.nlm.nih.gov/9759496/`.

[20] Dario Polli, Vikas Kumar, Carlo M. Valensise, Marco Marangoni, and Giulio Cerullo. Broadband coherent raman scattering microscopy. *Laser & Photonics*

Reviews, 12(9):1800020, 2018. doi: https://doi.org/10.1002/lpor.201800020. URL https://onlinelibrary.wiley.com/doi/abs/10.1002/lpor.201800020.

[21] Shang Wang, Irina V. Larina, and Kirill V. Larin. Label-free optical imaging in developmental biology. *Biomed. Opt. Express*, 11(4):2017–2040, Apr 2020. doi: 10.1364/BOE.381359. URL http://opg.optica.org/boe/abstract.cfm?URI=boe-11-4-2017.

[22] R. A. Hoebe, C. H. Van Oven, T. W. J. Gadella, P. B. Dhonukshe, C. J. F. Van Noorden, and E. M. M. Manders. Controlled light-exposure microscopy reduces photobleaching and phototoxicity in fluorescence live-cell imaging. *Nature Biotechnology*, 25(2):249–253, Feb 2007. ISSN 1546-1696. doi: 10.1038/nbt1278. URL https://doi.org/10.1038/nbt1278.

[23] Valentin Magidson and Alexey Khodjakov. Chapter 23 - circumventing photodamage in live-cell microscopy. In Greenfield Sluder and David E. Wolf, editors, *Digital Microscopy*, volume 114 of *Methods in Cell Biology*, pages 545–560. Academic Press, 2013. doi: https://doi.org/10.1016/B978-0-12-407761-4.00023-3. URL https://www.sciencedirect.com/science/article/pii/B9780124077614000233.

[24] Rohit Bhargava. Infrared spectroscopic imaging: the next generation. *Appl Spectrosc*, 66(10):1091–1120, October 2012.

[25] George Turrell. 1 - the raman effect. In George Turrell and Jacques Corset, editors, *Raman Microscopy*, pages 1–25. Academic Press, London, 1996. ISBN 978-0-12-189690-4. doi: https://doi.org/10.1016/B978-012189690-4/50021-1. URL https://www.sciencedirect.com/science/article/pii/B9780121896904500211.

[26] Renzo Vanna, Alejandro De la Cadena, Benedetta Talone, Cristian Manzoni, Marco Marangoni, Dario Polli, and Giulio Cerullo. Vibrational imaging for label-free cancer diagnosis and classification. *La Rivista del Nuovo Cimento*, 45(2):107–187, Feb 2022. ISSN 1826-9850. doi: 10.1007/s40766-021-00027-6. URL https://doi.org/10.1007/s40766-021-00027-6.

[27] Mahmoud Ghomi and Authors. *APPLICATIONS OF RAMAN SPECTROSCOPY TO BIOLOGY. From Basic Studies to Disease Diagnosis*. 02 2012.

[28] G J Puppels, F F de Mul, C Otto, J Greve, M Robert-Nicoud, D J Arndt-Jovin, and T M Jovin. Studying single living cells and chromosomes by confocal raman microspectroscopy. *Nature*, 347(6290):301–303, September 1990.

[29] Nicholas Stone, Catherine Kendall, Jenny Smith, Paul Crow, and Hugh Barr. Stone

n, kendall c, smith j, crow p, barr hraman spectroscopy for identification of epithelial cancers. faraday discuss 126: 141-157. *Faraday discussions*, 126:141–57; discussion 169, 02 2004. doi: 10.1039/B304992B.

[30] Abigail S. Haka, Karen Shafer-Peltier, Maryann Fitzmaurice, Joseph P. Crowe, Ramachandra R. Dasari, and M. S. Feld. Diagnosing breast cancer by using raman spectroscopy. *Proceedings of the National Academy of Sciences of the United States of America*, 102 35:12371–6, 2005.

[31] Catherine Kendall, Martin Isabelle, Florian Bazant-Hegemark, Joanne Hutchings, Linda Orr, Jaspreet Babrah, Rebecca Baker, and Nicholas Stone. Vibrational spectroscopy: a clinical tool for cancer diagnostics. *Analyst*, 134:1029–1045, 2009. doi: 10.1039/B822130H. URL `http://dx.doi.org/10.1039/B822130H`.

[32] Matthias Kirsch, Gabriele Schackert, Reiner Salzer, and Christoph Krafft. Raman spectroscopic imaging for in vivo detection of cerebral brain metastases. *Anal Bioanal Chem*, 398(4):1707–1713, August 2010.

[33] Paola Piredda, Manuel Berning, Petra Boukamp, and Andreas Volkmer. Subcellular raman microspectroscopy imaging of nucleic acids and tryptophan for distinction of normal human skin cells and tumorigenic keratinocytes. *Anal Chem*, 87(13): 6778–6785, May 2015.

[34] U Neugebauer, T Bocklitz, J H Clement, C Krafft, and J Popp. Towards detection and identification of circulating tumour cells using raman spectroscopy. *Analyst*, 135(12):3178–3182, October 2010.

[35] Conor Evans and X Xie. Coherent anti-stokes raman scattering microscopy: Chemical imaging for biology and medicine. *Annual review of analytical chemistry (Palo Alto, Calif.)*, 1:883–909, 07 2008. doi: 10.1146/annurev.anchem.1.031207.112754.

[36] Ji-Xin Cheng and Xiaoliang Sunney Xie, editors. *Coherent Raman scattering microscopy*. Series in Cellular and Clinical Imaging. CRC Press, Boca Raton, FL, April 2016.

[37] W Denk, J H Strickler, and W W Webb. Two-photon laser scanning fluorescence microscopy. *Science*, 248(4951):73–76, April 1990.

[38] Yanping Li, Binglin Shen, Shaowei Li, Yihua Zhao, Junle Qu, and Liwei Liu. Review of stimulated raman scattering microscopy techniques and applications in the biosciences. *Advanced Biology*, 5(1):2000184, 2021. doi: https://doi.org/10.1002/adbi.

202000184. URL https://onlinelibrary.wiley.com/doi/abs/10.1002/adbi.202000184.

[39] M Hashimoto, T Araki, and S Kawata. Molecular vibration imaging in the fingerprint region by use of coherent anti-stokes raman scattering microscopy with a collinear configuration. *Opt Lett*, 25(24):1768–1770, December 2000.

[40] P Nandakumar, A Kovalev, and A Volkmer. Vibrational imaging based on stimulated raman scattering microscopy. *New Journal of Physics*, 11(3):033026, mar 2009. doi: 10.1088/1367-2630/11/3/033026. URL https://doi.org/10.1088/1367-2630/11/3/033026.

[41] T. Bocklitz, T. Meyer, M. Schmitt, I. Rimke, F. Hoffmann, F. von Eggeling, G. Ernst, O. Guntinas-Lichius, and J. Popp. Invited article: Comparison of hyperspectral coherent raman scattering microscopies for biomedical applications. *APL Photonics*, 3(9):092404, 2018. doi: 10.1063/1.5030159. URL https://doi.org/10.1063/1.5030159.

[42] Marcus T. Cicerone, Khaled A. Aamer, Young Jong Lee, and Erik Vartiainen. Maximum entropy and time-domain kramers–kronig phase retrieval approaches are functionally equivalent for cars microspectroscopy. *Journal of Raman Spectroscopy*, 43(5):637–643, 2012. doi: https://doi.org/10.1002/jrs.3169. URL https://analyticalsciencejournals.onlinelibrary.wiley.com/doi/abs/10.1002/jrs.3169.

[43] Carsten Cleff, Petra Groß, Carsten Fallnich, Herman L. Offerhaus, Jennifer L. Herek, Kai Kruse, Willem P. Beeker, Chris J. Lee, and Klaus-Jochen Boller. Ground-state depletion for subdiffraction-limited spatial resolution in coherent anti-stokes raman scattering microscopy. *Phys. Rev. A*, 86:023825, Aug 2012. doi: 10.1103/PhysRevA.86.023825. URL https://link.aps.org/doi/10.1103/PhysRevA.86.023825.

[44] Conor L. Evans, Eric O. Potma, Mehron Puoris'haag, Daniel Côté, Charles P. Lin, and X. Sunney Xie. Chemical imaging of tissue in vivo with video-rate coherent anti-stokes raman scattering microscopy. *Proceedings of the National Academy of Sciences*, 102(46):16807–16812, 2005. doi: 10.1073/pnas.0508282102. URL https://www.pnas.org/doi/abs/10.1073/pnas.0508282102.

[45] Brian G. Saar, Christian W. Freudiger, Jay Reichman, C. Michael Stanley, Gary R. Holtom, and X. Sunney Xie. Video-rate molecular imaging in vivo with stimu-

lated raman scattering. *Science*, 330(6009):1368–1370, 2010. doi: 10.1126/science.1197236. URL https://www.science.org/doi/abs/10.1126/science.1197236.

[46] Jae Yong Lee, Se-Hwa Kim, Dae Won Moon, and Eun Seong Lee. Three-color multiplex cars for fast imaging and microspectroscopy in the entire chn stretching vibrational region. *Opt. Express*, 17(25):22281–22295, Dec 2009. doi: 10.1364/OE.17.022281. URL http://opg.optica.org/oe/abstract.cfm?URI=oe-17-25-22281.

[47] Charles H. Camp Jr, Young Jong Lee, John M. Heddleston, Christopher M. Hartshorn, Angela R. Hight Walker, Jeremy N. Rich, Justin D. Lathia, and Marcus T. Cicerone. High-speed coherent raman fingerprint imaging of biological tissues. *Nature Photonics*, 8(8):627–634, Aug 2014. ISSN 1749-4893. doi: 10.1038/nphoton.2014.145. URL https://doi.org/10.1038/nphoton.2014.145.

[48] Esben Ravn Andresen, Henrik Nørgaard Paulsen, Victoria Birkedal, Jan Thøgersen, and Søren Rud Keiding. Broadband multiplex coherent anti-stokes raman scattering microscopy employing photonic-crystal fibers. *J. Opt. Soc. Am. B*, 22(9):1934–1938, Sep 2005. doi: 10.1364/JOSAB.22.001934. URL http://opg.optica.org/josab/abstract.cfm?URI=josab-22-9-1934.

[49] Michiel Müller and Juleon M. Schins. Imaging the thermodynamic state of lipid membranes with multiplex cars microscopy. *The Journal of Physical Chemistry B*, 106(14):3715–3723, Apr 2002. ISSN 1520-6106. doi: 10.1021/jp014012y. URL https://doi.org/10.1021/jp014012y.

[50] Hideaki Kano, Takumi Maruyama, Junko Kano, Yuki Oka, Daiki Kaneta, Tiffany Guerenne, Philippe Leproux, Vincent Couderc, and Masayuki Noguchi. Ultra-multiplex cars spectroscopic imaging with 1-millisecond pixel dwell time. *OSA Continuum*, 2(5):1693–1705, May 2019. doi: 10.1364/OSAC.2.001693. URL http://opg.optica.org/osac/abstract.cfm?URI=osac-2-5-1693.

[51] Hiroaki Yoneyama, Kazuhiro Sudo, Philippe Leproux, Vincent Couderc, Akihito Inoko, and Hideaki Kano. Invited article: Cars molecular fingerprinting using sub-100-ps microchip laser source with fiber amplifier. *APL Photonics*, 3(9):092408, 2018. doi: 10.1063/1.5027006. URL https://doi.org/10.1063/1.5027006.

[52] Tak W. Kee and Marcus T. Cicerone. Simple approach to one-laser, broadband coherent anti-stokes raman scattering microscopy. *Opt. Lett.*, 29(23):2701–2703, Dec 2004. doi: 10.1364/OL.29.002701. URL http://opg.optica.org/ol/abstract.cfm?URI=ol-29-23-2701.

[53] Jingjiang Xu, Baoshan Guo, Kenneth K. Y. Wong, and Kevin K. Tsia. Broad-

band hyperspectral coherent anti-Stokes Raman scattering microscopy for stain-free histological imaging with principal component analysis. In Ammasi Periasamy, Peter T. C. So, and Karsten König, editors, *Multiphoton Microscopy in the Biomedical Sciences XIV*, volume 8948, page 89480R. International Society for Optics and Photonics, SPIE, 2014. doi: 10.1117/12.2039215. URL https://doi.org/10.1117/12.2039215.

[54] Hideaki Kano and Hiro-o Hamaguchi. Ultrabroadband (>2500cm−1) multiplex coherent anti-stokes raman scattering microspectroscopy using a supercontinuum generated from a photonic crystal fiber. *Applied Physics Letters*, 86(12):121113, 2005. doi: 10.1063/1.1883714. URL https://doi.org/10.1063/1.1883714.

[55] Meng Cui, Manuel Joffre, Joshua Skodack, and Jennifer P. Ogilvie. Interferometric fourier transform coherent anti-stokes raman scattering. *Opt. Express*, 14(18):8448–8458, Sep 2006. doi: 10.1364/OE.14.008448. URL http://opg.optica.org/oe/abstract.cfm?URI=oe-14-18-8448.

[56] Kazuki Hashimoto, Megumi Takahashi, Takuro Ideguchi, and Keisuke Goda. Broadband coherent raman spectroscopy running at 24,000 spectra per second. *Scientific Reports*, 6(1):21036, Feb 2016. ISSN 2045-2322. doi: 10.1038/srep21036. URL https://doi.org/10.1038/srep21036.

[57] Alex Soares Duarte, Christoph Schnedermann, and Philipp Kukura. Wide-field detected fourier transform cars microscopy. *Scientific Reports*, 6(1):37516, Nov 2016. ISSN 2045-2322. doi: 10.1038/srep37516. URL https://doi.org/10.1038/srep37516.

[58] Takuro Ideguchi, Simon Holzner, Birgitta Bernhardt, Guy Guelachvili, Nathalie Picqué, and Theodor W. Hänsch. Coherent raman spectro-imaging with laser frequency combs. *Nature*, 502(7471):355–358, Oct 2013. ISSN 1476-4687. doi: 10.1038/nature12607. URL https://doi.org/10.1038/nature12607.

[59] Audrius Dubietis, Gintaras Tamošauskas, Rosvaldas Šuminas, Vytautas Jukna, and Arnaud Couairon. Ultrafast supercontinuum generation in bulk condensed media (invited review). 2017. doi: 10.48550/ARXIV.1706.04356. URL https://arxiv.org/abs/1706.04356.

[60] Andrew Weiner. *Ultrafast optics*, volume 72. John Wiley & Sons, 2011.

[61] R. L. Fork, O. E. Martinez, and J. P. Gordon. Negative dispersion using pairs of prisms. *Optics Letters*, 9(5):150, May 1984. doi: 10.1364/ol.9.000150. URL https://doi.org/10.1364/ol.9.000150.

[62] Hongying Liu, Tian Lan, Xiaomei Chen, and Guoqiang Ni. Dispersion compensation based on prism compressor. In Takashige Omatsu, editor, *SPIE Proceedings*. SPIE, April 2017. doi: 10.1117/12.2274789. URL https://doi.org/10.1117/12.2274789.

[63] Robert W. Boyd. Chapter 2 - wave-equation description of nonlinear optical interactions. In Robert W. Boyd, editor, *Nonlinear Optics (Third Edition)*, pages 69–133. Academic Press, Burlington, third edition edition, 2008. ISBN 978-0-12-369470-6. doi: https://doi.org/10.1016/B978-0-12-369470-6.00002-2. URL https://www.sciencedirect.com/science/article/pii/B9780123694706000022.

[64] Hervé Rigneault. Chapter 1 - coherent raman scattering processes. In Ji-Xin Cheng, Wei Min, Yasuyuki Ozeki, and Dario Polli, editors, *Stimulated Raman Scattering Microscopy*, pages 3–20. Elsevier, 2022. ISBN 978-0-323-85158-9. doi: https://doi.org/10.1016/B978-0-323-85158-9.00004-X. URL https://www.sciencedirect.com/science/article/pii/B978032385158900004X.

[65] Jiabao Xu, Tong Yu, Christos E. Zois, Ji-Xin Cheng, Yuguo Tang, Adrian L. Harris, and Wei E. Huang. Unveiling cancer metabolism through spontaneous and coherent raman spectroscopy and stable isotope probing. *Cancers*, 13(7), 2021. ISSN 2072-6694. doi: 10.3390/cancers13071718. URL https://www.mdpi.com/2072-6694/13/7/1718.

[66] Federico Vernuccio, Arianna Bresci, Benedetta Talone, Alejandro de la Cadena, Chiara Ceconello, Stefano Mantero, Cristina Sobacchi, Renzo Vanna, Giulio Cerullo, and Dario Polli. Fingerprint multiplex cars at high speed based on supercontinuum generation in bulk media and deep learning spectral denoising. *Opt. Express*, 30 (17):30135–30148, Aug 2022. doi: 10.1364/OE.463032. URL http://opg.optica.org/oe/abstract.cfm?URI=oe-30-17-30135.

[67] Francesco Masia, Adam Glen, Phil Stephens, Paola Borri, and Wolfgang Langbein. Quantitative chemical imaging and unsupervised analysis using hyperspectral coherent anti-stokes raman scattering microscopy. *Analytical Chemistry*, 85 (22):10820–10828, Nov 2013. ISSN 0003-2700. doi: 10.1021/ac402303g. URL https://doi.org/10.1021/ac402303g.

[68] Keisuke Isobe, Akira Suda, Masahiro Tanaka, Hiroshi Hashimoto, Fumihiko Kannari, Hiroyuki Kawano, Hideaki Mizuno, Atsushi Miyawaki, and Katsumi Midorikawa. Single-pulse coherent anti-stokes raman scattering microscopy employing an octave spanning pulse. *Opt. Express*, 17(14):11259–11266, Jul 2009. doi:

10.1364/OE.17.011259. URL http://opg.optica.org/oe/abstract.cfm?URI=oe-17-14-11259.

[69] Wolfgang Langbein, Israel Rocha-Mendoza, and Paola Borri. Single source coherent anti-stokes raman microspectroscopy using spectral focusing. *Applied Physics Letters*, 95(8):081109, 2009. doi: 10.1063/1.3216073. URL https://doi.org/10.1063/1.3216073.

[70] Anne-Laure Calendron, Hüseyin Çankaya, Giovanni Cirmi, and Franz X. Kärtner. White-light generation with sub-ps pulses. *Opt. Express*, 23(11):13866–13879, Jun 2015. doi: 10.1364/OE.23.013866. URL http://opg.optica.org/oe/abstract.cfm?URI=oe-23-11-13866.

[71] B. Talone, M. Bazzarelli, A. Schirato, F. Dello Vicario, D. Viola, E. Jacchetti, M. Bregonzio, M. T. Raimondi, G. Cerullo, and D. Polli. Phototoxicity induced in living hela cells by focused femtosecond laser pulses: a data-driven approach. *Biomed. Opt. Express*, 12(12):7886–7905, Dec 2021. doi: 10.1364/BOE.441225. URL http://opg.optica.org/boe/abstract.cfm?URI=boe-12-12-7886.

[72] Jennifer P. Ogilvie, Meng Cui, Dmitry Pestov, Alexei V. Sokolov, and Marlan O. Scully. Time-delayed coherent raman spectroscopy. *Molecular Physics*, 106(2-4):587–594, 2008. doi: 10.1080/00268970801961005. URL https://doi.org/10.1080/00268970801961005.

[73] Andreas Volkmer, Ji-Xin Cheng, and X. Sunney Xie. Vibrational imaging with high sensitivity via epidetected coherent anti-stokes raman scattering microscopy. *Physical Review Letters*, 87(2), June 2001. doi: 10.1103/physrevlett.87.023901. URL https://doi.org/10.1103/physrevlett.87.023901.

[74] Audrius Dubietis, Gintaras Tamosauskas, Rosvaldas Šuminas, Vytautas Jukna, and Arnaud Couairon. Ultrafast supercontinuum generation in bulk condensed media. *Lithuanian Journal of Physics*, 57, 10 2017. doi: 10.3952/physics.v57i3.3541.

[75] A. Couairon and A. Mysyrowicz. Femtosecond filamentation in transparent media. *Physics Reports*, 441(2-4):47–189, March 2007. doi: 10.1016/j.physrep.2006.12.005. URL https://doi.org/10.1016/j.physrep.2006.12.005.

[76] Sergey Mitryukovskiy. Coherent secondary radiation from femtosecond laser filaments. 09 2014.

[77] D.J. Kane and R. Trebino. Characterization of arbitrary femtosecond pulses using

frequency-resolved optical gating. *IEEE Journal of Quantum Electronics*, 29(2): 571–579, 1993. doi: 10.1109/3.199311.

[78] Daniel J. Kane, Jeremy Weston, and Kai-Chien J. Chu. Real-time inversion of polarization gate frequency-resolved optical gating spectrograms. *Appl. Opt.*, 42(6): 1140–1144, Feb 2003. doi: 10.1364/AO.42.001140. URL `http://opg.optica.org/ao/abstract.cfm?URI=ao-42-6-1140`.

[79] Tracy Sharp Clement, A. J. Taylor, and Daniel J. Kane. Single-shot measurement of the amplitude and phase of ultrashort laser pulses in the violet. *Opt. Lett.*, 20 (1):70–72, Jan 1995. doi: 10.1364/OL.20.000070. URL `http://opg.optica.org/ol/abstract.cfm?URI=ol-20-1-70`.

[80] Charles H. Camp Jr., John S. Bender, and Young Jong Lee. Real-time and high-throughput raman signal extraction and processing in CARS hyperspectral imaging. *Optics Express*, 28(14):20422, June 2020. doi: 10.1364/oe.397606. URL `https://doi.org/10.1364/oe.397606`.

[81] Pavel V. Kolesnichenko, Jonathan O. Tollerud, and Jeffrey A. Davis. Background-free time-resolved coherent raman spectroscopy (csrs and cars): Heterodyne detection of low-energy vibrations and identification of excited-state contributions. *APL Photonics*, 4(5):056102, 2019. doi: 10.1063/1.5090585. URL `https://doi.org/10.1063/1.5090585`.

[82] Pascal Berto, Esben Ravn Andresen, and Hervé Rigneault. Background-free stimulated raman spectroscopy and microscopy. *Phys. Rev. Lett.*, 112:053905, Feb 2014. doi: 10.1103/PhysRevLett.112.053905. URL `https://link.aps.org/doi/10.1103/PhysRevLett.112.053905`.

[83] Marcus T. Cicerone, Khaled A. Aamer, Young Jong Lee, and Erik Vartiainen. Maximum entropy and time-domain kramers-kronig phase retrieval approaches are functionally equivalent for CARS microspectroscopy. *Journal of Raman Spectroscopy*, 43 (5):637–643, April 2012. doi: 10.1002/jrs.3169. URL `https://doi.org/10.1002/jrs.3169`.

[84] Charles H. Camp, Young Jong Lee, and Marcus T. Cicerone. Quantitative, comparable coherent anti-stokes raman scattering (CARS) spectroscopy: correcting errors in phase retrieval. *Journal of Raman Spectroscopy*, 47(4):408–415, October 2015. doi: 10.1002/jrs.4824. URL `https://doi.org/10.1002/jrs.4824`.

[85] Imaiyan Chitra Ragupathy, Volker Schweikhard, and Andreas Zumbusch. Multivariate analysis of hyperspectral stimulated raman scattering microscopy images.

Journal of Raman Spectroscopy, 52(9):1630–1642, June 2021. doi: 10.1002/jrs.6184. URL https://doi.org/10.1002/jrs.6184.

[86] International Union of Pure and Applied Chemistry. Iupac compendium of chemical terminology – the gold book, 2009. URL http://goldbook.iupac.org/.

[87] Zhi-Hong Yang, Hiroko Miyahara, and Akimasa Hatanaka. Chronic administration of palmitoleic acid reduces insulin resistance and hepatic lipid accumulation in KK-Ay mice with genetic type 2 diabetes. *Lipids Health Dis.*, 10(1):120, July 2011.

[88] L Hagenfeldt, J Wahren, B Pernow, and L Räf. Uptake of individual free fatty acids by skeletal muscle and liver in man. *J. Clin. Invest.*, 51(9):2324–2330, September 1972.

[89] K. Czamara, K. Majzner, M. Z. Pacia, K. Kochan, A. Kaczor, and M. Baranska. Raman spectroscopy of lipids: a review. *Journal of Raman Spectroscopy*, 46(1):4–20, 2015. doi: https://doi.org/10.1002/jrs.4607. URL https://analyticalsciencejournals.onlinelibrary.wiley.com/doi/abs/10.1002/jrs.4607.

[90] M Neuringer, G J Anderson, and W E Connor. The essentiality of n-3 fatty acids for the development and function of the retina and brain. *Annu. Rev. Nutr.*, 8(1): 517–541, 1988.

[91] James M. Ntambi and Makoto Miyazaki. Recent insights into stearoyl-coa desaturase-1. *Current Opinion in Lipidology*, 14(3), 2003. ISSN 0957-9672. URL https://journals.lww.com/co-lipidology/Fulltext/2003/06000/Recent_insights_into_stearoyl_CoA_desaturase_1.5.aspx.

[92] P. C. Calder. Docosahexaenoic acid. *Annals of Nutrition and Metabolism*, 69(suppl 1)(Suppl. 1):8–21, 2016. ISSN 0250-6807. doi: 10.1159/000448262. URL https://www.karger.com/DOI/10.1159/000448262.

[93] Donald F. H. Wallach and Surendra Pal Verma. Raman and resonance-raman scattering by erythrocyte ghosts. *Biochimica et biophysica acta*, 382 4:542–51, 1975.

[94] Katsuyoshi Ikeda and Kohei Uosaki. Coherent phonon dynamics in single-walled carbon nanotubes studied by time-frequency two-dimensional coherent anti-stokes raman scattering spectroscopy. *Nano Letters*, 9(4):1378–1381, Apr 2009. ISSN 1530-6984. doi: 10.1021/nl803027c. URL https://doi.org/10.1021/nl803027c.

[95] Alesia Paddubskaya, Danielis Rutkauskas, Renata Karpicz, Galina Dovbeshko, Nadezhda Nebogatikova, Irina Antonova, and Andrej Dementjev. Recognition of

spatial distribution of cnt and graphene in hybrid structure by mapping with coherent anti-stokes raman microscopy. *Nanoscale Research Letters*, 15(1):37, Feb 2020. ISSN 1556-276X. doi: 10.1186/s11671-020-3264-8. URL https://doi.org/10.1186/s11671-020-3264-8.

[96] Galyna Dovbeshko, Olena Fesenko, Andrej Dementjev, Renata Karpicz, Vladimir Fedorov, and Oleg Yu Posudievsky. Coherent anti-stokes raman scattering enhancement of thymine adsorbed on graphene oxide. *Nanoscale Research Letters*, 9(1):263, May 2014. ISSN 1556-276X. doi: 10.1186/1556-276X-9-263. URL https://doi.org/10.1186/1556-276X-9-263.

[97] Juha Koivistoinen, Pasi Myllyperkiö, and Mika Pettersson. Time-resolved coherent anti-stokes raman scattering of graphene: Dephasing dynamics of optical phonon. *The Journal of Physical Chemistry Letters*, 8(17):4108–4112, Sep 2017. doi: 10.1021/acs.jpclett.7b01711. URL https://doi.org/10.1021/acs.jpclett.7b01711.

[98] A. Virga, C. Ferrante, G. Batignani, D. De Fazio, A. D. G. Nunn, A. C. Ferrari, G. Cerullo, and T. Scopigno. Coherent anti-stokes raman spectroscopy of single and multi-layer graphene. *Nature Communications*, 10(1):3658, Aug 2019. ISSN 2041-1723. doi: 10.1038/s41467-019-11165-1. URL https://doi.org/10.1038/s41467-019-11165-1.

[99] Jiwei Ling, Xianchong Miao, Yangye Sun, Yiqing Feng, Liwu Zhang, Zhengzong Sun, and Minbiao Ji. Vibrational imaging and quantification of two-dimensional hexagonal boron nitride with stimulated raman scattering. *ACS Nano*, 13(12): 14033–14040, Dec 2019. ISSN 1936-0851. doi: 10.1021/acsnano.9b06337. URL https://doi.org/10.1021/acsnano.9b06337.

[100] Franz Hempel, Sven Reitzig, Michael Rüsing, and Lukas M. Eng. Broadband coherent anti-stokes raman scattering for crystalline materials. *Phys. Rev. B*, 104:224308, Dec 2021. doi: 10.1103/PhysRevB.104.224308. URL https://link.aps.org/doi/10.1103/PhysRevB.104.224308.

[101] Amirmahdi Honardoost, Kamal Abdelsalam, and Sasan Fathpour. Rejuvenating a versatile photonic material: Thin-film lithium niobate. *Laser & Photonics Reviews*, 14(9):2000088, 2020. doi: https://doi.org/10.1002/lpor.202000088. URL https://onlinelibrary.wiley.com/doi/abs/10.1002/lpor.202000088.

[102] Lin Chang, Yifei Li, Nicolas Volet, Leiran Wang, Jon Peters, and John E. Bowers. Thin film wavelength converters for photonic integrated circuits. *Optica*, 3(5):531–

535, May 2016. doi: 10.1364/OPTICA.3.000531. URL http://opg.optica.org/optica/abstract.cfm?URI=optica-3-5-531.

[103] Jie Zhao, Chaoxuan Ma, Michael Rüsing, and Shayan Mookherjea. High quality entangled photon pair generation in periodically poled thin-film lithium niobate waveguides. *Phys. Rev. Lett.*, 124:163603, Apr 2020. doi: 10.1103/PhysRevLett.124.163603. URL https://link.aps.org/doi/10.1103/PhysRevLett.124.163603.

[104] Ashutosh Rao, Kamal Abdelsalam, Tracy Sjaardema, Amirmahdi Honardoost, Guillermo F. Camacho-Gonzalez, and Sasan Fathpour. Actively-monitored periodic-poling in thin-film lithium niobate photonic waveguides with ultrahigh nonlinear conversion efficiency of 4600 %w−1cm−2. *Opt. Express*, 27(18):25920–25930, Sep 2019. doi: 10.1364/OE.27.025920. URL http://opg.optica.org/oe/abstract.cfm?URI=oe-27-18-25920.

[105] Juanjuan Lu, Joshua B. Surya, Xianwen Liu, Alexander W. Bruch, Zheng Gong, Yuntao Xu, and Hong X. Tang. Periodically poled thin-film lithium niobate microring resonators with a second-harmonic generation efficiency of 250,000%/w. *Optica*, 6(12):1455–1460, Dec 2019. doi: 10.1364/OPTICA.6.001455. URL http://opg.optica.org/optica/abstract.cfm?URI=optica-6-12-1455.

A | Appendix A

A.1. Second order non-linear processes

Let us consider the second order non-linear optical processes, where the second order polarization $\boldsymbol{P}^{(2)}$ plays a significant role. In the general case, the components of $\boldsymbol{P}^{(2)}$ are defined as:

$$P_i^{(2)}(t) = \epsilon_o \int_{-\infty}^{+\infty} dt' \int_{-\infty}^{+\infty} dt'' \chi_{ijk}^{(2)}(t', t'') E_j(t, t') E_k(t, t', t'') \tag{A.1}$$

Where we neglected the spatial dependence and $\chi_{ijk}^{(2)}(t', t'')$ is the second order non-linear susceptibility. We made implicit use of the Einstein notation, summing over j and k, which both represent $\{x, y, z\}$. Let us introduce the same approximations exploited in (2.21), namely isotropic, time-invariant, homogeneous media and let us consider linearly polarized waves. Thus, we can simplify (A.1), in particular discarding the tensorial nature of $\chi^{(2)}$, obtaining:

$$P^{(2)}(t) = \epsilon_o \int_{-\infty}^{+\infty} dt' \int_{-\infty}^{+\infty} dt'' \chi^{(2)}(t', t'') E(t - t') E(t - t' - t'') \tag{A.2}$$

In the following, we will also assume that the second order susceptibility depends only on the instantaneous field, and not on the history of $E(t)$ in time. Therefore,

$$\chi^{(2)}(t', t'') = \chi^{(2)} \delta(t') \delta(t''), \tag{A.3}$$

Considering (A.3) and exploiting the property of the Dirac delta (2.46), we can rewrite (A.2) as:

$$P^{(2)}(t) = \epsilon_0 \chi^{(2)} E^2(t), \tag{A.4}$$

Let us consider an incoming electric field, made of two components, centered at different

frequencies ω_1 and ω_2:

$$E(t) = E_1 \cos(\omega_1 t + \phi_1) + E_2 \cos(\omega_2 t + \phi_2), \tag{A.5}$$

Where $\phi_{1,2}$ are the phases. We can now make use of the exponential representation of the cosine function and write (A.5) as:

$$E(t) = \frac{1}{2}\left(E_1 e^{i(\omega_1 t+\phi_1)} + E_1 e^{-i(\omega_1 t+\phi_1)} + E_2 e^{i(\omega_2 t+\phi_2)} + E_2 e^{-i(\omega_1 t+\phi_1)}\right), \tag{A.6}$$

Where we can define the complex amplitudes as:

$$\tilde{E}_1 = E_1 e^{i\phi_1}, \quad \tilde{E}_2 = E_2 e^{i\phi_2}, \tag{A.7}$$

Then, taking into account (A.7), we can write (A.6) as:

$$E(t) = \frac{1}{2}\left(\tilde{E}_1 e^{i\omega_1 t} + \tilde{E}_1 e^{-i\omega_1 t} + \tilde{E}_2 e^{i\omega_2 t} + \tilde{E}_2 e^{-i\omega_1 t}\right), \tag{A.8}$$

Substituting (A.8) in (A.4) we obtain:

$$\begin{aligned} P^{(2)}(t) = \frac{\epsilon_0 \chi^{(2)}}{4}\Big\{ & \tilde{E}_1^2 e^{2i\omega_1 t} + \tilde{E}_1^{*2} e^{-2i\omega_1 t} + \tilde{E}_2^2 e^{2i\omega_2 t} + \tilde{E}_2^{*2} e^{-2i\omega_2 t} + \\ & + 2\tilde{E}_1\tilde{E}_1^* + 2\tilde{E}_2\tilde{E}_2^* + 2\tilde{E}_1\tilde{E}_2^* e^{i(\omega_1-\omega_2)t} + 2\tilde{E}_1^*\tilde{E}_2 e^{-i(\omega_1-\omega_2)t} + \\ & + 2\tilde{E}_1\tilde{E}_2 e^{i(\omega_1+\omega_2)t} + 2\tilde{E}_1^*\tilde{E}_2^* e^{-i(\omega_1+\omega_2)t}, \Big\} \end{aligned} \tag{A.9}$$

Equation (A.9) can be simplified and written as:

$$\begin{aligned} P^{(2)}(t) = \frac{\epsilon_0 \chi^{(2)}}{2}\big\{ & E_1^2 cos(2\omega_1 t + 2\phi_1) + E_2^2 cos(2\omega_2 t + 2\phi_2) + \\ & + 2E_1 2E_2 cos[(\omega_1 - \omega_2)t + \phi_1 - \phi_2] + \\ & + 2E_1 2E_2 cos[(\omega_1 + \omega_2)t + \phi_1 + \phi_2] + \\ & + 2E_1^2 + 2E_2^2\big\}, \end{aligned} \tag{A.10}$$

In figure A.1, a scheme of the light-matter interaction with a material with $\chi^{(2)} \neq 0$ is reported.

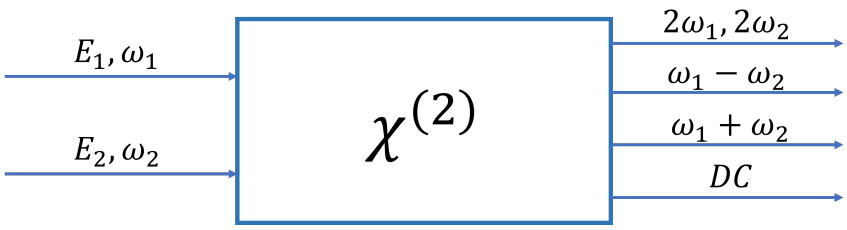

Figure A.1: Conceptual scheme of the interaction between light and matter considering second order non-linear processes.

The non-linear polarization acts as a source giving rise to terms that oscillate at frequencies different from the incoming ones. It is possible to identify four different phenomena:

1. Second Harmonic Generation (SHG),
2. Difference Frequency Generation (DFG),
3. Sum Frequency Generation (SFG),
4. Optical rectification (OR).

In fig. A.2, the Jablonsky diagrams of the aformentioned phenomena are shown.

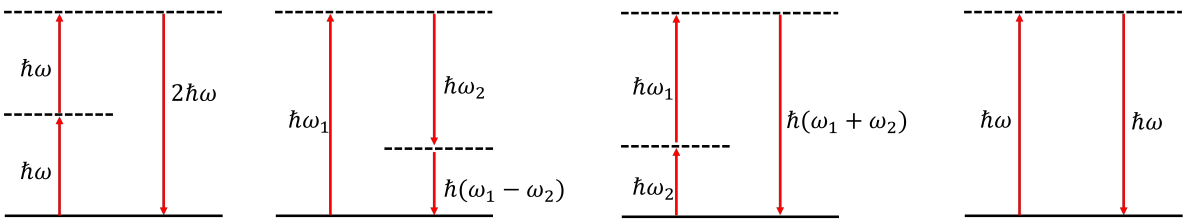

(a) Second harmonic generation. (b) Difference frequency generation. (c) Sum frequency generation. (d) Optical rectification.

Figure A.2: Jablonsky diagram of second order non-linear processes, respectively: (a) second harmonic generation, (b) difference frequency generation, (c) sum frequency generation, (d) optical rectification.

B | Appendix B

B.1. Spontaneous Raman set-up

The spontaneous Raman spectra were acquired employing a home-built confocal Raman microspectroscopy unit in inverted configuration. The light source is a continuous-wave diode laser (Cobolt AB, Flamenco) centered at 660 nm. The pump beam is delivered to a commercial inverted microscope (IX73, Olympus Europa SE & Co. KG) with a single edge dichroic beam splitter (Di03-R660-t1-25x36, Semrock). The pump light is directed onto the materials via a dry/air 20x objective (MPLFLN20X 20x/0.45 NA, Olympus), which then collects the backscattered Raman photons and directs them back to the dichroic beam splitter. The residual pump light is removed through a long-pass (664 nm) edge filter (LP02-664RU-25, Semrock), which transmits only the Stokes Raman signal. Finally, the Raman scattered light is focused on the entrance slit of a spectrometer with a lens. For the spontaneous Raman measurements in the fingerprint region, we used a monochromator (Isoplane160, Princeton instruments) with a grating of 1200 gr/mm equipped with a front illuminated CCD (PIXIS256F, Princeton Instruments). We performed all the measurements with an excitation power equal to 50 mW. All the SR spectra shown in the previous sections were obtained with an integration time of 5 s, averaging over five measurements. We pre-processed the spectra in order to remove the baseline (due to fluorescence) employing a polynomial curve with degree 8. The wavenumber axis was calibrated using tabulated Raman peaks of ethanol and methanol.

List of Figures

Acronyms

Acronym	Meaning
ALS	Alternating least square
B-CARS	Broadband CARS
CARS	Coherent anti-Stokes Raman scattering
CCD	Charge-coupled device
CEP	Carrier-envelope phase offset
CRS	Coherent Raman scattering
CSRS	Coherent Stokes Raman scattering
DFG	Difference frequency generation
DMSO	Dimethylsulfoxid
E-CARS	Epi-detected CARS
FA	Fatty acid
F-CARS	Forward-detected CARS
FROG	Frequency resolved optical gating
FWHM	Full width at half maximum
FWM	Four wave mixing
GDD	Group delay dispersion
GVD	Group velocity dispersion
HWP	Half-wave plate
IR	Infrared
KK	Kramers-Kronig
LIA	Lock-in amplifier
LN	Lithium Niobate
LPF	Long pass filter
MCR	Multivariate curve resolution
MEM	Maximum entropy method

Acronym	Meaning
MIR	Mid-infrared
NIR	Near-infrared
NMF	Non-negative matrix factorization
NRB	Non-resonant background
OR	Optical rectification
PBS	Polarizing beam splitter
PCF	Photonic-crystal fiber
PMMA	Polymethylmethacrylate)
PS	Polystyrene
PWA	Plane wave approximation
SC	Supercontinuum
SFG	Sum frequency generation
SHG	Second harmonic generation
SNR	Signal-to-noise ratio
SPF	Short pass filter
SPM	Self phase modulation
SR	Spontaneous Raman
SRG	Stimulated Raman gain
SRL	Stimulated Raman loss
SRS	Stimulated Raman scattering
SVD	Singular value decomposition
SVEA	Slowly varying envelope function approximation
TAMP	Tuned amplifiers
T-CARS	Time-delayed CARS
THG	Third harmonic generation
TOD	Third order dispersion
YAG	Yttrium aluminium garnet